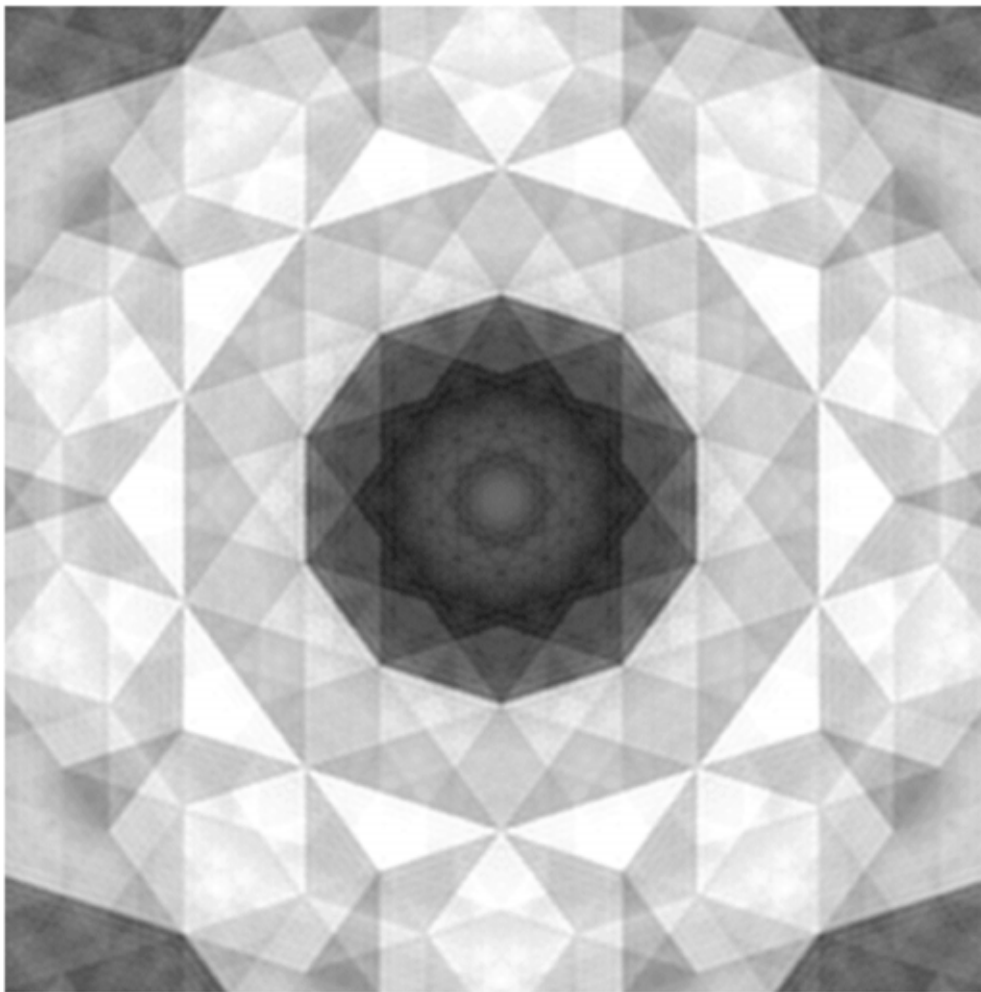


Diss. ETH Nr. 15819

# **Modelling Disorder in Quasicrystals.**

Decagonal Al-Co-Ni.



presented by

**Miroslav Kobas**

**Cover image:** Calculated truncation error of an atomic surface of a rhombic Penrose tiling in the  $4D$  hypercubic description. The truncation error is located at the origin of the body diagonal of the  $4D$  hyper-rhombohedral unit cell.

# **Modelling Disorder in Quasicrystals.**

Decagonal Al-Co-Ni.

Dissertation

submitted to the

**ETH**

Swiss Federal Institute of Technology Zurich

for the degree of

**Doctor of Natural Sciences**

presented by

**Miroslav Kobas**

Dipl. Werkstoff-Ing. ETH  
born 23 September 1975  
citizen of Kirchberg SG

Accepted on the recommendation of

Prof. Dr. Walter Steurer  
Dr. Thomas Weber  
Prof. Dr. Friedrich Frey

Examiner  
Co-examiner  
Co-examiner





# TABLE OF CONTENTS

<b>Summary .....</b>	<b>1</b>
<b>Zusammenfassung .....</b>	<b>3</b>
<b>1 Introduction.....</b>	<b>5</b>
<b>2 Diffuse scattering from disordered materials .....</b>	<b>8</b>
2.1 Experimental techniques	8
2.2 Diffuse scattering from 3D periodic crystals	10
2.3 Diffuse scattering from quasicrystals	11
2.4 Modelling techniques	12
<b>3 Patterson analysis of diffuse X-ray scattering data .....</b>	<b>14</b>
3.1 Article I	14
3.2 Appendix	46
<b>4 Modelling structural disorder of the Bragg layers .....</b>	<b>50</b>
4.1 Article II	50
4.2 Article III	55
4.3 Appendix	93
<b>5 Modelling structural disorder of the diffuse interlayers .....</b>	<b>96</b>
5.1 Article IV	96
<b>6 Outlook .....</b>	<b>101</b>
6.1 Optimisation of the <i>punch-and-fill</i> method	101
6.2 Growth model for decagonal Al-Co-Ni	102
<b>Bibliography .....</b>	<b>107</b>
<b>Curriculum vitae.....</b>	<b>108</b>
<b>Acknowledgements .....</b>	<b>109</b>

## Summary

The theme of this doctoral thesis is the modelling of structural disorder phenomena from decagonal Al-Co-Ni quasicrystals by an analysis of full diffuse X-ray scattering data as a function of temperature. The motivation for this study is to reveal the complex ordering principles of decagonal Al-Co-Ni quasicrystals and, consequently, to understand the driving force for the formation and stability of these materials.

For the first time, the 3D difference Patterson (autocorrelation) function of a disordered quasicrystal (*Edagawa-phase*) has been analysed. A new technique, the *punch-and-fill* method has been developed to separate diffuse scattering and Bragg reflections. Its potential and limits are discussed in detail. The calculated difference Patterson maps are interpreted in terms of inter-cluster correlations as a function of temperature. Both, at high and low temperatures, clusters decorate the vertices of the same quasiperiodic covering. At high temperatures, medium-range inter-cluster correlations are present, whereas at low temperatures, the ordering between the clusters becomes less concise. Qualitatively, the Patterson maps may be interpreted by inter-cluster correlations, which take place mainly inside pentagonal superclusters below 1120 K, and inside larger decagonal superclusters at 1120 K. The pentagonal supercluster consists of five *Gummelt* clusters at the corners of a star-centered pentagon with  $\approx 20$  Å edge length; the decagonal supercluster is composed of one central *Gummelt* cluster edge-joiningly surrounded by a ring of ten further overlapping *Gummelt* clusters.

The hydrodynamic theory of phasonic and phononic disorder has been applied successfully to describe the short-range, disordered structure of the *Edagawa-phase*. Moreover, model calculations demonstrate that the main features of diffuse scattering can equally well be described by phasonic disorder and fivefold orientational disorder of clusters. The calculations allow to distinguish the different cluster types published so far and the best agreement with experimental data could be achieved with the mirror-symmetric Abe-cluster. Modelling of phasonic diffuse scattering associated with the S1 and S2 superstructure reflections indicates disorder of superclusters. The former show basically inter-cluster correlations inside quasiperiodic layers, while the latter exhibit intra- and inter-cluster correlations, both between adjacent and inside quasiperiodic layers. The feasibility, potential and limits of the Patterson method in combination with the *punch-and-fill* method employed is shown on the example of a phasonic disordered rhombic Penrose tiling. A variation of the

elastic constants within the framework of the hydrodynamic theory does not change qualitatively the way phasonic disorder is realized in the *local* quasicrystalline structure. For the same model system it is also shown that phasonic fluctuations of the atomic surfaces give average clusters in the cut-space, which correspond to fivefold orientationally disordered clusters, *i.e.* phasons induce fivefold orientational disorder of clusters.

A Patterson analysis of the diffuse interlayers from the *Edagawa-phase* showed that the main unit for correlated displacements along the periodic direction is a disordered structure motif (cluster) with a diameter of  $\approx 15$  Å, the fine structure of which does hardly change as a function of temperature. At 1120 K, the displacements of the clusters are uncorrelated along quasiperiodic directions, while at lower temperatures  $\approx 42$  Å-sized superclusters of a well-defined shape are formed. The spatial distribution but not the internal structure of the superclusters differs significantly at 1070 K and 300 K.

## Zusammenfassung

In der vorliegenden Arbeit werden Modellrechnungen von strukturellen Fehlordnungsphänomenen an dekadagonalen Quasikristallen präsentiert. Als Ausgangsbasis diente die Analyse von diffusen Streuphänomenen als Funktion der Temperatur. Die Motivation für diese komplexen Untersuchungen liegt darin, Verständnis für die Grundprinzipien, die für die Bildung und Stabilität dieser Materialien verantwortlich sind, zu erlangen.

Zum ersten Mal wurde die 3D Pattersonfunktion (Autokorrelationsfunktion) der Differenzstruktur eines fehlgeordneten Quasikristalls (*Edagawa-phase*) untersucht. Zu diesem Zweck wurde eine neue Methode, die *punch-and-fill* Methode, entwickelt, die es erlaubt diffuse Streuung aus 3D Streudaten zu separieren. Möglichkeiten und Grenzen der Methode werden aufgezeigt und eingehend diskutiert. Die berechneten Pattersonkarten der Differenzstruktur werden durch Interclusterkorrelationen interpretiert, die sich als Funktion der Temperatur ändern. Es zeigt sich, dass Cluster die Eckpunkte der ein und derselben quasiperiodischen Überdeckung dekorieren und zwar über den ganzen untersuchten Temperaturbereich. Bei hohen Temperaturen bilden sich ausgeprägte mittelreichweitige Interclusterkorrelationen aus; bei tieferen Temperaturen dagegen nimmt die Ordnung zwischen den Clustern deutlich ab. Qualitativ können die Pattersonkarten in der Art und Weise interpretiert werden, dass sich Interclusterkorrelationen bei Temperaturen unter 1120 K, vorwiegend innerhalb pentagonaler Supercluster ausbilden, bei Temperaturen über 1120 K dagegen vorwiegend innerhalb der grösseren dekadagonalen Supercluster. Der pentagonale Supercluster besteht aus jeweils fünf *Gummelt*-Clustern an den Ecken eines sternförmigen Pentagons mit  $\approx 20$  Å Kantenlänge. Der dekadagonale Supercluster lässt sich durch einen zentralen *Gummelt*-Cluster beschreiben, der von einem Ring bestehend aus zehn sich überlappenden *Gummelt*-Clustern umgeben ist.

Die hydrodynamische Theorie von phasonischer und phononischer Fehlordnung ist erfolgreich angewendet worden um die kurzreichweitige, fehlgeordnete Struktur der *Edagawa-Phase* zu beschreiben. Die Rechnungen zeigen, dass die Hauptmerkmale der diffusen Streuung gleichermassen durch phasonische Fehlordnung wie auch durch eine fünffache Cluster-Orientierungsfehlordnung beschrieben werden können. Die Empfindlichkeit der berechneten diffusen Streuintensitäten auf die verwendeten Clustertypen erlaubt zudem die zahlreichen, in der Literatur vorgeschlagenen Clustertypen voneinander zu unterscheiden. Die beste Übereinstimmung mit experimentellen Daten konnte mit dem spiegelsymmetrischen Abe-Cluster erzielt werden. Modellrechnungen phasonischer Fehlordnung

anhand der S1 und S2 Überstrukturreflexe deuten auf unterschiedlich korrelierte Fehlordnungphänomene der Superclustern hin. Die phasonisch diffuse Streuung assoziiert mit den S1 Satelliten zeigt vorwiegend Interclusterkorrelationen auf, die sich innerhalb quasiperiodischer Ebenen erstrecken; die phasonisch diffuse Streuung der S2 Satelliten dagegen sowohl Intra- wie auch Interclusterkorrelationen, die sich sowohl zwischen benachbarten, als auch innerhalb der quasiperiodischen Ebenen formieren. Machbarkeit, Potenzial und Grenzen der Pattersonanalyse in Kombination mit der eingesetzten *punch-and-fill* Methode ist anhand eines Beispiels, einer phasonisch fehlgeordneten, rhombischen Penrose-Parkettierung, aufgezeigt. Es zeigte sich auch, dass eine Variation der elastischen Konstanten im Rahmen der hydrodynamischen Theorie die Art und Weise wie sich phasonische Fehlordnung in der lokalen quasiperiodischen Struktur manifestiert, nur unmassgeblich beeinflusst. Anhand desselben Modellsystems konnte desweiteren aufgezeigt werden, dass phasonische Fluktuationen der atomaren Hyperflächen gemittelte Cluster im Schnittraum ergeben, die fünffach orientierungsfehlgeordneten Clustern entsprechen. Dies deutet auf eine Induzierung von fünffacher Cluster-Orientierungsfehlordnung durch Phasonen hin.

Die Pattersonanalyse der diffusen Zwischenschichten der *Edagawa-phase* zeigte, dass die fundamentalen Baueinheiten für korrelierte Verschiebungen entlang der periodischen Achse einem fehlgeordneten Strukturmotiv (Cluster) zuzuordnen sind, das einen Durchmesser von  $\approx 15$  Å aufzeigt. Die Feinstruktur dieses Clusters bleibt über den ganzen untersuchten Temperaturbereich hin unverändert. Bei 1120 K sind Verschiebungen der Cluster entlang quasiperiodischer Richtungen unkorreliert, wogegen sich bei niederen Temperaturen  $\approx 42$  Å grosse Supercluster ausbilden, die eine wohl definierte Form besitzen. Die räumliche Verteilung dieser Supercluster unterscheidet sich klar zwischen 1070 K und 300 K, ihre Feinstruktur dagegen bleibt weitgehend unverändert.

# 1 Introduction

One of the main discoveries in solid-state physics in the eighties has been the discovery of quasicrystals in 1982 by Shechtman [Shechtman, 1984]. Since then, the field of quasicrystal research has experienced an enormous growth. The number of publications on quasicrystals has exceeded 8000. From the beginning on, the field has been multidisciplinary; mathematicians, experimental and theoretical physicists, crystallographers, material scientists and chemists have worked together to get a better understanding of this form of matter.

Inspired by the growing numbers and varieties of quasicrystals, the International Union of Crystallography has redefined the term crystal to mean 'any solid having an essentially discrete diffraction pattern'. Thereby the essential attribute of crystallinity has been shifted from direct space to reciprocal space. The quasicrystalline state is most probably a third form of solid matter beside the 3D periodic crystalline and the amorphous state. Quasicrystals possess long-range aperiodic order and crystallographically forbidden rotational symmetries, e.g. five-, eight-, ten- or twelvefold. These symmetries forbid a 3D periodic structure and do instead enforce quasiperiodicity. Quasicrystals can be classified in three groups, one-dimensional (Fibonacci phases; quasiperiodic stacking of periodic layers), two-dimensional (pentagonal, decagonal, octagonal and dodecagonal phases; periodic stacking of quasiperiodic layers) and three-dimensional quasicrystals (icosahedral phases). Nowadays, both metastable and thermodynamically stable phases are known and several quasicrystals can be synthesized with a degree of perfection comparable to that of silicon.

Before the actual synthesis of quasicrystals took place, several theoretical works already existed. In 1974 Penrose described a tiling consisting of two different unit tiles [Penrose, 1974]. These tiles cover a plane without gaps and without repeating patterns, simply by imposing a set of matching rules for how the tile edges are allowed to be joined. The resulting tiling has local fivefold symmetry and can be used to describe the structure of quasicrystals. Several other concepts such as cluster-coverings and irrational cuts through higher-dimensional space have been developed for the same task. Nevertheless, not a single quasicrystal structure is known with the same reliability that is normal in standard structure analysis.

What makes quasicrystal structure analysis so demanding is that it requires the determination of both, short-range and long-range order. The former mainly refers to the atomic arrangement inside a cluster, while the latter refers to the ordering of the clusters themselves. An aggravating circumstance is the inherent disorder that is present in most quasicrystals. Disorder in quasicrystals has an exceptional position because the thermodynamical stability region of quasicrystals is at high temperatures (typically over 1000 K). This ensures a role to entropy as a stabilizing factor. The additional degrees of freedom from the higher-dimensional description of quasicrystals lead to disorder phenomena specific to quasicrystals, e.g. phasonic disorder.

Despite twenty years of intensive research on quasicrystals, fundamental questions are still open: What is the driving force for the formation and stability of quasicrystals? Does strict quasiperiodic order really exist in quasicrystals? Why have only quasicrystals been observed with five-, eight-, ten- and twelvefold rotational symmetries? These considerations point out that the exact knowledge of the evolution of structural order and disorder in quasicrystals as a function of temperature will be a key to the understanding of real quasicrystals.

The focus of this work concentrates on the modelling of structural disorder in decagonal Al-Co-Ni (*Edagawa-phase*, [Edagawa, 1994]). The system Al-Co-Ni has been in the focus of decagonal quasicrystal research in the last ten years. It is an excellent model system: the phase diagram is well known, large single crystals can be easily grown and several structural modifications of the decagonal phases have been found as a function of temperature and composition. Diffraction data from most Al-Co-Ni quasicrystals show diffuse scattering in addition to Bragg reflections. The *Edagawa-phase* shows an extraordinary richness of complex scattering including one-, two- and three-dimensional diffuse scattering. The reciprocal space sections perpendicular to the periodic axis are all sharp along the tenfold axis. Even numbered layers contain Bragg reflections as well as diffuse scattering and are named 'Bragg layers'. They reflect the  $\approx 4$  Å periodic average structure. The odd numbered layers, which show diffuse scattering only, are referred to as 'diffuse interlayers' and they represent the  $\approx 8$  Å superstructure.

Most structural investigations of disordered materials are done by the use of diffractometric methods. Diffuse scattering from X-ray diffraction measurements of single crystals are most commonly used for the investigation of structural disorder phenomena. By an analysis thereof, one obtains typically structural information on a length scale of a few hundred Å. Usually, these investigations do not include the analysis of diffuse scattering, which originates from structural *defects* such as point defects, dislocations, grain and phase

boundaries, precipitates, *etc.* The diffuse scattering thereof can hardly be measured. The reason for this is on the one hand due to the low concentrations of these defects compared to the concentration of atoms, which leads to very weak diffuse scattering intensities. On the other hand, the microscopic dimensions of these defects often lead to high-frequent scattering, which can only be resolved in high-resolution diffraction measurements. Thus, the observed diffuse scattering intensities mainly originate from structural disorder phenomena and not from structural defects.

The thesis is organized as follows: §2 gives an introduction into diffuse scattering from disordered materials. §3 shows a reprint of the article, in which the *punch-and-fill* method is described and which includes the interpretation of the difference Patterson maps in terms of inter-cluster correlations. §4 includes two articles, which deal with the modelling of structural disorder phenomena of decagonal Al-Co-Ni quasicrystals. These calculations deal with the diffuse scattering inside the Bragg layers. §5 includes a reprint of the article, which deals with the study of the diffuse interlayers. §6 gives an outlook onto some possibilities to optimise the *punch-and-fill* method. Moreover, a growth model for decagonal Al-Co-Ni is discussed, which may allow the modelling of the 3D disordered structure of the *Edagawa-phase*.



## **2 Analysis of disordered materials**

Structural research has traditionally played an important role in solid state physics since the determination of the arrangements of atoms in space is the prerequisite to subsequently determine the different physical properties. Investigation of structurally disordered materials is complicated and often leads to relatively imprecise results. Nevertheless, both the fundamental aspect and the ever wider industrial applications give structurally disordered materials a role that cannot be overlooked. Several books have been published focusing on studies of disordered materials [Cowley, 1995; Nield, Keen, 2001; Ossi, 2002; Welberry, 2004].

### **2.1 Experimental techniques**

The main experimental techniques used in structural investigations of disordered materials are diffraction experiments (X-ray, neutron, electron), absorption spectroscopies (extended X-ray absorption fine structure, EXAFS; X-ray absorption near edge structure, XANES), Mössbauer spectroscopy and vibrational spectroscopies (infrared, IR; Raman). Diffractometric methods are the most common technique and most diffuse scattering studies have involved single crystal measurements using X-ray diffraction.

The basic principles of X-ray, neutron and electron diffraction are the same. X-ray diffraction is commonly used in structural analysis and can be used to study all types of disorder except for magnetic disorder. Data correction to study diffuse scattering from X-ray diffraction is a general problem since diffuse scattering phenomena are mostly weak and often have a broad distribution in reciprocal space. The intensity of synchrotron sources allows the use of relatively small samples (several microns) and facilitates fast measurements of diffuse scattering. Anomalous dispersion can be used to contrast between atomic species near to each other in the periodic table. Modern X-ray instrumentation also offers extremely high signal to noise ratio and high resolution, which is important when diffuse features around or even peaking under Bragg reflections are investigated.

The lower intensity of neutron sources means that samples need to be larger ( $\approx$  cubic centimeter). The limited availability of experimental sources compared to the other methods is an additional disadvantage. However, for neutron diffraction it is easier to obtain data on an

absolute scale and data correction is generally well understood. One advantage of neutron diffraction is that the scattering length of the atoms does not show a systematic dependence on their atomic number and that it does not decrease with increasing diffraction vector (in the same way as the X-ray form-factor). This allows to study atomic species, which are near to each other in the periodic table and also to study atomic species with low atomic weights. Neutrons have similar energies to the energies of lattice vibrations. This can be used to probe the energy change in the sample as a result of neutron-lattice interactions. This allows measurements of dynamic disorder, such as phononic disorder, and one can separate between scattering of static and dynamic origin. The last advantage of neutron scattering is the possibility to measure diffuse scattering, which arises from disordered magnetic structures. In many cases X-rays and neutrons can be used interchangeably. Diffractometric methods often provide enough information for the determination of short-range and, together with the development of structural models, medium-range order.

The main advantage of electron diffraction is that it can be used to study very small single crystals. Since the averaging is done over a smaller volume than for neutrons and X-rays, it can sometimes provide more insight into the underlying structure, e.g. in a heterogenous structure. Multiple scattering significantly takes place in electron diffraction, which differs from X-ray and neutron diffraction. Consequently, the diffuse scattering in electron diffraction patterns may have a different appearance compared to the X-ray or neutron patterns. Multiple scattering effects can result in a transfer of diffraction intensity from one region of the pattern to another often simplifying the appearance of diffuse scattering.

EXAFS is a technique to specifically examine the chemical short-range structure and provides detailed information on the average local environment around a given atom. Both, conventional diffraction and EXAFS, give us information on the atomic pair-correlations, whereas XANES gives us information on multi-site interactions. Mössbauer spectroscopy provides spatially averaged information on the nearest neighbour configurations of an atom. It is a nuclear spectroscopy based on the emission of  $\gamma$ -rays associated with any transition between nuclear energy levels. Vibrational spectroscopies are used to obtain information on the molecular structure of organic and inorganic compounds (stretching, bending and torsion of a molecule). In general, the IR and Raman spectra of a system are complementary to each other. Both Mössbauer and vibrational spectroscopies supply us with indirect structural information.

## 2.2 Diffuse scattering from 3D periodic crystals

The diffuse contribution to scattering data from crystalline materials, whether using X-ray, neutron or electron diffraction, arises from the deviation of the system under study from perfect order. Thus, disorder can be defined as the deviation from perfect order. Scattering experiments from all real crystals will display diffuse features in addition to Bragg reflections, since equilibrium defects (e.g. thermal vacancies) and dynamical deviations (e.g. thermal vibrations) are always present, even at thermodynamical equilibrium. Bragg scattering contains information on the averaged structure only. Any structural disorder is implied in the averaged structure via partially occupied sites and the atomic displacement parameters. In fact, Bragg scattering only contains single-site information, while diffuse scattering contains information on *real* pair-correlations. Detailed information on static, dynamic and orientational disorder can only be obtained by an analysis of diffuse scattering. Static disorder covers for example displacive disorder, substitutional disorder, stacking faults and other planar faults; dynamic disorder is disorder that changes with time or temperature, such as phononic disorder; orientational disorder is present when molecules on equivalent sites in different unit cells have different orientations (can be both static and dynamic). This variability makes the analysis of diffuse scattering far from straightforward, and many different methods have been developed to analyse specific disorder phenomena.

Diffuse scattering can be elastic, quasi-elastic and inelastic in nature. In the case of elastic scattering, the incident beam does not change its energy during the scattering process. This is the case for diffuse scattering from static disorder phenomena. Quasi-elastic and inelastic scattering results when the energy of the beam changes during the scattering process. This type of diffuse scattering is due to dynamic disorder. Diffuse scattering measurements in which no energy discrimination is used, effectively integrate over all intensities, *i.e.* the distinction between elastic and inelastic scattering is lost. The observed intensity is then a time average of the instantaneous intensities. This time averaging can be considered equivalent to an averaging over space [see Cowley, 1995]. Usually the region of a homogeneous sample, which reflects coherently is limited in size to be very much smaller than the total illuminated size. The reason for this behaviour is on the one hand due to the size of the mosaic grains of the crystal and on the other hand due to the limitations on the coherence of the incident beam. The lateral coherence of the beam is in the order of several hundred Å and is limited by the divergence of the beam. The coherence of the beam in the direction of propagation is limited by the monochromaticity and is typically in the order of about 1 micron for X-rays. Thus, the total diffracted intensity corresponds to the incoherent

summation of the scattering intensities from a large number of independent but statistically equivalent regions. This is the same as the incoherent summation of the scattering intensities from any one region at different times. In time, any one region may take all the possible configurations of the atoms present and for a large number of independent regions, all possible configurations are represented at any time.

Provided that the kinematical theory of diffraction applies, the diffraction pattern of any object is the Fourier transform of the pair-correlation function. Information on multi-site interactions between atoms or arrangements of atoms do not directly contribute to the diffraction patterns [see Welberry, 1986]. However, their effects are felt indirectly, for example in the constraints that are imposed on the two-site interactions and the way in which these decay with distance. Two-site and multi-site interactions are not independent from each other since the need to densely fill the space with atoms restricts the possible atomic arrangements. Multi-site occupational correlations can result in distinctive diffraction effects when additional relaxation displacements are considered. However, if a system has properties that stem from multi-site interactions there is no simple way in which these can be related to the observed intensities. The diffuse scattering from such a system arises from pair-correlations, which are indirectly generated from the fundamental multi-site interactions.

### **2.3 Diffuse scattering from quasicrystals**

Everything said in the previous section on diffuse scattering from 3D periodic crystals is also true for quasicrystals. The physical properties of a crystal are determined by two factors: the chemical constituents and the crystal structure. In quasicrystals, the structure appears to be dominant, and the study of structure-property relations is not only of academic interest, but of importance in applications. The analysis of real structures encloses the study of order, disorder and defects. Several books have been published that focus on studies of quasicrystals and include chapters on disorder or defects [Janot, 1994; Nield, Keen, 2001; Ossi, 2002; Stadnik, 1998; Suck, Schreiber, Häussler, 2002; Trebin, 2003].

Decagonal quasicrystals can basically be described in two reasonable ways. In the first approach, they are described in terms of a higher-dimensional space, in which the quasicrystalline structure is periodic [see Stadnik, 1998]. This periodic space is composed of two orthogonal subspaces: the parallel-space and the perpendicular-space. Atomic surfaces, extended along the perpendicular-space, decorate the higher-dimensional lattice. For perfect

quasicrystals, all the measured scattering may be expressed as a sum of  $\delta$ -functions, which cover the complete space. Any diffuse scattering is intermixed with these peaks since the experimental resolution allows to detect only the most intense peaks. In this description, diffuse scattering can occur due to fluctuations in the sizes and shapes of the atomic surfaces. A new type of displacive disorder occurs in quasicrystals if displacements along directions of the perpendicular-space are considered. This so called phasonic disorder leads to correlated flips of atoms or groups of atoms in the 3D structure. In the simplest case, such a phason mode corresponds simply to an atomic jump from one position to a nearby one with similar symmetry. The problem with this higher-dimensional approach is that it tends to ignore the fact that the quasicrystal itself is a three-dimensional object.

The second approach used to describe quasicrystals is with a tiling model, in which a quasiperiodic arrangement of atoms is made up by two or more tiles decorated with atomic clusters. Closely related periodic structures (approximants) exist with similar atomic clusters. A Perfect quasiperiodic tiling is determined by local matching rules, which are strictly fulfilled. If these matching rules are violated, disorder arises, either towards a more random or towards a more periodic tiling [see Trebin, 2003]. In the random tiling model, violation of the strict matching rules leads to diffuse scattering in the diffraction patterns. Both, the higher-dimensional description and the tiling model, lead to sharp Bragg reflections, unless there is phasonic disorder.

## 2.4 Modelling techniques

It is becoming increasingly common for scientists to adopt computer simulations methods to investigate crystalline systems. It is often not possible to apply established theoretical descriptions to disordered systems analytically, and it quickly becomes a complex task to rigorously describe the interactions between atoms as the material becomes increasingly disordered. Nevertheless, computer simulations can be used to bridge the gap between theory and experiment. They can be used to check the validity of analytical parameters in terms of atom positions and correlations. This is especially true in the case of structural disorder where a more complete picture may be obtained from a computer simulation than from an analytical treatment that relies on a number of possibly inappropriate approximations. Nowadays, model systems can be simulated that closely represent the physical system of interest.

The analysis of diffuse scattering using model calculations of disordered structures involves the comparison of calculated diffuse scattering from the model structure with the experimental diffuse scattering. This approach does not give a unique solution of the problem. However, with the incorporation of chemical knowledge into the construction of the disordered structure model both chemically and physically meaningful solutions can be found. In the following, some simulation techniques to study disordered materials are briefly characterized. The techniques used in the present study are described in article III.

Molecular dynamics (MD) simulations are particularly suited to the study of dynamic disorder and are not an entirely appropriate method to study static disorder. The MD method is versatile and the following thermodynamical properties may be calculated: diffusion coefficients, lattice vibrations, phonon density of states and energy maps. The structural configurations, which are obtained from the MD calculations, allow to extract structural parameters such as pair-correlation functions, structure factors and average density maps.

Monte Carlo (MC) simulations have been applied to many areas in science and shown to be extremely versatile. It is a powerful tool whenever the disordered system can be described by a set of interaction potentials. MC simulations start with the description of a set of potentials, which the system is then constrained to. From the potentials one obtains the structure and subsequently the structure factors. MC simulations were successfully applied by Welberry and co-workers to study diffuse scattering from single crystal X-ray data [e.g. Proffen and Welberry, 1998].

Reverse Monte Carlo (RMC) modelling uses the experimental intensities to deduce the structure, *i.e.* the MC simulation is operated in reverse. The strength and weakness of RMC lies in the fact that no interatomic potentials are imposed in the structural modelling. The definition of structural constraints is important, not to say essential in RMC modelling. Arbitrary, physically and chemically unreasonable, structural models may be obtained, which perfectly reproduce the experimental diffraction pattern. The earliest RMC modelling of crystalline systems used powdered samples [Keen, 1990] and after that, diffuse scattering from single crystal X-ray and neutron data was analysed [e.g. Proffen and Welberry, 1997a, 1997b].

### **3 Patterson analysis of diffuse X-ray scattering data**

#### **3.1 Article I**

This section contains a reprint of the article:

M. Kobas, Th. Weber and W. Steurer: Structural disorder in decagonal Al-Co-Ni.

Part A. Patterson analysis of diffuse X-ray scattering data. *Phys. Rev. B*, submitted.

Additional figures concerning this article are depicted in the appendix.

# Structural disorder in decagonal Al-Co-Ni.

## Part A: Patterson analysis of diffuse X-ray scattering data.

Miroslav Kobas<sup>1</sup>, Thomas Weber<sup>1</sup>, and Walter Steurer<sup>1,2</sup>

<sup>1</sup>*Laboratory of Crystallography, Department of Materials, ETH Zurich, CH-8093 Zurich, Switzerland*

<sup>2</sup>*MNF, University of Zurich, Switzerland*

For the first time, the three-dimensional (3D) difference Patterson (autocorrelation) function of a disordered quasicrystal (*Edagawa-phase*) has been analysed. 3D diffuse X-ray diffraction data were collected *in-situ* at 300 K, 1070 K and 1120 K. A new method, the *punch-and-fill* technique, has been developed for separating diffuse scattering and Bragg reflections. Its potential and limits are discussed in detail. The difference Patterson maps are interpreted in terms of inter-cluster correlations as a function of temperature. Both at high and low temperatures, the clusters decorate the vertices of the same quasiperiodic covering. At high temperatures, medium-range inter-cluster correlations are present, whereas at low temperatures, the ordering between the clusters becomes less pronounced. Qualitatively, the Patterson maps may be interpreted by inter-cluster correlations that take place mainly inside pentagonal superclusters below 1120 K, and inside the larger decagonal superclusters at 1120 K. The results of our diffraction study are published in two parts. Part *A* focuses on the 3D Patterson analysis based on experimental data, part *B* reports modelling of structural disorder in decagonal Al-Co-Ni.

61.44.Br, 61.43.Bn, 61.10.Nz

## I. INTRODUCTION

Real crystals can be perfect but never ideal. An ideal crystal is a fictitious infinite mathematical object. A crystal is perfect if it is in its thermodynamic equilibrium state. At any given finite temperature equilibrium defects (*e.g.* thermal vacancies) and dynamical



deviations (*e.g.* thermal vibrations) from the ideal structure are present. In quite a few cases, the entropic contribution by structural disorder decreases the free energy of a crystal by an amount to stabilize this structure against another one with lower enthalpy. Disorder is favorable if the energy landscape allows alternative structural arrangements at low energy costs. The study of equilibrium disorder, therefore, can give valuable insight into the structural factors governing the stability of a crystal.

Everything said is also true for quasicrystals. Quasicrystals, at least the known ones, are binary or ternary intermetallic phases, many of them stable. There is some experimental evidence that they are electronically stabilized in the same way as Hume-Rothery phases are. Indeed, most quasicrystals have been discovered based on this hypothesis by searching phase diagrams for compounds with particular valence electron concentration.<sup>1</sup> However, there are still open questions concerning stability and structure. There are two fundamentally different approaches. The one says that quasicrystals are built up of energetically very favorable clusters (*quasi-unit-cell* approach). The lowest total energy can be achieved by maximization of the cluster density. Jeong and Steinhardt<sup>2</sup> showed that for clusters with fivefold symmetry the Penrose tiling (*Gummelt* decagon-covering) fulfills this condition. Consequently, strictly ordered quasicrystals could be stable down to 0 K, *i.e.* they would be a ground state of matter. With rising temperature, local deviations from the quasiperiodic structure would increase mainly by phasonic and phononic disorder.

The other approach [related to the *random tiling* model<sup>3</sup>] says that quasicrystals are high-temperature phases stabilized by configurational entropy, again mainly from phasonic disorder. Quasiperiodicity would provide maximum structural flexibility for disorder under the constraint of structures locally favoring non-crystallographic symmetry. The structure would be quasiperiodic on average only. Lowering the temperature would increase local deviations (phason strain) from the average quasiperiodicity (nuclei of periodic approximant structures are formed) until the transformation into a periodic low-temperature structure takes place. This is just an opposite behaviour of the first approach.

From these considerations it becomes clear that it is crucial to know the evolution of structural order, *i.e.* of short- and long-range correlations in quasicrystals as a function of temperature. A Patterson analysis of the diffraction intensities is a powerful tool to obtain this kind of information. By a Patterson analysis of Bragg scattering, one obtains the distance

vectors between the maxima of the electron densities. A Patterson analysis of diffuse scattering yields *real* pair-correlations between structural building units, for short Patterson vectors, and thus, a direct access to local interactions in the structure is achieved. The temperature dependent investigation of diffuse diffraction phenomena of quasicrystals will therefore be a key technique in answering the question whether or not quasicrystals are a ground state of matter<sup>4,5</sup>.

The present article reports part *A* of our study of structural ordering phenomena of decagonal Al-Co-Ni (*Edagawa-phase*<sup>6</sup>) as a function of temperature. It mainly deals with the Patterson analysis of experimental diffuse scattering. A new method is presented that allows the removal of Bragg reflections from the full 3D diffraction data set. Part *B* focuses on the modelling of structural disorder. Phasonic diffuse scattering (*PDS*) and thermal diffuse scattering (*TDS*) have been simulated on a model system, a vertex decorated rhombic Penrose tiling, as well as based on synchrotron diffraction data of the *Edagawa-phase*. Both parts, *A* and *B*, only deal with the diffuse scattering in the Bragg layers related to the average  $\approx 4$  Å period along the tenfold axis of the basic structure and not that originating from the  $\approx 8$  Å superstructure.

## II. PREVIOUS WORK

A huge amount of work has already been invested in the study of stability, structure and ordering of decagonal Al-Co-Ni [for a recent review see Steurer<sup>7</sup>]. This phase has become *the* model system for decagonal quasicrystals for several reasons: it shows an exceptionally broad stability range with a wealth of different structural ordering states as a function of composition and/or temperature; the full power of electron-microscopy and of surface imaging methods can be applied due to the short translation period along the periodic axis (2-4 atomic layers); it can be easily grown in centimeter-sized single crystals of excellent quality, which makes it well-suitable for the study of all kinds of physical properties. In the following, previous diffuse-scattering studies on the *Edagawa-phase* are briefly reviewed. For a general review on diffuse scattering in quasicrystals see Steurer and Frey<sup>4</sup>.

The *Edagawa-phase (superstructure type I)*<sup>6,8</sup> is a twofold superstructure along the periodic and a fivefold superstructure in lateral direction of the basic decagonal phase with a periodicity of  $\approx 4$  Å along the tenfold axis. First temperature dependent studies on decagonal  $\text{Al}_{70}\text{Co}_{13}\text{Ni}_{17}$  were performed with powder X-ray diffraction and HRTEM on quenched samples.<sup>9</sup> *In-situ* high-temperature studies on single-crystals were carried out by X-ray diffractometry.<sup>10</sup> Both experiments showed that first and second order satellites behave different as a function of temperature: second order satellites (S2) start to lose intensity between 970 and 1020K and vanish almost completely between 1070 and 1120K, while first order satellites (S1) preserve about 40% of the original intensity even at 1170K. Indexing of the satellite reflections here and in the following is after Edagawa<sup>6</sup>. The index  $h_5$  refers to the  $\approx 8$  Å superstructure. Around 1190K, S1 satellites also disappear accompanied by a strong reduction of diffuse scattering in the interlayers and the Bragg layers.<sup>5,10</sup> The diffuse intensity is fully recovered when cooled down to 300 K proving the reversibility of the underlying ordering process. Both the correlation lengths along the tenfold axis (beyond experimental resolution) and perpendicular to it (approximately 20 to 40 Å) decrease with temperature.<sup>10</sup>

Recently, Kobas *et al.*<sup>11</sup> performed simulations of disorder phenomena on decagonal  $\text{Al}_{70}\text{Co}_{12}\text{Ni}_{18}$ . Model calculations of structural disorder in 3D and phasonic diffuse scattering in 5D were presented. It was found that the overall diffuse intensity distribution of the experimental pattern can be well reproduced by an orientationally disordered Abe-cluster<sup>12</sup> as well as by *PDS* & *TDS*.

### III. EXPERIMENTAL

The diffraction experiments on single crystals with nominal composition  $\text{Al}_{70}\text{Co}_{12}\text{Ni}_{18}$  [prepared by Lemster<sup>13</sup>] were performed at the Swiss-Norwegian Beamlines (SNBL) at the European Synchrotron Radiation Facility (ESRF) in Grenoble, France. The experimental setup was as follows: *MarResearch* 345 imaging plate detector, crystal-detector distance 260.0 mm, exposure time 20 s per frame, step-scan increment at 300 K  $\Delta\phi=0.25^\circ$  and at higher temperatures  $\Delta\phi=0.5^\circ$ , wavelength  $\lambda=0.7$  Å, using a high temperature in-situ furnace under helium atmosphere.<sup>5,14,15</sup> The decagonally-prismatic shaped crystal was clamped in a bundle of  $\text{Al}_2\text{O}_3$  fibres as described in Schreuer *et al.*<sup>14</sup> and oriented with its long-axis

approximately perpendicular to the rotation axis. 720 frames were collected at 300 K, out of which the first 690 were used, because the crystal had slightly moved at the end of the measurement. 471 frames were collected at 1070 K and 360 frames were measured at 1120 K, 1145 K and 1170 K. Undistorted reciprocal-space sections were reconstructed using the program *Xcavate*.<sup>16,17</sup> They were calculated on a square grid of size 2135x2135 pixels whereas reciprocal space covers  $\pm 0.8 \text{ \AA}^{-1}$ . Crystal orientation and instrumental corrections were determined using the program *XDS*.<sup>18,19,20</sup> The reconstructed layers were integrated over  $\pm 0.0025 \text{ \AA}^{-1}$  perpendicular to the sections in order to minimize resolution effects. They were corrected for polarisation effects but neither absorption nor Lorentz corrections were applied. This is assumed to be the reason for the deviations from strict decagonal symmetry, which are apparent in some, reconstructed layers. The extent in reciprocal space recorded by the imaging plate ( $\pm 0.8 \text{ \AA}^{-1}$ ) determines also the resolution of the Patterson maps ( $1.25 \text{ \AA}$ ).

## IV. DIFFRACTOGRAPHY

### A. Introductory remarks on some particularities of quasicrystals

Provided the kinematical theory of diffraction applies, the Bragg reflection pattern of a disordered 3D periodic structure is related to the square of the Fourier transform of the average structure. The same is true for a decagonal structure with the only difference that it is the 5D average structure in the higher-dimensional description that has to be Fourier transformed and that the result has to be projected upon 3D reciprocal space. The diffuse scattering is related to the square of the Fourier transform of the differences from the average structure. The full width at half maximum (*FWHM*) of the features in the structured diffuse scattering is inversely proportional to the correlation lengths of the disordered structure.

What kind of disorder is typical for decagonal quasicrystals? Their structure can be described in terms of cluster-decorated tilings or coverings.<sup>21</sup> In case of decagonal Al-Co-Ni, this columnar cluster has a decagonal shape but its symmetry is lower, probably just mirror symmetry. Frey *et al.* discussed various types of static and dynamic disorder that exist in decagonal quasicrystals.<sup>22</sup> Some possible types of disorder can be:

- Phason flips of individual atoms due to perpendicular space fluctuations. The frequency of flips increases with temperature.<sup>23</sup> Atoms jump between two energy minima of a double-well potential. The minima have almost the same energy and are usually less than 1 Å apart.
- Phason flips of larger units like sub-clusters or clusters. The virtually large jump distances of up to 10 Å or more result from correlated simple phason flips of only a subset of atoms [see *e.g.*, Fig. 7(a) of Steurer *et al.*<sup>24</sup>].
- *Random-tiling-like* disorder.<sup>3</sup> If the matching or overlapping rules are relaxed or completely omitted, randomized tilings or coverings are formed, which may have average structures close or equal to quasiperiodic structures.<sup>25</sup>

Equilibrium random fluctuations of quasiperiodic structures under conservation of a strictly quasiperiodic average structure take place at high temperatures. In a diffraction experiment this would be reflected in *PDS*. The decagonally shaped  $\approx 20$  Å clusters forming the structure of decagonal Al-Co-Ni may also be orientationally disordered since their actual symmetry is lower than decagonal. They may also be translationally disordered along their periodic axis, *i.e.* neighbouring clusters may be shifted by a multiple of layers (preferably by multiples of two layers) without losing registry. The last two disorder models also apply to sub-clusters or super-clusters of the basic  $\approx 20$  Å cluster.

## B. Structure factor calculations

The *Edagawa-phase* can geometrically be described as a layer structure with the sequence  $A, B, A', B'$  of the four different quasiperiodic layers per  $\approx 8$  Å translation period along the decagonal axis. Physically more reasonable is the description as quasiperiodic packing<sup>21</sup> of partly interpenetrating columnar clusters ( $\approx 20$  Å in diameter) with the same layer sequence  $A, B, A', B'$  along their periodic axis.

Fourier transformation of each layer gives the complex layer form factors  $f(A)$ ,  $f(B)$ ,  $f(A')$ ,  $f(B')$ . Then, the structure factor for a stack of equidistant layers with period ... $ABA'B'$ ... along the tenfold axis reads

$$F(h_5) = f(A) + f(B) \cdot e^{2\pi i h_5 \cdot 0.25} + f(A') \cdot e^{2\pi i h_5 \cdot 0.5} + f(B') \cdot e^{2\pi i h_5 \cdot 0.75}. \quad (1)$$

By simplification the expressions for the individual reciprocal-space layers give

$$F(h_5 = 4n) = f(A + A') + f(B + B'), \quad (2)$$

$$F(h_5 = 4n + 1) = f(A - A') + i \cdot f(B - B'), \quad (3)$$

$$F(h_5 = 4n + 2) = f(A + A') - f(B + B'), \quad (4)$$

$$F(h_5 = 4n + 3) = f(A - A') - i \cdot f(B - B'), \quad (5)$$

with  $n \in \mathbb{Z}$ .  $f(A + A')$  is the Fourier transform of the superposition of layer  $A$  with  $A'$ ,  $f(A - A')$  is the Fourier transform of the difference between layer  $A$  and  $A'$  and so on. Assuming flat layers and point scatterer at rest, the structure factor is repeating with a period of four reciprocal-space layers.

Even numbered reciprocal-space layers include only information on the superposition of layers  $A$ ,  $B$ ,  $A'$ ,  $B'$ , whereby the odd numbered layers comprise information about their differences. The average over the scattering *intensities* of the even numbered layers is obtained as  $|f(A + A')|^2 + |f(B + B')|^2$  and over the odd numbered layers as  $|f(A - A')|^2 + |f(B - B')|^2$ .

### C. Experimental low- and high-temperature X-ray data

In the following, both Bragg and diffuse X-ray diffraction phenomena are described of decagonal  $\text{Al}_{70}\text{Co}_{12}\text{Ni}_{18}$  at 300 K, 1120 K and 1170 K. The  $h_1 h_2 \overline{h_2} \overline{h_1} h_5$  reciprocal-space section [Fig. 1] shows both Bragg reflections as well as diffuse scattering arranged in lines, which are all sharp along the (vertical) periodic direction. Even numbered layers contain Bragg reflections as well as diffuse scattering and will be referred to as *Bragg layers* later on.

They are subject of the present study. The odd numbered layers show diffuse scattering only and will be referred to as *diffuse interlayers*. Between 300 K and 1070 K, no significant variation of the diffraction features is observed. At 1120 K [Fig. 1(b)], however, the diffuse interlayers get broadened along the periodic direction. Up to 1170 K no further significant changes are seen. These observations are in accordance with the studies of Frey *et al.*, who also developed a tentative scenario of the related structural ordering process taking place during cooling from high temperature.<sup>26</sup>

In direct space, these observations can be explained in terms of the cluster model. At 300 K, the four-layer periodicity ( $\approx 8$  Å) within each cluster is perfectly fulfilled with a correlation length along the tenfold axis beyond the experimental resolution. At 1120 K, the correlation length of the four-layer period strongly decreases while that of the averaged two-layer period  $\dots(A+A')(B+B')\dots$  remains almost unchanged. Within the quasiperiodic layers, the former breaks down to approximately one cluster diameter ( $\approx 20$  Å) while the long-range order of the averaged  $\approx 4$  Å structure does not change as indicated by the Bragg reflections.

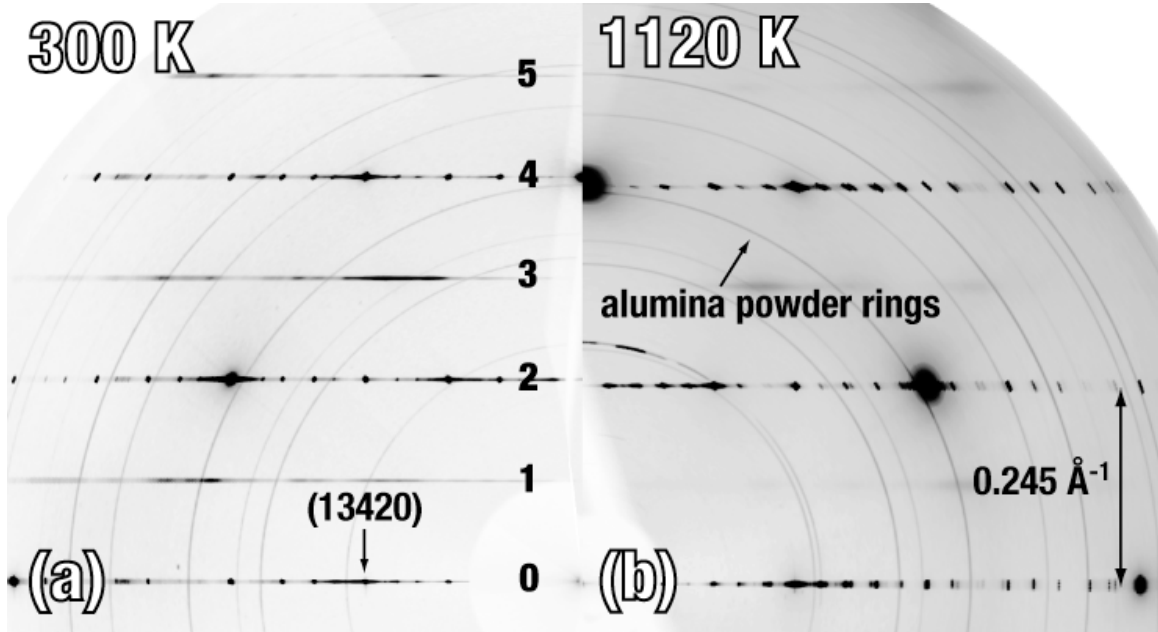


FIG. 1. The  $h_1 h_2 \overline{h_2} h_1 \overline{h_5}$  layer parallel to the periodic axis recorded at (a) 300 K and at (b) 1120 K. A sequence of layers can be recognized, which are sharp along the periodic axis and smeared out perpendicular to it. The index  $h_5$  refers to the  $\approx 8$  Å superstructure. Even numbered layers contain Bragg reflections and diffuse scattering while odd numbered layers only show diffuse scattering. Powder rings come from the alumina sample holder. At 1120 K, the odd numbered layers get clearly broadened and loose intensity. The broadening of the even numbered layers is due to the larger step-scan increment of the scan-technique.

The Laue symmetry of the total diffraction pattern as well as of just the set of Bragg reflections is  $10/mmm$  [Fig. 2]. Most of the diffuse intensity is positively correlated to the Bragg intensities, *i.e.* strong diffuse scattering can be found around strong Bragg reflections only. At ambient temperature, the diffuse intensity consists of essentially  $2D$  features, but also some weak, streak-like (*i.e.* almost  $1D$ ) intensities interconnecting main and satellite reflections can be observed. At higher temperatures streak-like diffuse scattering is dominating. Sequences of four reciprocal-space layers repeat themselves in a good approximation. Every other layer shows an essentially complementary intensity distribution [Fig. 2]. Strong intensities in one layer mostly correspond to very weak intensities at corresponding positions in the other layer. The reverse is not true: there are several regions, which show reduced intensities in both layers. This behaviour can be explained by Eqs. (2, 4). Strong intensities in one layer and weak ones in the other layer can be explained due to opposite phases of  $f(A + A')$  and  $f(B + B')$ . Weak intensities in both layers may be obtained with small values for both  $f(A + A')$  and  $f(B + B')$ . This kind of information can be used to obtain relative phases of  $f(A + A')$  and  $f(B + B')$ .

A common feature of all reciprocal layers is that the overall (*i.e.* low-frequency) intensity distribution of the diffraction patterns are almost unchanged during temperature evolution [Fig. 2(a) compared to Fig. 2(b) and Fig. 2(c) compared to Fig. 2(d)]. In contrast to that, the particular shapes of the diffuse phenomena, *i.e.* the high-frequency contributions to the diffuse intensities change drastically. With increasing temperature, first the intensities of S1 reflections clearly decrease, while those of S2 reflections increase. At the same time main reflections with large perpendicular space components of the diffraction vectors strongly increase their intensities [*cf.* Steurer *et al.*<sup>5</sup>]. At 1070 K, the diffuse intensities look alike those at 300 K. However, some precursor effects from the high-temperature regime are observable. At 1120 K, the broad diffuse features disappear almost completely and condense into relatively narrow streaks of different lengths [Fig. 2(c,d)]. They interconnect positions of main and S1 satellite reflections. Going to even higher temperatures, no significant variations can be observed compared to 1120 K. Despite all changes in the appearance of the diffuse intensities inside the quasiperiodic layers, their profiles along the tenfold axis do not change as a function of temperature indicating preservation of the long-range correlation of the average  $\approx 4$  Å periodicity up to high temperatures as long as differences between  $A$  and  $A'$  as well as  $B$  and  $B'$  are ignored.



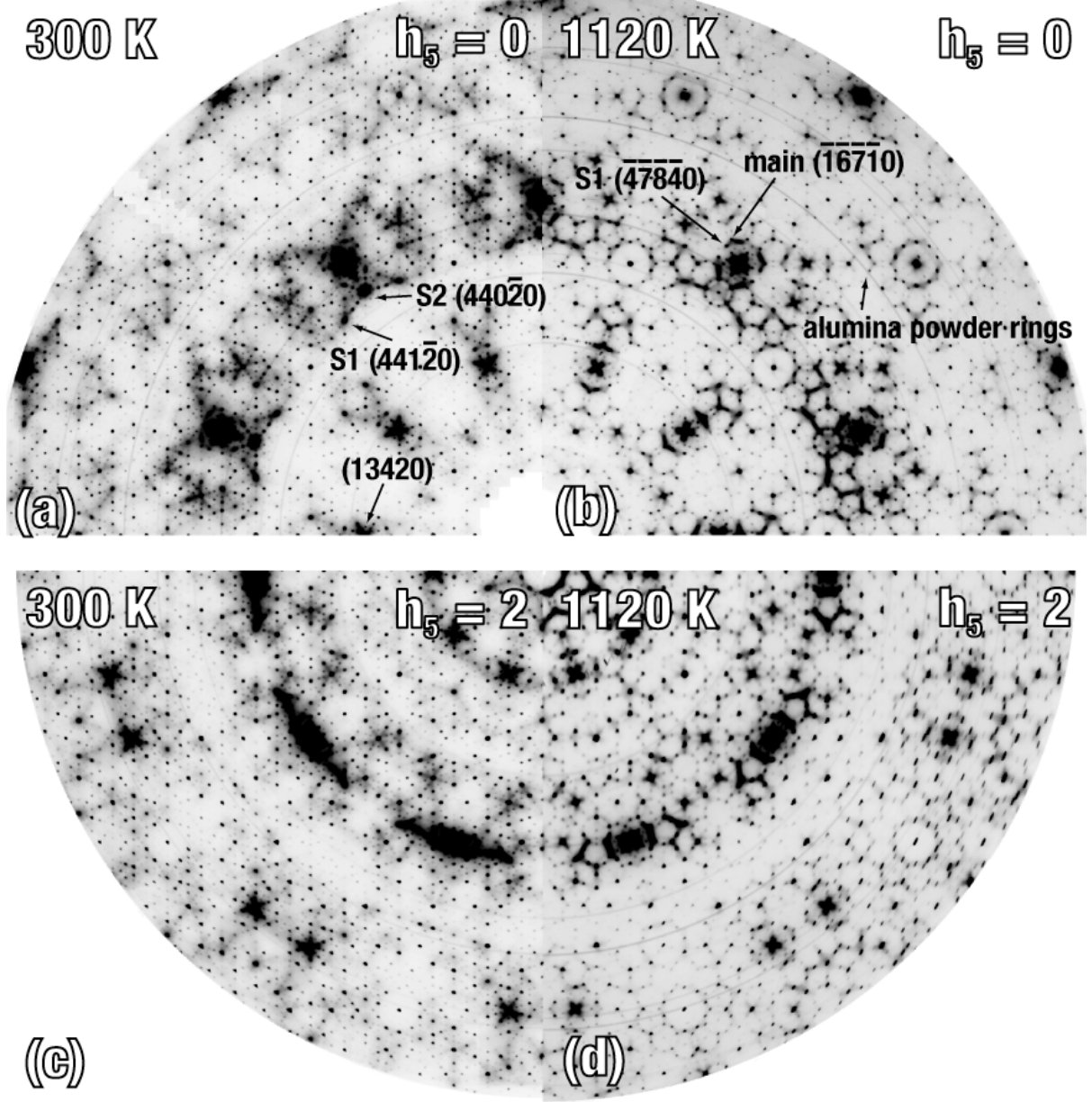


FIG. 2. The  $h_1h_2h_3h_40$  layer at (a) 300 K, at (b) 1120 K, the  $h_1h_2h_3h_42$  layer at (c) 300 K and at (d) 1120 K. The extent of the reciprocal-space patterns is  $\pm 0.8 \text{ \AA}^{-1}$ . The overall intensity distribution of the diffraction pattern are almost unchanged during temperature evolution. In contrast to that, the particular shapes of the diffuse phenomena, *i.e.* the high-frequency contributions change drastically. The streaks at 1120 K interconnect positions of main and first order satellite reflections [indexing of the satellite reflections is after Edagawa<sup>6</sup>].

In direct space, these observations can be interpreted mainly by a variation of the correlation lengths with temperature. Structural changes must be related to a reorganisation of clusters or super-clusters. The evolution of streak-like scattering at higher temperatures can be explained by the formation of correlations between these big structural units.

## V. PATTERSON ANALYSIS OF DIFFUSE SCATTERING

In this chapter, the *punch-and-fill* method is presented, which is our first approach to the development of a method that allows separation of diffuse and Bragg scattering from full 3D diffraction data. The method is not restricted to quasicrystals. It follows the derivation of the mathematical formulation of the method, the influence of chosen parameters and the application of the method to the experimental diffraction data. All following representations using five indices (for example  $h_1h_2h_3h_4h_5$ ) refer to the  $D$ -basis, whereas representations using three indices (for example  $J(h,k,l)$ ) refer to the parallel-space part of the  $V$ -basis [see Steurer *et al.*<sup>27</sup>].

### A. The *punch-and-fill* method

Structural disorder phenomena cause deviations from an averaged structure (Bragg reflections only) and contribute to the intensity distribution in reciprocal-space in terms of (continuous) diffuse scattering. The electron density distribution of a disordered structure can be written as

$$\rho(\mathbf{r}) = \rho_{aver}(\mathbf{r}) + \Delta\rho(\mathbf{r}). \quad (6)$$

$\rho_{aver}(\mathbf{r})$  is the electron density distribution of the averaged structure and  $\Delta\rho(\mathbf{r})$  represents the deviation therefrom. If an average periodic lattice of a real, disordered structure can be defined meaningfully, the total diffracted intensity  $J(\mathbf{r}^*)$  can be obtained as<sup>28</sup>

$$J(\mathbf{r}^*) = |F(\mathbf{r}^*)|^2 = |F_{aver}(\mathbf{r}^*) + \Delta F(\mathbf{r}^*)|^2 = |F_{aver}(\mathbf{r}^*)|^2 + |\Delta F(\mathbf{r}^*)|^2. \quad (7)$$

$F(\mathbf{r}^*)$  is the Fourier transform of  $\rho(\mathbf{r})$ ,  $F_{aver}(\mathbf{r}^*)$  is the Fourier transform of  $\rho_{aver}(\mathbf{r})$  and  $\Delta F(\mathbf{r}^*)$  is the Fourier transform of  $\Delta\rho(\mathbf{r})$ . The Patterson (autocorrelation) function  $P(\mathbf{r})$  is obtained by Fourier transformation of  $J(\mathbf{r}^*)$ . The basic idea of the *punch-and-fill* method concerns the elimination of  $|F_{aver}(\mathbf{r}^*)|^2$  from the total diffracted intensity.

The reciprocal lattice function, which consists of a series of  $\delta$ -functions with their centers at the positions of Bragg reflections, can be written as

$$g(\mathbf{r}^*) = \sum_{\mathbf{R}^*} \delta(\mathbf{r}^* - \mathbf{R}^*). \quad (8)$$

The corresponding direct lattice is obtained by Fourier transformation and gives

$$G(\mathbf{r}) = \sum_{\mathbf{R}} \delta(\mathbf{r} - \mathbf{R}). \quad (9)$$

Here  $\mathbf{r}^*(h, k, l)$  and  $\mathbf{r}(x, y, z)$  denote position vectors and  $\mathbf{R}^*$  and  $\mathbf{R}$  projected  $5D$ -lattice vectors in  $3D$  reciprocal and direct space respectively. Further, a window-function  $w(\mathbf{r}^*)$  is defined as a function with  $w(\mathbf{r}^*) = 1$  inside a certain region in reciprocal-space and  $w(\mathbf{r}^*) = 0$  elsewhere. The aim of the window-function is to mask the Bragg intensities.  $W(\mathbf{r})$  is the Fourier transform of the window-function. The punch-function, which removes the Bragg intensities in reciprocal-space, is now defined as (for non-overlapping windows)

$$s(\mathbf{r}^*) = 1 - g(\mathbf{r}^*) \otimes w(\mathbf{r}^*), \quad (10)$$

Fourier transformation of  $s(\mathbf{r}^*)$  gives

$$S(\mathbf{r}) = \delta(\mathbf{r}) - G(\mathbf{r}) \cdot W(\mathbf{r}). \quad (11)$$

Here  $\otimes$  denotes convolution. Note that from the definition of the punch-function  $s(\mathbf{r}^*)$ , the size of the window-function is static. In reciprocal space,  $s(\mathbf{r}^*)$  has the value 0 at and around the positions of Bragg reflections and 1 elsewhere. In direct space, the interpretation of  $S(\mathbf{r})$  is not straightforward. The Fourier transformed window-function  $W(\mathbf{r})$  is clearly defined and has a broad distribution in direct space if  $w(\mathbf{r}^*)$  is narrow in reciprocal-space. The accessible region both in parallel and perpendicular reciprocal-space of  $g(\mathbf{r}^*)$  is limited by the experiment. Thus, the reciprocal lattice  $g(\mathbf{r}^*) = g(\mathbf{r}_{\parallel}^*, \mathbf{r}_{\perp}^*)$  corresponds to a cutout of the  $5D$

infinite lattice, which can be expressed as  $g(\mathbf{r}_{\parallel}^*, \mathbf{r}_{\perp}^*) = w(\mathbf{r}_{\parallel}^*, \mathbf{r}_{\perp}^*) \cdot g_{\infty}(\mathbf{r}_{\parallel}^*, \mathbf{r}_{\perp}^*)$ . The window-function  $w(\mathbf{r}_{\parallel}^*, \mathbf{r}_{\perp}^*)$  is limited in parallel space by the maximum diffraction angle and in perpendicular space through the observable diffraction intensities. Thus,  $g(\mathbf{r}^*)$ ,  $G(\mathbf{r})$  and  $S(\mathbf{r})$  are well defined. Figure 3 shows line scans in horizontal direction of  $S(\mathbf{r})$  [Fig. 3(a)] and  $P(\mathbf{r})$  [Fig. 3(b)] calculated from the  $h_1h_2h_3h_40$  diffraction pattern at 300 K.  $S(\mathbf{r})$  shows a strong origin peak, which is more than three orders of magnitude stronger than any of the subsidiary maxima. Minima (maxima) in  $S(\mathbf{r})$  correspond mostly to maxima (minima) in  $P(\mathbf{r})$ ; they show an opposite sign behaviour. Note that  $P(\mathbf{r})$  shows both positive and negative values since  $J(\mathbf{0})$  is not accessible. These observations are equally valid for all three examined temperature regimes.

The multiplication of the scattering intensity with the punch-function gives

$$J_p(\mathbf{r}^*) = J(\mathbf{r}^*) \cdot s(\mathbf{r}^*) = J(\mathbf{r}^*) - J(\mathbf{r}^*) \cdot [g(\mathbf{r}^*) \otimes w(\mathbf{r}^*)]. \quad (12)$$

$J_p(\mathbf{r}^*)$  represents the *punched* intensity distribution in reciprocal-space. Note that all Bragg reflections were *punched* equally by a window-function of size 9x9 pixels. Visual examination of the *punched* diffraction pattern sourced that this size allows to neglect effects like peak broadening or peak shifts, which appear in the case of phason strained crystals. In figure 4, the  $h_1h_2h_3h_40$  diffraction pattern at 1070 K is shown before and after *punching* [Fig. 4(a,b)]. Except for a few strong Bragg reflections that have not been *punched* completely, most of the Bragg intensities have been removed. The insets show line scans through the broadest Bragg reflection. The maximum residual pixel intensities are below ten percent of the Bragg peak intensity, while most other peaks have been *punched* completely. For comparison, Létoublon *et al.*<sup>29</sup> have measured diffuse scattering from icosahedral Al-Pd-Mn quasicrystals on an absolute scale and have shown that *PDS* under certain Bragg reflections peaks with intensities that reach up to ten percent of the corresponding Bragg intensity. The influence of the remaining Bragg intensities onto the Patterson function will be addressed in paragraph C of this chapter.

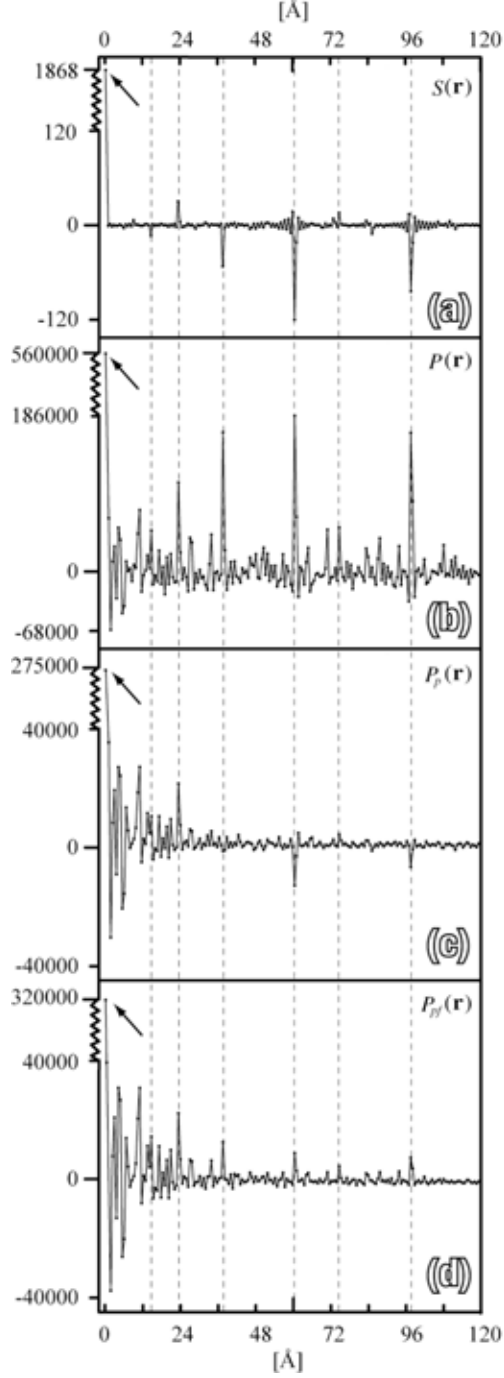


**FIG. 3.** Horizontal line scans calculated from the  $h_1h_2h_3h_40$  diffraction layer at 300 K shown for  $S(\mathbf{r})$  (a),  $P(\mathbf{r})$  (b),  $P_p(\mathbf{r})$  (c) and  $P_{pf}(\mathbf{r})$  (d).  $S(\mathbf{r})$  shows a strong origin peak, which is more than two orders of magnitude stronger than any of the subsidiary maxima. Minima (maxima) in  $S(\mathbf{r})$  mostly correspond to maxima (minima) in  $P(\mathbf{r})$ . The scan of  $P_p(\mathbf{r})$  shows basically the same distribution at short Patterson vectors as the scan of  $P(\mathbf{r})$ , indicating that the distribution of  $P_p(\mathbf{r})$  is mainly controlled by the origin peak of  $S(\mathbf{r})$  and not by the subsidiary maxima of  $S(\mathbf{r})$ . At longer Patterson vectors, the peaks in  $P_p(\mathbf{r})$  become negative, defining the region that is biased by  $S(\mathbf{r})$ . However, these peaks become again positive in  $P_{pf}(\mathbf{r})$ .

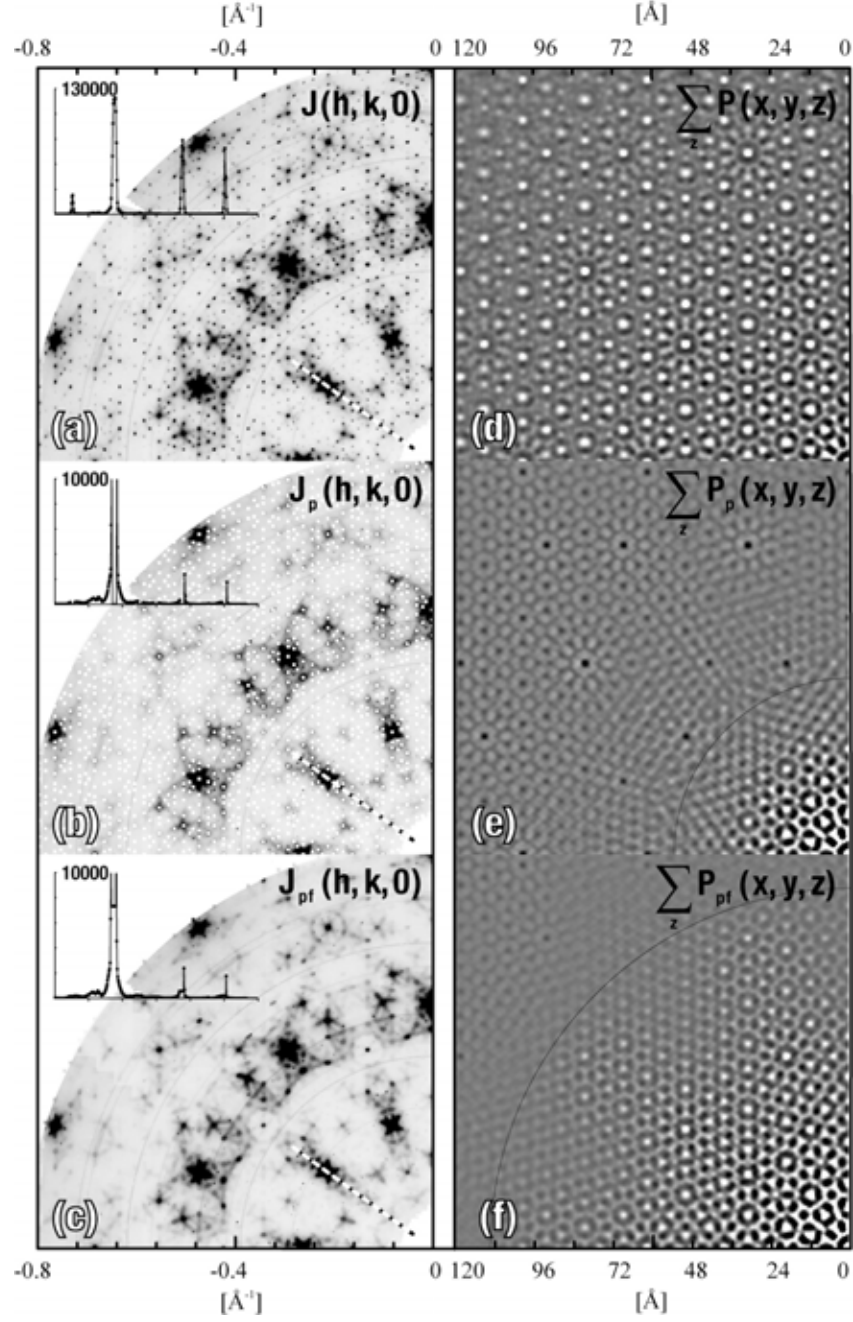


FIG. 4. The  $h_1h_2h_3h_40$  diffraction pattern at 1070 K is shown before (a) and after *punching* (b) and after *punching-and-filling* (c). Line scans of these patterns in the direction of the black-and-white dashed line are shown in the insets. The corresponding Patterson maps (*PM*) are shown in (d-f) respectively. Negative peaks are darker, positive peaks are brighter than the zero level background. The patterns in (d, e) show basically the same distribution of Patterson peaks up to  $\approx 40$  Å, which means that *punching* does not significantly influence short Patterson vectors. The influence of the punch-function onto the Patterson function becomes strong at Patterson vectors  $> 50$  Å, where the sign of the distribution in (e) turns negative (black peaks). Filling up the *punched* Bragg reflections by the fill-function moves the region dominated by the punch-function to Patterson vectors  $> 120$  Å (f). For Patterson peaks up to  $\approx 60$  Å, the pattern in (f) resembles the one in (d). Relative scaling of the intensities in the patterns (d), (e), (f) is 5:1:1.

*Punching* the Bragg reflections mainly removes the high-frequency part of scattering intensity. The low-frequency part, which mostly corresponds to the overall distribution of diffuse scattering, is hardly affected by this procedure. If the Bragg intensities are *punched* completely,  $J_p(\mathbf{r}^*)$  describes the distribution of diffuse scattering correctly at all positions in reciprocal-space except for the diffuse scattering beneath the Bragg intensities. Thus, the size of  $w(\mathbf{r}^*)$  is best chosen such that the punch-function cuts completely the strongest Bragg reflections. Fourier transformation of  $J_p(\mathbf{r}^*)$  gives

$$P_p(\mathbf{r}) = P(\mathbf{r}) \otimes S(\mathbf{r}) = P(\mathbf{r}) - P(\mathbf{r}) \otimes [G(\mathbf{r}) \cdot W(\mathbf{r})]. \quad (13)$$

What is now the influence of the punch-function in Patterson space? The horizontal line scan of  $P_p(\mathbf{r})$  in Fig. 3(c) shows basically the same distribution at short Patterson vectors as the line scan of  $P(\mathbf{r})$  [Fig. 3(b)]. Thus, the distribution of  $P_p(\mathbf{r})$  is mainly controlled by the origin peak of  $S(\mathbf{r})$  [see Fig. 3(a)] and not by the subsidiary maxima of  $S(\mathbf{r})$ . At longer Patterson vectors, the algebraic sign of the peaks in  $P_p(\mathbf{r})$  turns negative, defining the region that is biased by  $S(\mathbf{r})$ . The Patterson maps (*PMs*) of the  $h_1h_2h_3h_40$  diffraction pattern at 1070 K before and after *punching* are illustrated in Fig. 4(d, e). Negative peaks are darker, positive peaks are brighter than the zero level background. Apparently, both patterns show basically the same distribution of Patterson peaks up to  $\approx 40$  Å and the region biased by  $S(\mathbf{r})$  becomes strong at Patterson vectors  $> 50$  Å [Fig. 4(e)]. In the case of a narrow window-function  $w(\mathbf{r}^*)$ , this transition is visible at long Patterson vectors, in the case of a broad  $w(\mathbf{r}^*)$ , the transition moves to shorter vectors. The distinguished similarity between  $P(\mathbf{r})$  and  $P_p(\mathbf{r})$  [Fig. 4(d, e)] at short Patterson vectors can be explained to be due to a positive correlation between Bragg and diffuse scattering, as it is the case for our examined quasicrystal (see paragraph C of chapter V).

Filling up each *punched* region in reciprocal-space with a function  $t(\mathbf{r}^*)$ , one obtains the following expression for the *punched-and-filled* scattering intensity  $J_{pf}(\mathbf{r}^*)$

$$\Delta J(\mathbf{r}^*) \approx J_{pf}(\mathbf{r}^*) = J(\mathbf{r}^*) - J(\mathbf{r}^*) \cdot [g(\mathbf{r}^*) \otimes w(\mathbf{r}^*)] + t(\mathbf{r}^*) \cdot [g(\mathbf{r}^*) \otimes w(\mathbf{r}^*)]. \quad (14)$$

In our studies, the fill-function  $t(\mathbf{r}^*)$  was defined such that the average value of the surrounding pixel intensities around a *punched* region is assigned to the pixels inside the *punched* region. Thus, the *punched* regions are filled dynamically up to a certain threshold, the value of which depends on the intensity distribution around the *punched* region. Consequently,  $J_{pf}(\mathbf{r}^*)$  approximates the distribution of diffuse scattering, whereby the slope of the curve beneath the positions of Bragg reflections is set constant to a certain threshold value. This is an approximation to the real diffuse scattering distribution  $\Delta J(\mathbf{r}^*) = |\Delta F(\mathbf{r}^*)|^2$  [see Eq. (7)]. Note that the correct slope of the curve beneath positions of Bragg reflections in  $\Delta J(\mathbf{r}^*)$  is unknown, and thus a constant curve serves as an approximation. The *punched-and-filled* intensity distribution of  $h_1h_2h_3h_40$  at 1070 K is shown in Fig. 4(c). From the definition of  $t(\mathbf{r}^*)$  above, the Bragg reflections are not filled up to their maximum residual intensities but to an average value calculated from the intensities of the pixels around them. Fourier transformation of  $J_{pf}(\mathbf{r}^*)$  gives

$$\Delta P(\mathbf{r}) \approx P_{pf}(\mathbf{r}) = P(\mathbf{r}) - P(\mathbf{r}) \otimes [G(\mathbf{r}) \cdot W(\mathbf{r})] + T(\mathbf{r}) \otimes [G(\mathbf{r}) \cdot W(\mathbf{r})]. \quad (15)$$

$P_{pf}(\mathbf{r})$  serves as an approximation to the Patterson function of the difference structure  $\Delta P(\mathbf{r})$ . Note the similarities between the second and the third term in Eq. (15) and their opposite sign. The fill term  $T(\mathbf{r}) \otimes [G(\mathbf{r}) \cdot W(\mathbf{r})]$  (Patterson function of the diffuse scattering beneath the Bragg reflections) is a subset of  $P(\mathbf{r})$  (Patterson function of the total diffracted intensity). The horizontal line scan of  $P_{pf}(\mathbf{r})$  in Fig. 3(d) shows basically the same distribution as the line scan of  $P_p(\mathbf{r})$  [Fig. 3(c)], except for the longer Patterson vectors, which become positive again (like in  $P(\mathbf{r})$ ). The two-dimensional Patterson map (*PMs*) of the  $h_1h_2h_3h_40$  diffraction pattern at 1070 K after *punching-and-filling* is depicted in Fig. 4(f). The region dominated by  $S(\mathbf{r})$  is clearly apparent at Patterson vectors larger than  $\approx 120$  Å. The pattern in (f) shows basically the same distribution of Patterson peaks up to  $\approx 60$  Å as the *PM* depicted in (d). Vectors between  $\approx 60$  Å and  $\approx 100$  Å in Fig. 4(f) show a star-like distribution of Patterson peaks, which is not observable in the *PM* of Fig. 4(d). The origin of this distribution is addressed in paragraph C of this chapter.



## B. Dependence of the *punch-and-fill* method on the observed reciprocal space density

The set of all Bragg diffraction vectors  $\mathbf{R}^*$  of a decagonal quasicrystal forms a  $\mathbb{Z}$ -module  $M^* = \{\mathbf{R}_{\parallel}^* = \sum_{i=1}^5 h_i \mathbf{a}_i^* | h_i \in \mathbb{Z}\}$  of rank 5 in  $3D$  physical space.<sup>30</sup> This means that Bragg reflections densely fill reciprocal space. Due to experimental limitations, however, Bragg reflections can only be observed for a subset of this  $\mathbb{Z}$ -module. One limit is set by the maximum diffraction angle  $\Theta_{\max}$ , the other by the minimum detectable intensity (sensitivity of the detection system). The Bragg reflection intensity falls off drastically with increasing perpendicular-space component of the diffraction vectors

$$d_{\perp}^* = \left\{ \left\| \sum_{i=0}^4 h_i \mathbf{a}_i^* \right\| \mid h_i \in \mathbb{Z} \right\}. \quad (16)$$

Thus, by varying  $d_{\perp}^*$ , the density of the punch-function [Eq. (10)] can be triggered. For our synchrotron datasets, a punch-function, dense enough to *punch* even the weakest observable Bragg reflections, would lead to a very 'pitted' diffraction pattern. Thereby, almost all diffuse scattering information would be lost. Therefore, the maximum value  $d_{\perp, \max}^*$  has to be chosen carefully.

Our study on the influence of the punch-density onto the Patterson function  $P_{pf}(\mathbf{r})$  [Eq. (15)] shows the following: hardly any observable differences can be found for vectors up to  $\approx 110 \text{ \AA}$  for a wide variation of the punch-density. Since Patterson vectors of the difference structure larger than  $110 \text{ \AA}$  are not accessible by the proposed method and our dataset, the influence of the punch-density is negligible. In our calculations,  $d_{\perp, \max}^*$  was set to  $1.4 \text{ \AA}^{-1}$  for all examined temperature regimes, which corresponds to the maximal value for non-overlapping windows of size  $9 \times 9$  pixels.

### C. Evaluation of experimental diffraction data

The scattering intensity in any reciprocal-space region affected by parasitic scattering from the sample environment (sample holder, high temperature in-situ furnace) has been set to zero as well as the blind areas originating from the rotation-method employed and from the beam stop. Then, the data has been averaged under  $mm$ -symmetry in the following way: symmetry equivalent positions are averaged if both positions have an intensity-value different from zero. Otherwise, the position with zero intensity receives the intensity-value of the other position. After this averaging process, the positions of the Bragg reflections have been determined by overlaying a  $\mathbb{Z}$ -module with  $d_{\perp, \max}^* = 1.4 \text{ \AA}^{-1}$ . Subsequently, the Bragg reflections have been *punched* with  $w(\mathbf{r}^*)$  being fixed to a square of 9x9 pixels. The *punched* regions have been refilled by assigning to them the average value of the pixel intensities surrounding the *punched* region.

The resulting diffraction patterns served now as a basis for the calculation of the Patterson function of the difference structure, which is defined as

$$\Delta P(x, y, z) = \sum_h \sum_k \sum_l \Delta J(h, k, l) e^{2\pi i(hx + ky + lz)}. \quad (17)$$

Therewith, the projected  $PMs$ , the one at  $z = 0$  and at  $z = 0.25$  have been calculated from the Bragg layers  $\{hkl \mid -3 \leq l \leq 3\}$ . All  $PMs$  depicted in the article have been smoothed by convoluting the  $PMs$  twice with a pyramidal matrix according to

$$\Delta P_{smooth}(x, y, z) = \begin{pmatrix} 1 & 1 & 1 \\ 1 & 2 & 1 \\ 1 & 1 & 1 \end{pmatrix} \otimes \begin{pmatrix} 1 & 1 & 1 \\ 1 & 2 & 1 \\ 1 & 1 & 1 \end{pmatrix} \otimes \Delta P(x, y, z). \quad (18)$$

This procedure, well known from multi-dimensional digital image processing, minimizes truncation effects from the Fourier transformation. Back transformation of the smoothed  $PMs$  shows that the extent in reciprocal-space in directions perpendicular to the periodic axis is reduced to approximately  $\pm 0.5 \text{ \AA}^{-1}$ , resulting in an effective resolution of  $\approx 2.0 \text{ \AA}$  in the  $PMs$ . Thus, smoothing influences the direct neighbourhood of Patterson peaks but not their global

distribution in Patterson space. In some exceptional cases, smoothing can change the algebraic sign of Patterson peaks. This happens if weak, positive (negative) peaks are surrounded by strong, negative (positive) peaks. In such a case, the weak peak may change its algebraic sign after smoothing. Despite of the reduction of the resolution in Patterson space, smoothing is a useful tool to minimize truncation effects and thus prevents the interpretation of effects, which have been introduced artificially.

To estimate the influence of artifacts originating from the width of the window-function, Fourier filters were applied to the *PMs*. Figure 5 shows the projected *PM* at 300 K. The region of this *PM* containing information not biased by the punch-function amounts to  $\approx 110$  Å. Beyond this range, the *PMs* are clearly biased by  $S(\mathbf{r})$ . By applying Fourier filters to the projected *PMs* of Fig. 5 it becomes obvious that Patterson peaks in the range between 63 Å and 120 Å [Fig. 5(c)], which show a star-like distribution, result from remaining high-frequency contributions in the corresponding diffraction pattern [Fig. 5(d)]. These contributions are caused by weak Bragg reflections that have not been *punched* at all and by Bragg reflections that have not been *punched* completely. Former is limited by the chosen punch-density, latter by the fixed size of the window-function. Arrows in Fig. 5 mark some partly *punched* Bragg reflections. By Fourier filtering it is also shown that in the range below 63 Å, the Patterson peaks [Fig. 5(e)] nicely reproduce the experimental diffuse scattering [Fig. 5(f)]. This observation is equally valid for all three examined temperature regimes. Line scans in the insets show that the spiky relicts in the diffraction patterns, which have been introduced by *punching-and-filling* have their origin in Patterson vectors larger than 110 Å. To summarize, only Patterson vectors smaller than  $\approx 63$  Å reflect reliable information on structural disorder.

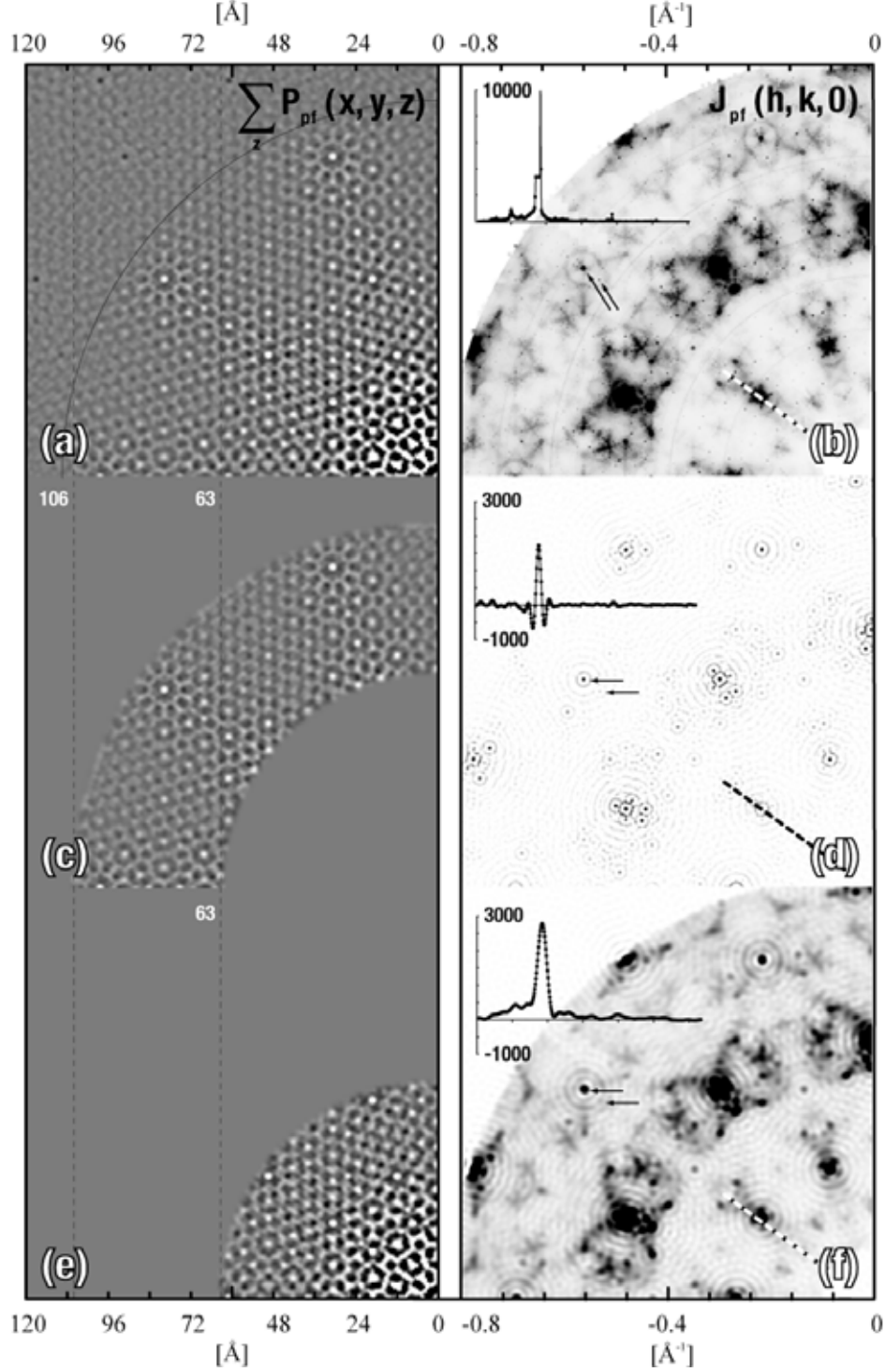


FIG. 5. Projected  $PM$  at 300 K (a) and the corresponding zeroth layer diffraction pattern (b). The region of this  $PM$  beyond  $\approx 110$  Å is dominated by the punch-function. The application of Fourier filters shows that Patterson peaks in between 63 Å and 120 Å (c) result in high-frequency contributions to the diffraction pattern (d). These contributions are caused by weak Bragg reflections that have not been *punched* at all and by Bragg reflections that have not been *punched* completely. Fourier filtering also shows that Patterson vectors smaller than 63 Å (e) nicely reproduce the experimental diffuse scattering (f). Line scans in direction of the black-and-white dashed line show that the spiky relicts in the diffraction patterns, which have been introduced by *punching-and-filling* have its origin at Patterson vectors larger than 110 Å. The intensities in the patterns (a), (c), (e) are on the same scale.

## VI. RESULTS AND DISCUSSION

By Patterson analysis of diffuse scattering data one obtains all inter-atomic vectors of the difference structure between the disordered structure and the average structure. Positive (negative) peaks mean that the corresponding inter-atomic vectors of the real structure occur more (less) frequently than in the average structure or the atoms connected by the vectors have higher (lower) scattering power than the averaged ones.

Figure 6 shows the projected difference *PMs* based on 300 K, 1070 K and at 1120 K data. Throughout these three investigated temperature regimes, a disordered structure motif (*DSM*) with  $\approx 20$  Å diameter can be identified, which does hardly change its fine structure as a function of temperature. This corresponds in size to the clusters reported in literature [for an overview see Steurer, Ref. 7]. Simulations of disorder phenomena explaining this fine structure will be presented in part *B*, while the present discussion is focusing on the distribution function of these *DSMs*.

The projected *PM* at 300 K [Fig. 6(a)] shows that the strongest Patterson peaks can be found within a range of  $\approx 23$  Å. At 1070 K [Fig. 6(b)], the distribution is similar to the one at 300 K, but with one significant difference. The Patterson vector at 20 Å has grown considerably in intensity (see scan in the inset), which means that inter-cluster correlations between direct neighbours of clusters are formed. At 1120 K [Fig. 6(c)], the correlations within the  $\approx 63$  Å range increase significantly. Remarkably strong is the increase in intensity of the Patterson peak at  $\approx 32$  Å (see scan in the inset). This means that inter-cluster correlations between second neighbours of clusters are significantly formed. The pronounced formation of inter-cluster correlations at 1120 K is also obvious from the presence of diffuse streaks in the diffraction patterns [see Fig. 2(b,d)]. Careful inspection of the projected *PMs* suggests that the complete patterns may be explained by the same *DSM* arranged at certain translation vectors [Fig. 6(a-c)]. Translation vectors are defined such that they point to Patterson peaks, which are surrounded by a similar pattern to the one around the origin peak. In horizontal and symmetry equivalent directions, the following sequence of translation vectors can be identified:  $\approx 23$  Å,  $\approx 38$  Å,  $\approx 61$  Å, which roughly corresponds to  $\{23 \cdot \tau^n \mid n \in \mathbb{N}_0\}$ . In vertical and symmetry equivalent directions:  $\approx 20$  Å,  $\approx 32$  Å,  $\approx 52$  Å is obtained, which is approximately  $\{20 \cdot \tau^n \mid n \in \mathbb{N}_0\}$ .

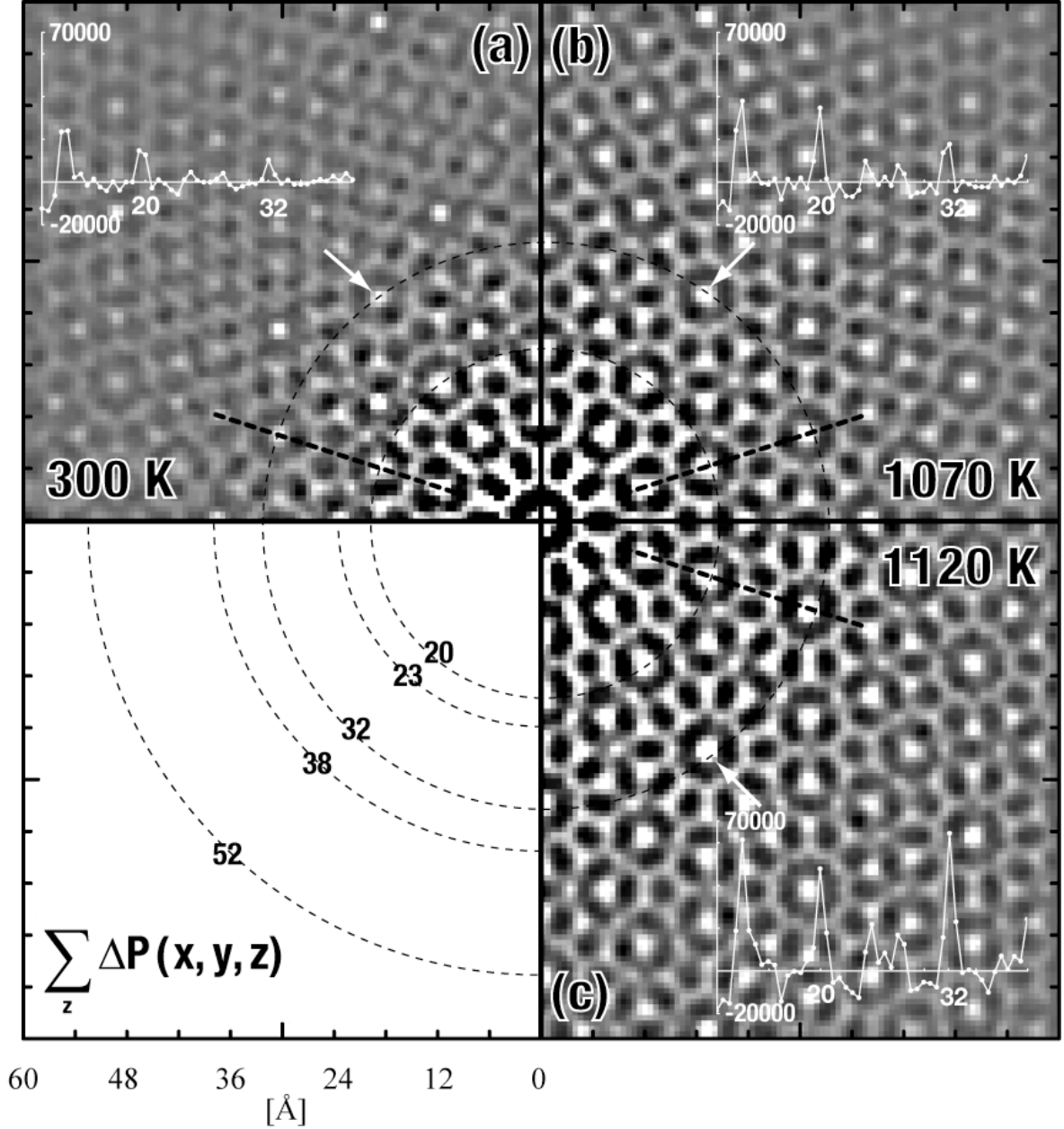


FIG. 6. Projected difference *PMs* (a) 300 K, at (b) 1070 K and at (c) 1120 K. Throughout these three temperatures, a disordered structure motif (*DSM*) with  $\approx 20$  Å diameter can be identified, which fine structure does hardly change as a function of temperature. At higher temperatures, an increase of the correlation lengths between the *DSMs* is observable. Line scans in the direction of the black dashed line are shown in the insets. They show the considerable increase in intensity of the Patterson vector at  $\approx 20$  Å at 1070K and of the Patterson vector at  $\approx 32$  Å at 1120 K. Arrows point to the prominent translation vector at 32 Å of the *DSMs*. Relative scaling of the intensities in the patterns (a), (b), (c) is 2:3:4.

These two sequences can also be identified in a quasiperiodic covering constructed of overlapping *Gummelt* decagons<sup>21</sup> [Fig. 7]. The distances between centers of decagons, which are aligned along a line mostly corresponds to one of the above sequences. The distance between two edge-sharing *Gummelt* decagons is  $\approx 20$  Å and the centers of the decagons in this

direction are separated according to  $\approx \{20 \cdot \tau^n \mid n \in \mathbb{N}_0\}$ . The distance between two corner-sharing decagons (connected by a tie) amounts to  $\approx 23 \text{ \AA}$  and the centers of the decagons in this direction are separated according to  $\approx \{23 \cdot \tau^n \mid n \in \mathbb{N}_0\}$ . This means that the translation vectors can be related to the centers of the *Gummelt* decagons.

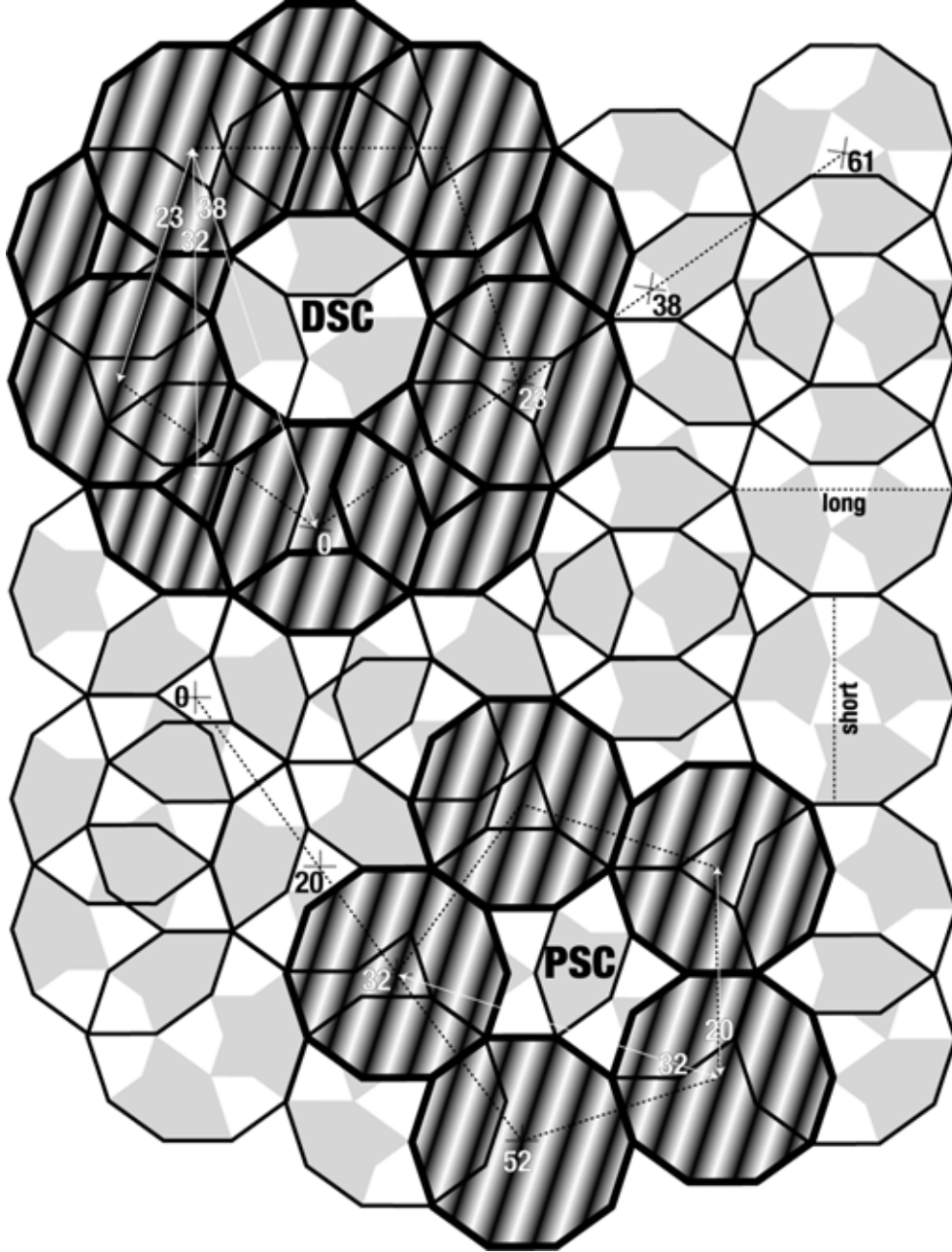


FIG. 7. Quasiperiodic covering constructed of *Gummelt* decagons<sup>21</sup>.  $\tau$ -scaled sequences of distances observed in the projected difference *PMs* are drawn in. The distance between two edge-sharing *Gummelt* decagons is  $\approx 20 \text{ \AA}$  (found in the pentagonal supercluster PSC), and between two corner-sharing decagons (connected by a tie) it amounts to  $\approx 23 \text{ \AA}$  (found in the decagonal supercluster DSC). Arrows mark inter-cluster vectors that appear in the PSC and DSC.

The *PMs* as a function of temperature may be explained as follows: both at high and low temperatures, the clusters decorate the vertices of the same quasiperiodic covering. At high temperatures, medium-range inter-cluster correlations are present, whereas at low temperatures, the ordering between the clusters becomes less pronounced. A possible disorder phenomenon that fulfills these requirements is described in Part *B* of our study. It is about phasonic induced cluster orientational disorder.

Qualitatively, the *PMs* may be interpreted by inter-cluster correlations that take place mainly inside pentagonal superclusters (PSC) below 1120 K, and inside decagonal superclusters (DSC) at 1120 K. Inter-cluster vectors that appear in the PSC (20, 32 Å) and DSC (20, 23, 32, 38 Å) are depicted in Fig. 7. These distance vectors are in accordance with the strong Patterson peaks found at the positions of translation vectors (see above). Figure 8 schematically illustrates the structure of the two types of superclusters. The PSC is composed of five *Gummelt* clusters at the corners of a star-centered pentagon with  $\approx 20$  Å edge length; the DSC consists of one central *Gummelt* cluster edge-joiningly surrounded by a ring of ten further overlapping *Gummelt* clusters. The PSCs appear in two orientations, which differ by  $36^\circ$ . The DSC can also be considered as being composed of five interpenetrating PSCs centered at the corners of a pentagon with  $\approx 23$  Å edge length.

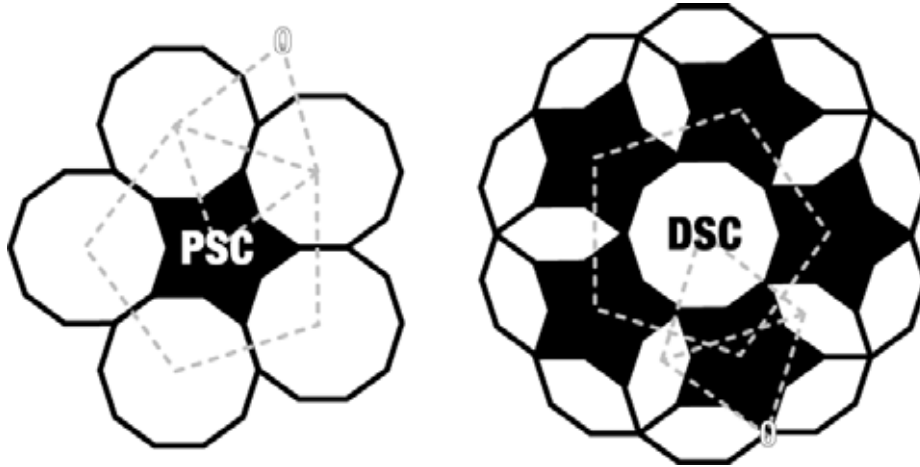


FIG. 8. Schematic illustration of the two types of superclusters. The PSC consists of five *Gummelt* clusters at the corners of a star-centered pentagon with  $\approx 20$  Å edge length; the DSC is composed of one central *Gummelt* cluster edge-joiningly surrounded by a ring of ten further overlapping *Gummelt* clusters. The DSC can also be imagined as being composed of 5 PSCs centered at the corners of a pentagon with  $\approx 23$  Å edge length. Pentagon vertices of *PMs* calculated from S1 and S2 satellite reflections are drawn as gray dashed lines. The pentagon vertices from S1 reflections can be found inside the PSC and from S2 reflections inside the DSC. In the former case, the vertices are located at the centers of the outer *Gummelt* decagons, while in the latter case, the vertices are located at the corners of the stars.



The difference *PMs* at  $z = 0$  [Fig. 9] comprise information about Patterson vectors located inside the quasiperiodic planes. The *PMs* at  $z = 1/4$  [Fig. 10] are composed of Patterson peaks on vectors pointing towards adjacent quasiperiodic layers. The *PMs* at  $z = 0$  and  $z = 1/4$  have the following points in common with the projected *PMs*: they show an increase in correlation lengths with increasing temperature and the strong Patterson peaks, which were found at the positions of translation vectors identified in the projected *PMs*, can also be found in these *PMs*. Major parts of the *PMs* at  $z = 0$  and  $z = 1/4$  are complementary, alike the reciprocal layers  $h_1h_2h_3h_40$  and  $h_1h_2h_3h_42$  [see Fig. 2]. Note the remarkable weaker intensities of the Patterson peaks at the positions of translation vectors in the *PMs* at  $z = 1/4$  [Fig. 10] in comparison to ones in the *PMs* at  $z = 0$  [Fig. 9]. This means that inter-cluster correlations between adjacent quasiperiodic layers are less pronounced than inter-cluster correlations inside quasiperiodic layers. Note the origin peak in the *PM* at  $z = 1/4$  at 300 K [Fig. 10(a)], which has become negative by smoothing. This may be understood by the effect described in paragraph C of chapter V, *e.g.* weak peaks, which are surrounded by strong peaks, may change their algebraic sign after smoothing.

From the investigations of Steurer *et al.*<sup>5</sup> on the superstructure of decagonal  $\text{Al}_{70}\text{Co}_{12}\text{Ni}_{18}$ , we know that the superstructure ordering takes place along the long and short diagonals, respectively, of a *Gummelt* decagon [see Fig. 7]. The ordering causing the S1 reflections is along the short diagonal, while the ordering of the S2 reflections is along the long diagonal of a fat Penrose rhomb. The pentagon vertices of the *PMs* calculated from S1 and S2 satellite reflections [see Steurer, Ref. 5] are drawn in Fig. 8. The pentagon vertices of the *PM* of S1 reflections can be found inside the PSC [fat dashed lines inside PSC of Fig. 8], while the ones of S2 reflections can be found inside the DSC [fat dashed lines inside DSC of Fig. 8]. In the case of the PSC, the vertices are located at the centers of the outer *Gummelt* decagons, while in the case of the DSC, the vertices are located at the centers of the stars. Note that in a certain temperature range, the intensities of S1 reflections decrease with increasing temperature while those of S2 reflections increase and that streaks interconnecting main and S1 reflections appear at 1120K. This may be explained as follows: at low temperatures, inter-cluster correlations take place predominantly in the smaller PSCs. With increasing temperature, bigger structural units are formed, the DSCs, which now govern the *PMs*. The formation of DSCs, which are composed of five interpenetrating PSCs, takes place on cost of the superstructure ordering formed by the PSCs. Thus, the S1 reflections loose intensity, while the superstructure ordering of the DSCs becomes more pronounced, *i.e.* the S2 reflections

grow in intensity. For a detailed understanding of the mechanism forming the superstructures, more studies will be necessary on the complex ordering phenomena in decagonal  $\text{Al}_{70}\text{Co}_{12}\text{Ni}_{18}$ .

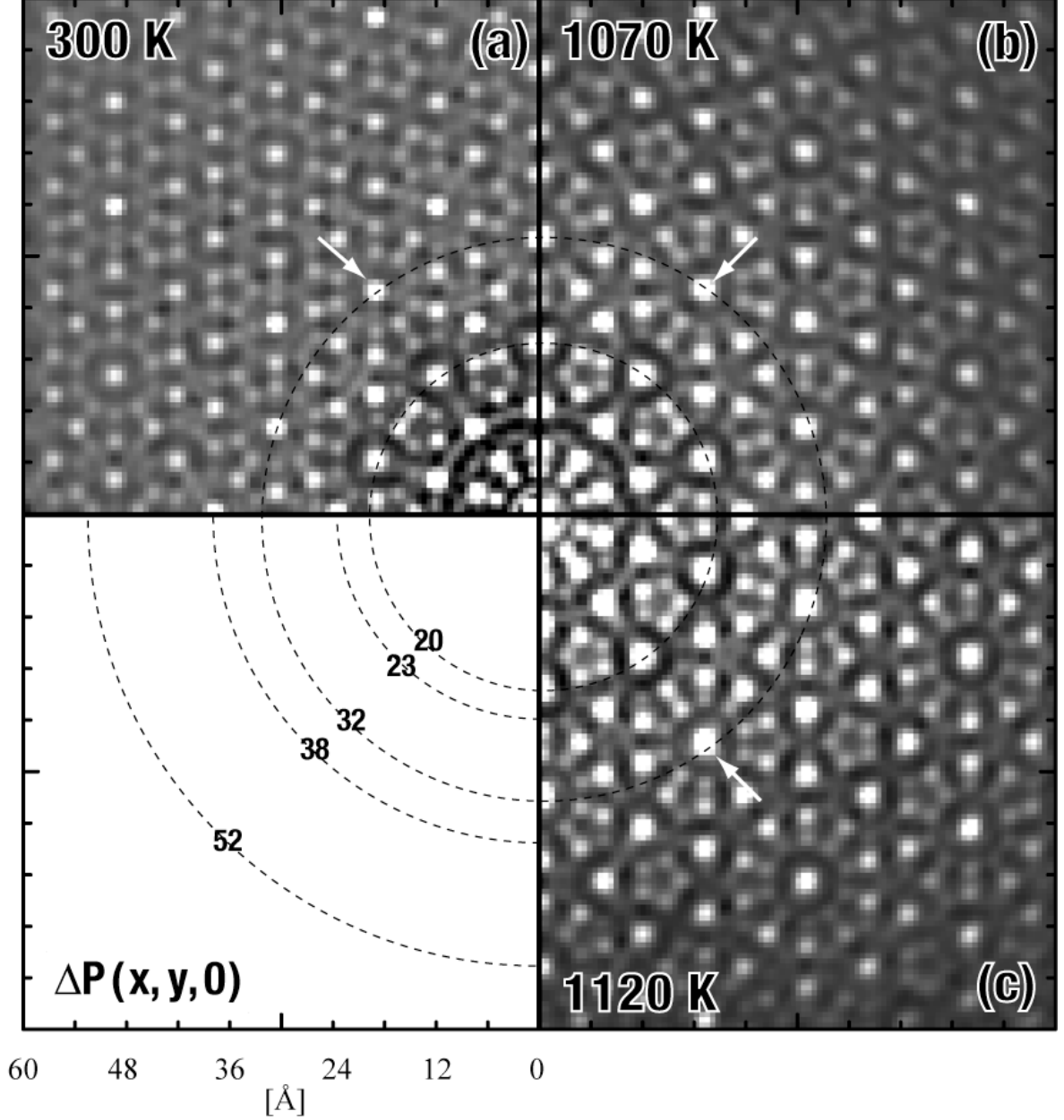


**FIG. 9.** Difference  $PMs$  at  $z = 0$  at (a) 300 K, at (b) 1070 K and at (c) 1120 K. They reflect correlated disorder of the  $DSMs$  perpendicular to the tenfold axis. At 1120 K, the correlations between the  $DSMs$  become much more pronounced. Full arrows point to the prominent translation vector at 32 Å. Relative scaling of the intensities in the patterns (a), (b), (c) is 1:2:2.

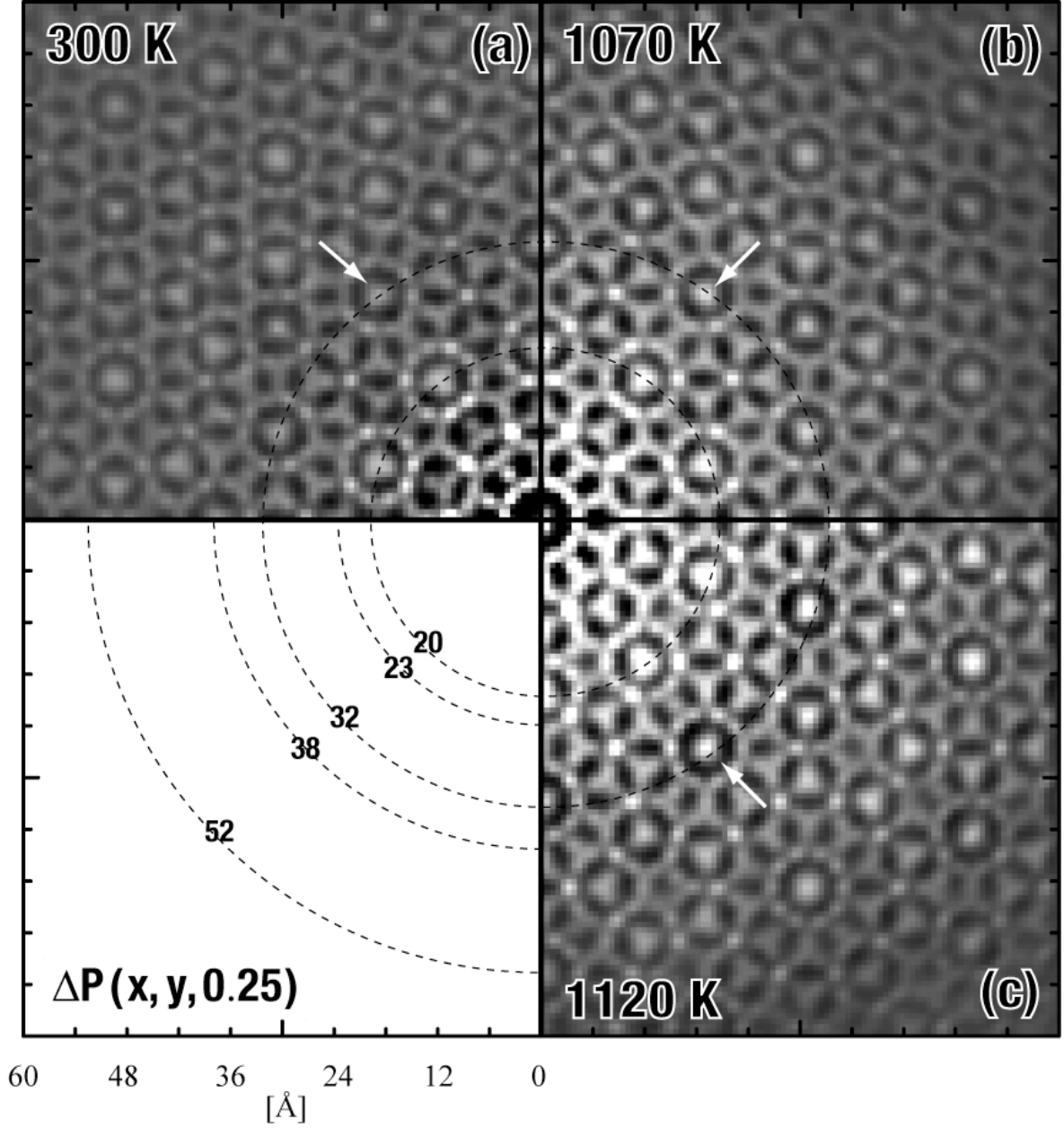


FIG. 10. Difference  $PMs$  at  $z = 1/4$  at (a) 300 K, at (b) 1070 K and at (c) 1120 K. They reflect correlated disorder of the  $DSMs$  between two adjacent layers. Full arrows point to the prominent translation vectors at 32 Å. In contrast to the  $PMs$  at  $z = 0$  [Fig. 9], the Patterson vectors at the positions of translation vectors are much weaker, but still positive. They show a slight increase in intensity at higher temperatures. Relative scaling of the intensities in the patterns (a), (b), (c) is 3:4:4.

## VII. CONCLUSIONS

Area detectors in combination with reciprocal-space reconstruction software allow 3D sampling and evaluation of X-ray intensity data. This is the prerequisite of quantitatively solving the structure of disordered complex materials such as quasicrystals. In the present study, the focus was on the application of the Patterson analysis to diffuse scattering. This powerful tool allows to obtain model-free structural information of the difference structure. The first hurdle to be taken was the reduction of the contribution from the Bragg reflections to the Patterson maps. Thus, Patterson maps were obtained, which are related to disorder only. The *punch-and-fill* method was shown to perform this task reasonably well. The Patterson maps based on *punched-and-filled* intensity data were interpreted in terms of inter-cluster correlations as a function of temperature. At high temperatures, medium-range inter-cluster correlations are present, whereas at low temperatures, inter-cluster correlations become less pronounced. The reduction of ordering between the clusters takes place without an observable change in the topology of the structure, *i.e.* the arrangement of the cluster centers.

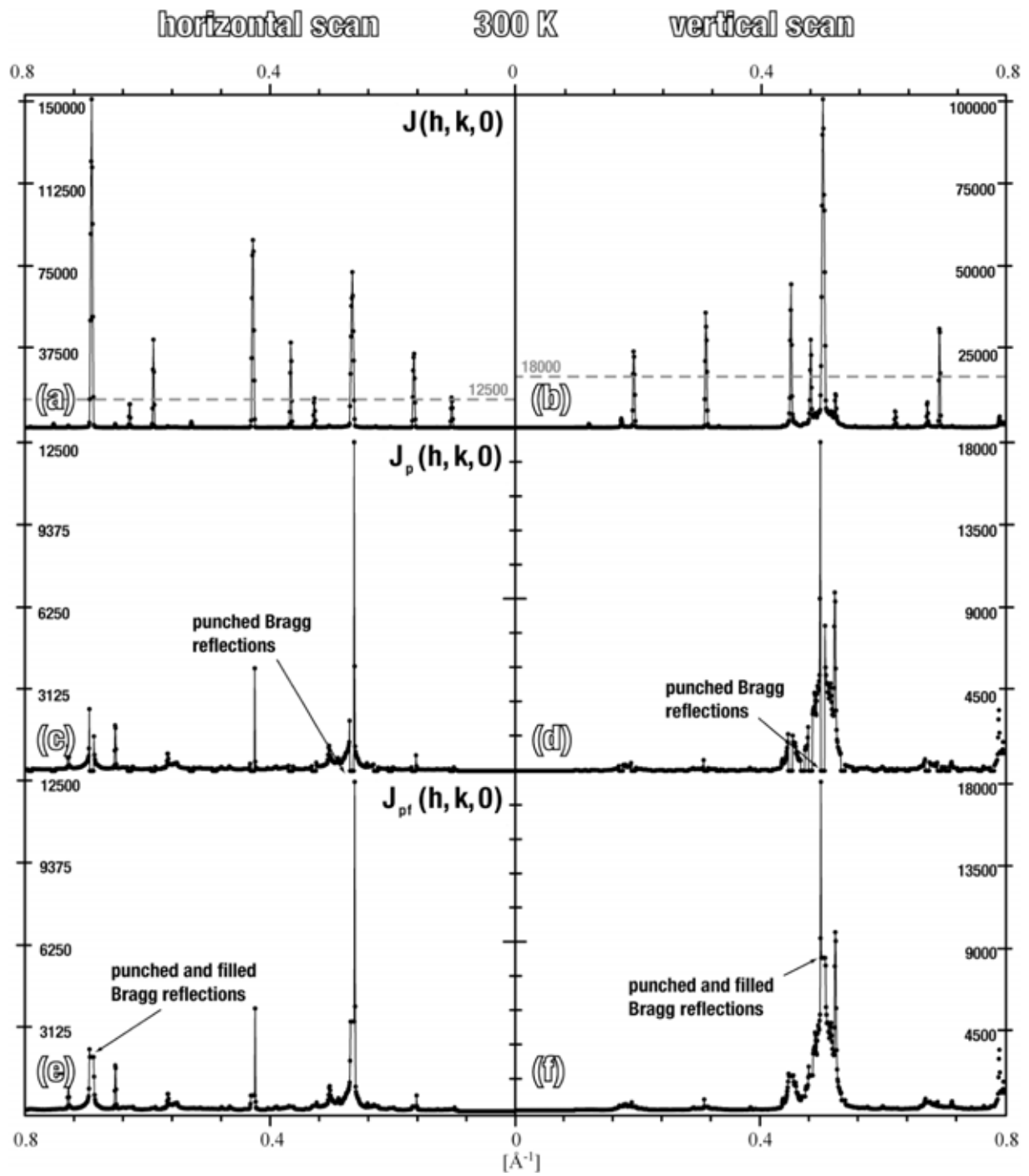
## VIII. ACKNOWLEDGMENT

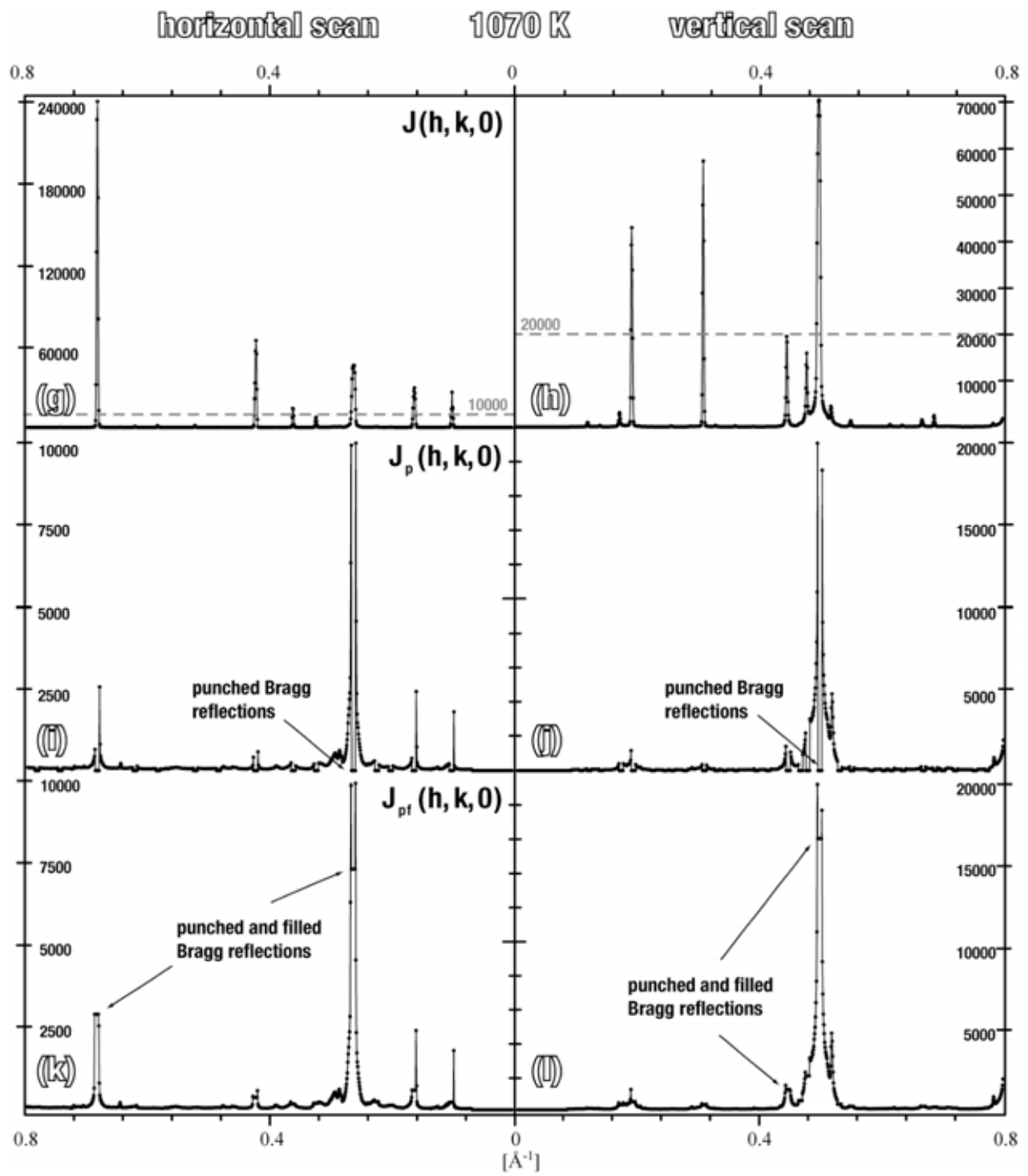
The authors would like to thank Swiss National Science Foundation for financial support by project No. 20-67872.02. We also thank F. Frey for useful comments and the staff of the Swiss-Norwegian Beam Lines (ESRF) for their assistance with the synchrotron measurements.

- 
- <sup>1</sup> A.P. Tsai, *Acc. Chem. Res.* **36**, 31-38 (2003).
- <sup>2</sup> H.C. Jeong and P.J. Steinhardt, *Phys. Rev. B* **55**, 3520-3532 (1997).
- <sup>3</sup> C.L. Henley, V. Elser, and M. Mihalkovic, *Z. Kristallogr.* **215**, 553-568 (2000).
- <sup>4</sup> W. Steurer and F. Frey, *Phase Transit.* **67**, 319-361 (1998).
- <sup>5</sup> W. Steurer, A. Cervellino, K. Lemster, S. Ortelli, and M.A. Estermann, *Chimia* **55**, 528-533 (2001).
- <sup>6</sup> K. Edagawa, H. Sawa, and S. Takeuchi, *Philos. Mag. Lett.* **69**, 227-234 (1994).
- <sup>7</sup> W. Steurer, *Z. Kristallogr.* **219**, 391-446 (2004).
- <sup>8</sup> K. Edagawa, M. Ichihara, K. Suzuki, and S. Takeuchi, *Philos. Mag. Lett.* **66**, 19-25 (1992).
- <sup>9</sup> K. Edagawa, H. Tamaru, S. Yamaguchi, K. Suzuki, and S. Takeuchi, *Phys. Rev. B* **50**, 12413-12420 (1994).
- <sup>10</sup> A. Baumgarte, J. Schreuer, M.A. Estermann, and W. Steurer, *Philos. Mag. A* **75**, 1668-1675 (1997).
- <sup>11</sup> M. Kobas, Th. Weber, and W. Steurer, *Ferroelectrics* **305**, 185-188 (2004).
- <sup>12</sup> E. Abe, K. Saitoh, H. Takakura, A.P. Tsai, P.J. Steinhardt, and H.C. Jeong, *Phys. Rev. Lett.* **84** **20**, 4609-4612 (2000).
- <sup>13</sup> K. Lemster, Ph.D. thesis ETH No. 14141, ETH Zurich, 2001.
- <sup>14</sup> J. Schreuer, A. Baumgarte, and W. Steurer, *J. Appl. Crystallogr.* **30**, 1162-1164 (1997).
- <sup>15</sup> M.A. Estermann, H. Reifler, W. Steurer, F. Filser, P. Kocher, and L.J. Gaukler, *J. Appl. Crystallogr.* **32**, 833-836 (1999).
- <sup>16</sup> M.A. Estermann and W. Steurer, *Phase Transit.* **67**, 165-195 (1998).
- <sup>17</sup> S. Scheidegger, M.A. Estermann, and W. Steurer, *J. Appl. Crystallogr.* **33**, 35-48 (2000).
- <sup>18</sup> W. Kabsch, *J. Appl. Crystallogr.* **21**, 67-71 (1988).
- <sup>19</sup> W. Kabsch, *J. Appl. Crystallogr.* **26**, 795-800 (1993).
- <sup>20</sup> W. Kabsch, *J. Appl. Crystallogr.* **21**, 916-924 (1988).
- <sup>21</sup> P. Gummelt, *Geom. Dedicata* **62**, 1-17 (1996).
- <sup>22</sup> F. Frey and E. Weidner, *Z. Kristallogr.* **218**, 160-169 (2003).
- <sup>23</sup> G. Coddens and W. Steurer, *Phys. Rev. B* **60**, 270-276 (1999).
- <sup>24</sup> W. Steurer, T. Haibach, B. Zhang, S. Kek, and R. Lück, *Acta Crystallogr. Sect. B* **49**, 661-675 (1993).
- <sup>25</sup> T.R. Welberry, *J. Appl. Crystallogr.* **24**, 203-211 (1991).

- 
- <sup>26</sup> F. Frey, E. Weidner, K. Hradil, M. De Boissieu, A. Létoublon, G. McIntyre, R. Currat, and A.P. Tsai, *J. Alloys. Comp.* **342**, 57-64 (2002).
- <sup>27</sup> W. Steurer and T. Haibach, in *International Tables for Crystallography*, 2nd edition, edited by U. Shmueli (Kluwer Academic Publishers, Dordrecht/Boston/London, 2001), Vol. **B**, Chap. 4, p.486-532.
- <sup>28</sup> J.M. Cowley, *Diffraction Physics*, 3rd edition (Elsevier Science B.V., Amsterdam, 1995)
- <sup>29</sup> A. Létoublon, M. De Boissieu, M. Boudard, L. Mancini, J. Gastaldi, B. Hennion, R. Caudron, and R. Bellissent, *Philos. Mag. Lett.* **81**, 273-283 (2001).
- <sup>30</sup> Z.M. Stadnik, *Physical Properties of Quasicrystals*, 1st edition (Springer, Berlin; Heidelberg; New York; Barcelona; Hong Kong; London; Milan; Paris; Singapore; Tokyo, 1999), Chap. 3.

## 3.2 Appendix







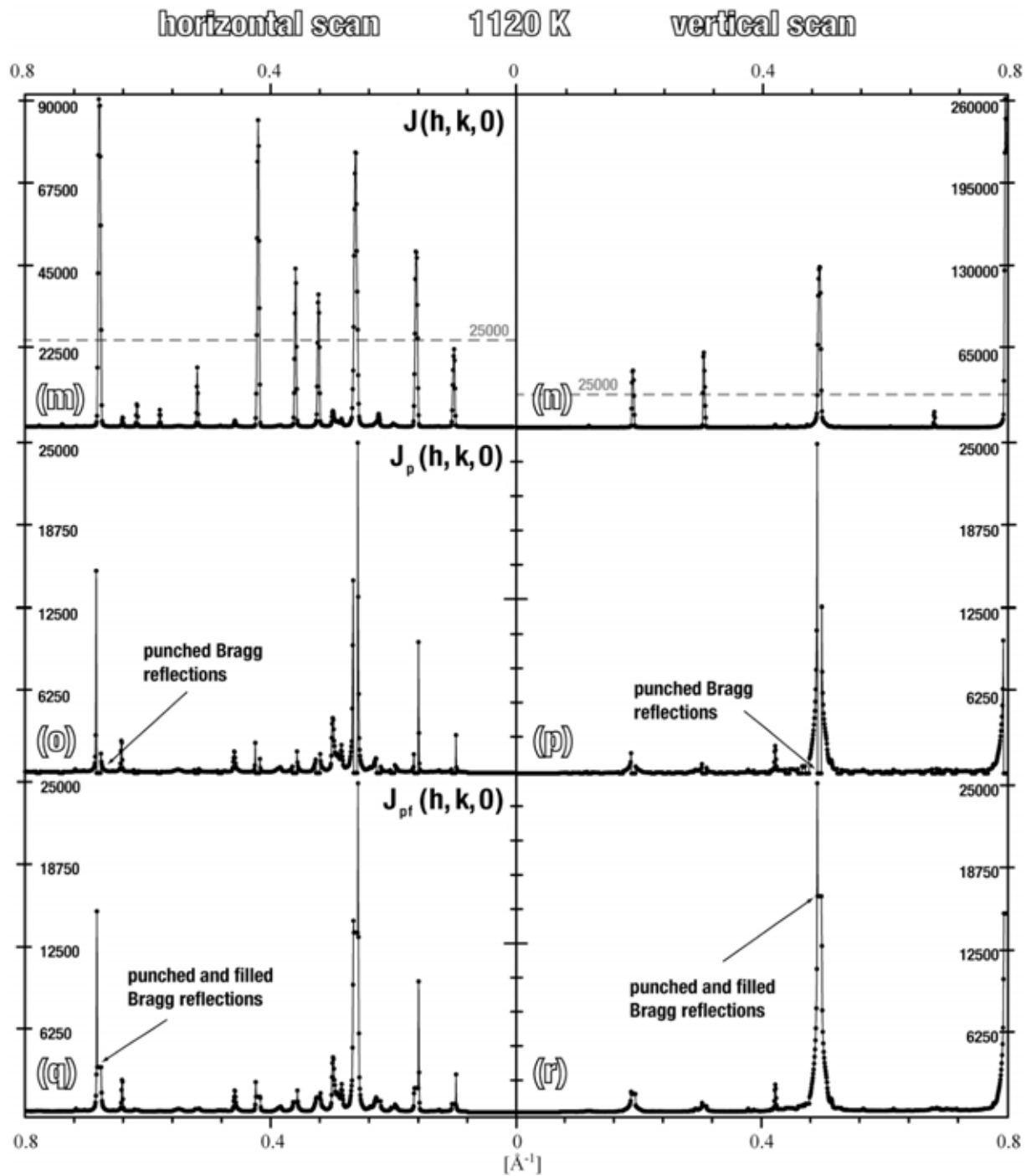


**Fig. 1:** These figures show the complete scans in horizontal and vertical direction of the  $h_1h_2h_3h_40$  diffraction patterns at the examined temperatures [cf. to Fig. 4(a-c) of article I]. (a, b; g, h; m, n) show the scans of the total diffracted intensity at 300 K, 1020 K and 1120 K, respectively. (c, d; i, j; o, p) depict scans of the *punched* and (e, f; k, l; q, r) scans of the *punched-and-filled* scattering intensity, respectively. Except for some strong Bragg peaks that have not been punched completely, most of the Bragg intensities have been removed. Dashed lines in (a, b; g, h; m, n) indicate the maximal remained intensity after punching.

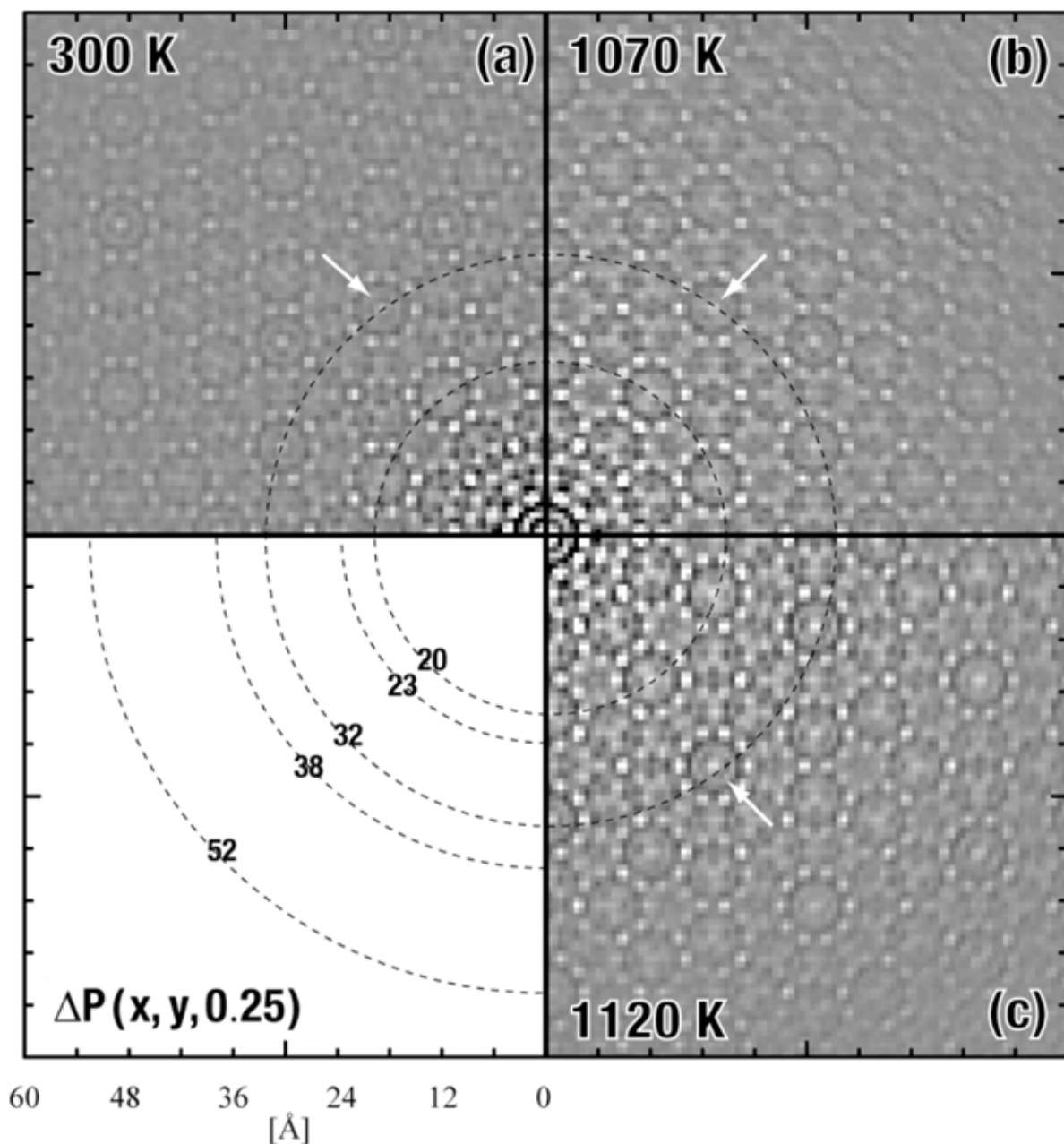


**Fig. 2:** This figure corresponds to Fig. 10 of article I, with the difference that the present *PMs* have not been smoothed. One can clearly recognize the higher resolution in the present *PMs*, which correspond to  $\approx 1.25 \text{ \AA}$ . The direct neighbourhoods of the Patterson peaks in the present case look slightly different to the ones in Fig. 10 of article I, but the global distribution of the Patterson vectors is the same. Note the origin peak at 300 K (a), which has been smoothed out in Fig. 10(a) of article I. The intensities in the patterns (a), (b), (c) are on the same scale.

## 4 Modelling structural disorder of the Bragg layers

### 4.1 Article II

This section contains a reprint of the article:

M. Kobas, Th. Weber and W. Steurer: Modelling Disorder of Decagonal Al-Co-Ni Quasicrystals. *Ferroelectrics*, **305**, 185-188 (2004).

# Modelling Disorder of Decagonal Al-Co-Ni Quasicrystals

M. KOBAS, TH. WEBER, and W. STEURER

*Laboratory for Crystallography, Department of Materials, ETH Zürich,  
 Zürich, Switzerland*

*(Received 29 August 2003; accepted 20 September 2003)*

*The question whether quasicrystals exist only on global average or also on a local scale entails the question about their stabilization. A detailed model of the real structure and temperature dependent structural changes should provide insight into this problem. Simulations of disordered structures on different scales (ranging from sub-clusters to clusters with 6–20 Å diameter) and in different dimensions (structural disorder in 3D and phasonic diffuse scattering (PDS) in 5D) were performed for decagonal Al<sub>70</sub>Co<sub>12</sub>Ni<sub>18</sub>. A good reproduction of the experimental diffuse scattering has been achieved.*

**Keywords** Quasicrystal; disorder; modelling

## 1. Introduction

One of the most challenging and still unsolved questions about quasicrystals concerns their stabilization. Energetic stabilization, i.e. optimum packing of cluster with non-crystallographic symmetry and low energy, would be reflected in PDS decreasing with temperature. In the case of entropic stabilization, the temperature dependence of PDS would be different.

From these considerations it becomes clear that it is of crucial importance to know short- and long-range correlations in quasicrystals as a function of temperature. Structure analysis based on Bragg reflections results in the space- and time-averaged structure. Detailed information about local order in disordered structures can be obtained from an analysis of diffuse diffraction intensities. Temperature dependent investigations of diffuse phenomena from quasicrystals will therefore be a key in answering the question whether entropy or energy is the driving force for stabilization of quasicrystals [1].

In the present study, we focus on X-ray scattering phenomena from a decagonal quasicrystal with nominal composition Al<sub>70</sub>Co<sub>12</sub>Ni<sub>18</sub> recorded at various temperatures from 300 K up to 1170 K. The melting temperature is approximately 1400 K. The diffraction experiments were performed at SNBL/ESRF [1] and reciprocal space sections were reconstructed using the program *Xcavate* [2]. The examined quasicrystal, the so-called Edagawa-phase [3], shows an extraordinary richness of complex scattering. The view perpendicular to the tenfold axis shows a sequence of layers that are sharp along the periodic direction. Integral layers contain Bragg reflections as well as diffuse scattering and are called ‘Bragg layers.’ They are the subject of the present study. Half-integral layers only show diffuse scattering and are discussed by Weber et al. [4].

Address correspondence to M. Kobas, Laboratory for Crystallography, Department of Materials, ETH Zürich, Zürich, Switzerland. E-mail: miroslav.kobas@mat.ethz.ch

At first glance, the diffuse intensities of the 'Bragg layers' consist of broad diffuse features. A more detailed view reveals superimposed fine structure.

In the following, three different approaches are reported. Two of them are based on concrete structural models. The third method uses an abstract concept describing disorder in higher-dimensional space.

## 2. Simulation Techniques

In the first approach, the 'molecular' form factors of about 6 Å-sized sub-clusters have been calculated. In the second approach, local disorder phenomena of about 20 Å-sized clusters were simulated. These structural modelling techniques are performed in three dimensions. The main goal is to identify essential structural building units of the quasicrystal structure. The size of the simulated models allows a reproduction of the experimental broad diffuse intensity distribution, which corresponds to a correlation length of  $\leq 20$  Å.

In the third approach, disorder related to thermal diffuse scattering (TDS) and PDS from the Edagawa-phase has been simulated in a five-dimensional approach [5]. This approach is capable to describe complex disorder in three dimensions by a few parameters in higher-dimensional space. The goal of this approach is to evaluate the importance of TDS and PDS and to explore the elastic properties of the investigated quasicrystal.

## 3. Models of Disorder

The 'molecular' form factors of several sub-clusters have been calculated. Two of them, the so-called P sub-cluster [6] and a slightly modified S sub-cluster [6], are in good agreement with experimental data (Figs. 1b–2b). The P sub-cluster [6] is an essential building unit of the Abe-cluster [7] and some other proposed clusters for decagonal Al-Co-Ni [8]. The 'molecular' form factors of these sub-clusters are shown in Figs. 1a–2a.

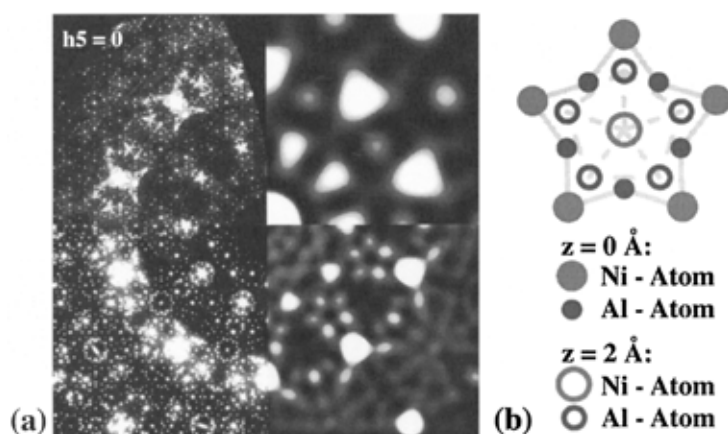


**FIGURE 1** (a) Comparison between experimental and simulated diffraction pattern. The upper left corner shows the experimental  $h_1h_2h_3h_40$ -layer (RT), the upper right corner represents the 'molecular' form factor of the modified S sub-cluster [6], the lower right corner shows the diffuse intensity of an orientational disorder of the Abe-Cluster [7] and the lower left corner displays calculated TDS and PDS of the Edagawa-phase. (b) Structure of the modified S sub-cluster [6].

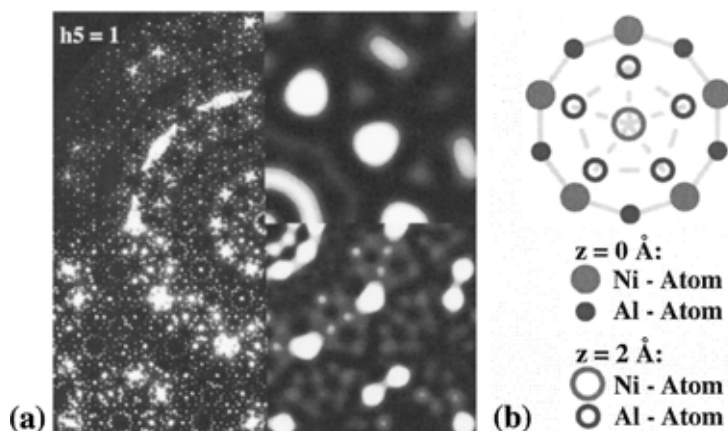


**FIGURE 2** (a) Comparison between the experimental  $h_1h_2h_3h_41$ -layer (RT) and the simulated diffraction pattern. The ‘molecular’ form factor in the upper right corner comes from the P sub-cluster [6]. Lower sections correspond to Fig. 1a. (b) Structure of the P sub-cluster [6].

Various kinds of disorder (substitutional, displacive, orientational, size-effect-like) have been simulated with numerous variations of clusters reported in literature [7–9]. Best results have been obtained by a random orientational disorder of  $n \cdot 72^\circ$ ,  $n \in \{0, 1, 2, \dots\}$  of the Abe-cluster [7] (Figs. 1a–2a).

Simulation of TDS and PDS does not require an atomic structural model but experimental Bragg intensities and elastic constants of the investigated quasicrystal. A decagonal quasicrystal can be characterized by five phononic elastic constants, three phasonic elastic constants and one phonon-phason coupling term [10]. The calculations were performed using experimentally determined phononic elastic constants [11]. For the examined Bragg layers, the number of independent phasonic elastic constants reduces to one. The phasonic elastic constant  $k_1$  has been determined by trial and error to 0.0189, the phonon-phason coupling constant  $r$  to 0.1. Both the shape of the diffuse features and the overall distribution of intensity are sensitive to a change of the elastic constants. Calculated TDS and PDS are shown in Figs. 1a–2a.

#### 4. Results and Discussion

The ‘molecular’ form factors of the simulated sub-clusters resemble the overall distribution of diffuse and Bragg scattering (Figs. 1a–2a). This is surprising since the atomic structure of the sub-clusters is simple and very small in size. It supports the theory that such building units are essential for both the average quasicrystal structure as well as for the disordered one.

The diffuse scattering of the orientationally disordered Abe-cluster [7] reproduces not only the overall diffuse intensity distribution of the experimental pattern, but also some fine structure details. An alternative description of this kind of orientational disorder is obtained by correlated substitutional and displacive disorder, which are frequently reported to be plausible disorder phenomena for decagonal  $\text{Al}_{70}\text{Co}_{12}\text{Ni}_{18}$  [1, 12].

The simulated TDS and PDS of the Edagawa-phase is in good agreement with the experimental diffraction pattern. Not only the overall diffuse intensity distribution is nicely reproduced, but also several fine structure details. It can be stated that TDS and PDS constitute the major part of the experimental diffuse intensities inside the ‘Bragg layers.’

In a next step, the three approaches will be combined by translating the results from the higher-dimensional simulations into three-dimensional structural information.

### Acknowledgment

The author would like to thank Swiss National Science Foundation for financial supporting project No. 20-67872.02.

### References

1. W. Steurer, A. Cervellino, K. Lemster, S. Ortelli, and M. A. Estermann, *Chimia* **55**, 528–533 (2001).
2. M. A. Estermann and W. Steurer, *Phase Transit.* **67**, 165–195 (1998).
3. K. Edagawa, M. Echihara, K. Suzuki, and S. Takeuchi, *Phil. Mag. Lett.* **60**, 19–25 (1992).
4. Th. Weber, M. Kobas, and W. Steurer, this issue.
5. J. Lei, R. Wang, C. Hu, and D. H. Ding, *Phys. Rev. B* **59**, 822–828 (1999).
6. K. Saitoh, K. Tsuda, M. Tanaka, K. Kaneko, and A. P. Tsai, *Jpn. J. Appl. Phys.* **36**, 1400–1402 (1997).
7. E. Abe, K. Saitoh, H. Takakura, A. P. Tsai, P. J. Steinhardt, and H. C. Jeong, *Phys. Rev. Lett.* **84**(20), 4609–4612 (2000).
8. P. J. Steinhardt, H. C. Jeong, K. Saitoh, M. Tanaka, E. Abe, and A. P. Tsai, *Nature* **396**(5), 54–57 (2000).
9. K. Hiraga, W. Sun, and A. Yamamoto, *Mater. Trans. JIM* **35**(10), 657–662 (1994).
10. C. Hu, R. Wang, W. Yang, and D. H. Ding, *Acta Cryst. A* **52**, 251–256 (1996).
11. M. A. Chernikov, H. R. Ott, A. Bianchi, A. Migliori, and T. W. Darling, *Phys. Rev. Lett.* **80**(2), 321–324 (1998).
12. F. Frey, *Mater. Sci. Eng. A* **294–296**, 178–185 (2000).

## 4.2 Article III

This section contains a reprint of the article:

M. Kobas, Th. Weber and W. Steurer: Structural disorder in decagonal Al-Co-Ni.  
Part B. Modelling. *Phys. Rev. B*, submitted.

Additional figures concerning this article are depicted in the appendix.



## Structural disorder in decagonal Al-Co-Ni.

### Part B: Modelling.

Miroslav Kobas<sup>1</sup>, Thomas Weber<sup>1</sup>, and Walter Steurer<sup>1,2</sup>

<sup>1</sup>*Laboratory of Crystallography, Department of Materials, ETH Zurich, CH-8093 Zurich, Switzerland and*

<sup>2</sup>*MNF, University of Zurich, Switzerland*

The hydrodynamic theory of phasonic and phononic disorder is applied successfully to describe the short-range, disordered structure of a decagonal  $\text{Al}_{71.5}\text{Co}_{14.6}\text{Ni}_{13.9}$  quasicrystal (*Edagawa-phase*, superstructure type I). Moreover, model calculations demonstrate that the main features of diffuse scattering can be equally well described by phasonic disorder and fivefold orientational disorder of clusters. The calculations allow to distinguish the different cluster types published so far and the best agreement with experimental data could be achieved with the mirror-symmetric Abe-cluster. Modelling of phason diffuse scattering associated with the S1 and S2 superstructure reflections indicate disorder of superclusters. The former show basically inter-cluster correlations inside quasiperiodic layers, while the latter exhibit intra- and inter-cluster correlations, both between adjacent and inside quasiperiodic layers. The feasibility, potential and limits of the Patterson method in combination with the *punch-and-fill* method employed is shown on the example of a phasonic disordered rhombic Penrose tiling. A variation of the elastic constants does not change qualitatively the way phasonic disorder is realized in the *local* quasicrystalline structure. For the same model system it is also shown that phasonic fluctuations of the atomic surfaces yield average clusters in the cut-space, which correspond to fivefold orientationally disordered clusters.

61.44.Br, 61.43.Bn, 61.10.Nz

## I. INTRODUCTION

Diffuse scattering in quasicrystals is primarily associated with phasonic diffuse scattering (*PDS*) [for a review on diffuse scattering of quasicrystals see Steurer and Frey<sup>1</sup>]. The quantitative description of phasonic diffuse scattering is based on the hydrodynamic theory using the elastic properties of a fictitious higher-dimensional hypercrystal. In particular, the distortion of the hypercrystal along perpendicular-space directions is responsible for phasonic disorder. One of the main tasks of this study was to explore the applicability of the hydrodynamic theory of *PDS* on decagonal quasicrystals and to check whether or not phasonic disorder is capable to describe the disordered structure of decagonal Al-Co-Ni. Other types of disorder phenomena for decagonal quasicrystals are known [see Frey *et al.*<sup>2</sup>] but a careful examination of this phenomena is beyond the scope of this paper. Although *PDS* has often been used to describe disorder of quasicrystals, it is quite unclear, however, what *PDS* means in terms of 3D structural disorder. Therefore, one of the tasks of this study was to explore the three-dimensional structural meaning of *PDS*. In the focus, however, was the modelling of structural disorder phenomena of decagonal Al-Co-Ni quasicrystals. Phasonic diffuse scattering and thermal diffuse scattering (*TDS*) have been calculated for a model system, a decorated rhombic Penrose tiling (*RPT*) as well as for synchrotron diffraction data taken on decagonal Al<sub>71.5</sub>Co<sub>14.6</sub>Ni<sub>13.9</sub>, a superstructure of type I [*Edagawa-phase*<sup>3</sup>]. The modelling of disorder on the scale of clusters allowed to distinguish between different cluster types suggested in literature.

In the following, we will briefly review theoretical work on *PDS* and then present current cluster models employed in our disorder model calculations.

## II. PREVIOUS WORK

### A. Theoretical work on *PDS*

Within the framework of the hydrodynamic theory, Jaric and Nelson<sup>4</sup> developed a theory of diffuse scattering from icosahedral quasicrystals due to spatially fluctuating thermal and quenched strains. This approach was extended such that it could be used also for decorated quasilattices.<sup>5,6,7</sup> Lei *et al.* discussed both quenched and thermal phasons and phonons in the case of decagonal quasicrystals.<sup>5</sup> Ishii<sup>8</sup> pointed out that anisotropic diffuse scattering of phasonic origin in decagonal quasicrystals may only be expected in the case of strong phonon-phason coupling.

Yang *et al.*<sup>9</sup> and Hu *et al.*<sup>10</sup> investigated point groups and elastic properties of pentagonal and decagonal quasicrystals. The number of independent second-order elastic constants of Laue class  $10/mmm$  has been determined: five elastic constants are associated with the phonon field, three with the phason field and one with the phonon-phason coupling. Phasonic elastic constants from geometrical random-tilings have been calculated by Monte Carlo simulations<sup>11,12,13</sup>. Zhu and Henley<sup>14</sup> have estimated the phonon-phason coupling constant from relaxation simulations of an icosahedral quasicrystal model. A similar method has been applied to a simple decagonal quasicrystal model and the full set of elastic constants has been calculated.<sup>15</sup>

The hydrodynamic theory for quasicrystals predicts that the phonon displacement field relaxes rapidly via phonon-modes, whereas the phason displacement field relaxes diffusively with much longer relaxation times.<sup>16</sup> At higher temperatures, the hydrodynamic theory treats phasons analogous to phonons, *i.e.* thermal excitations, and they are described in a unified way. At lower temperatures, however, atomic diffusion is very sluggish and phonons will equilibrate in the presence of a quenched phason displacement field.<sup>4,7,17</sup> In this case phonons and phasons have to be treated separately.

## B. Cluster models

A large number of cluster models for fundamental building units of decagonal Al-Co-Ni has been proposed [for a review see Steurer<sup>18</sup>]. In the present work, the following most reasonable models were used for modelling structural diffuse scattering phenomena:

- Abe-cluster<sup>19,20</sup>: d-Al<sub>72</sub>Co<sub>8</sub>Ni<sub>20</sub> (Ni-rich basic phase), periodicity  $\approx 4$  Å, columnar cluster with  $\approx 20$  Å diameter, mirror symmetry, forces a strictly quasiperiodic tiling.
- Hiraga-cluster<sup>21,22,23</sup>: d-Al<sub>70</sub>Co<sub>15</sub>Ni<sub>15</sub>, periodicity  $\approx 4$  Å, diameter  $\approx 20$  Å, pentagonal symmetry [Ref. 21, 22]. d-Al<sub>72</sub>Co<sub>8</sub>Ni<sub>20</sub>, diameter  $\approx 32$  Å, pentagonal symmetry [Ref. 23]. Cluster model for the *Edagawa-phase*: four-layer structure with sequence  $A, B, A', B'$ , periodicity  $\approx 8$  Å, layers  $A$  and  $A'$  are flat, layers  $B$  and  $B'$  are puckered, layers  $A$  and  $A'$  act as mirror planes between layers  $B$  and  $B'$ , diameter of  $\approx 32$  Å, pentagonal symmetry [Ref. 23].
- Ritsch-cluster<sup>24,25</sup>: d-Al<sub>72.5</sub>Co<sub>20</sub>Ni<sub>7.5</sub> (Co-rich basic phase), periodicity  $\approx 4$  Å, diameter  $\approx 20$  Å, pentagonal symmetry.
- Saitoh-cluster<sup>26</sup>: d-Al<sub>72</sub>Co<sub>8</sub>Ni<sub>20</sub> (Ni-rich basic phase), periodicity  $\approx 4$  Å, diameter  $\approx 20$  Å, mirror symmetry, consists of pentagonally shaped sub-clusters (P sub-cluster) and star-like shaped (S sub-cluster).
- Steinhardt-cluster<sup>27,28</sup>: d-Al<sub>72</sub>Co<sub>8</sub>Ni<sub>20</sub> (Ni-rich basic phase), periodicity  $\approx 4$  Å, diameter  $\approx 20$  Å, mirror symmetry, *Gummelt* cluster-covering<sup>29</sup> introduced that favours strict quasiperiodic tiling.
- Steurer-cluster<sup>30</sup>: d-Al<sub>70</sub>Co<sub>15</sub>Ni<sub>15</sub>, periodicity  $\approx 4$  Å, diameter  $\approx 20$  Å, 10<sub>5</sub> screw axis, layer A shows pentagonal symmetry, layer B mirror symmetry.
- Yan-cluster<sup>31,32,33,34</sup>: d-Al<sub>72</sub>Co<sub>8</sub>Ni<sub>20</sub> (Ni-rich basic phase), periodicity  $\approx 4$  Å, diameter  $\approx 20$  Å, substitutional disorder between transition metal (TM) atoms and Al in the core region of the cluster lowering the symmetry from pentagonal to mirror symmetry. Such a disordered model favours a random tiling structure [Ref. 31]. Slight modification based on P sub-clusters [Ref. 32-34].

All but the cluster-model of Steurer<sup>30</sup>, which has been derived by X-ray single-crystal structure analysis, are based on electron microscopy (*EM*) studies. The cluster of Hiraga<sup>21-23</sup> and Ritsch<sup>24,25</sup> exhibit  $5m$  symmetry, all other models show mirror symmetry only.

### III. EXPERIMENTAL

Alloys in the ternary system Al-Co-Ni with the nominal composition  $\text{Al}_{72.5}\text{Co}_{14}\text{Ni}_{13.5}$  were prepared by Lemster<sup>35</sup> by producing compacts (pressure of 30 kN applied for 1 min, weight 5 g) of high-purity elements under argon atmosphere (Mbraun glove box 150 B-G, PanGas Ar 99.9998%). The stoichiometric formula  $\text{Al}_{71.5}\text{Co}_{14.6}\text{Ni}_{13.9}$  was determined by electron microprobe X-ray analyser with the wavelength dispersive method (CAMECA SX50,  $\pm 0.1$  at.%). The compacts were melted twice in an arc furnace with water-cooled copper-crucible (Degussa VOLiO) for homogenisation. Afterwards they were put in an alumina crucible with top cover and were remelted in a high vacuum furnace (PVA MOV 64) under the following temperature conditions: heating up from 300 K to 1470 K in 1 h, holding the temperature for 15 min, then cooling down with a rate of 0.5 K/min to 1120 K, holding the temperature for 4 h and subsequently cooling down to ambient temperature by switching off the high-vacuum furnace. The ingots of the different compacts were crushed and single-crystals selected. The quality of the crystals was studied with X-ray photographic techniques.

The X-ray data collection of the Bragg reflection dataset (d- $\text{Al}_{71.5}\text{Co}_{14.6}\text{Ni}_{13.9}$ ) was performed at the four-circle diffractometer beamline D3 at the synchrotron source Hasylab ( $\lambda = 0.56000$  Å,  $3^\circ \leq 2\Theta \leq 140^\circ$ , 15474 reflections measured, therefrom 7058 main reflections, 4214 first order satellite reflections S1 and 4202 second order satellite reflections S2).<sup>36</sup> Indexing of the satellite reflections here and in the following is after Edagawa<sup>3</sup>. The quasicrystal parameters  $a = 3.7805(5)$  Å and  $c = 4.0816(5)$  Å are defined such that the reciprocal parameters  $a^*$  and  $c^*$  correspond to the physical reciprocal-space lengths of the (10000) and (00001) reflections in the standard embedding, respectively [see Steurer, Ref. 30].

The experimental details on the image plate datasets of the *Edagawa-phase* (d- $\text{Al}_{70}\text{Co}_{12}\text{Ni}_{18}$ ) are described in part A of our study.

#### IV. MODELLING *PDS* & *TDS* OF A RHOMBIC PENROSE TILING

A *RPT* has been constructed from its four-dimensional representation in the standard embedding as described in Cervellino *et al.*<sup>37</sup>. The centers of the atomic surfaces (*AS*) of the *RPT* occupy the positions  $\{(\frac{p}{5}, \frac{p}{5}, \frac{p}{5}, \frac{p}{5})_D | p=1, \dots, 4\}$  on the body diagonal of the four-dimensional unit-cell (subscript *D* denotes *D*-basis). The *AS*s consist of four pentagons of radius  $\frac{2a}{5\tau^2}$  at  $p=1, 4$  and of radius  $\frac{2a}{5\tau}$  at  $p=2, 3$ , where  $\tau = \frac{1+\sqrt{5}}{2}$  is the golden mean and  $a = 3.757 \text{ \AA}$  is the quasicrystal parameter. Throughout this paper, the ‘radius’ of a regular polygon is defined as its centre-to-vertex distance. Orientation of the *AS*s are according to Steurer *et al.*<sup>38</sup>. The *AS*s at  $p=1, 4$  are decorated with Ni-atoms, the ones at  $p=2, 3$  with Al-atoms. The atomic scattering factors are taken from Maslen *et al.*<sup>39</sup>. Both the anisotropic atomic displacement parameters and the anisotropic phasonic parameters are set to zero for the calculation of the diffraction patterns of the *RPT*. The atomic configurations in parallel-space are obtained through a cut of the four-dimensional embedding-space by the two-dimensional parallel-space.

##### A. Methodology: *PDS* & *TDS* calculations

For the calculation of *PDS* & *TDS* of a two-dimensional diffraction pattern, one has to solve the following expression for every single Bragg reflection [details on the theory can be found in Ref. 5-7]:

$$\Delta J(\mathbf{R}_{\parallel}^* + \mathbf{o}_{\parallel}^*) = \frac{k_B T}{(2\pi)^3} \cdot J_{aver}(\mathbf{R}_{\parallel}^*) \cdot (\mathbf{R}_{\parallel}^*, \mathbf{R}_{\perp}^*)_V \cdot \mathbf{A}^{-1}(\mathbf{o}_{\parallel}^*) \cdot (\mathbf{R}_{\parallel}^*, \mathbf{R}_{\perp}^*)_V. \quad (1)$$

$\Delta J(\mathbf{R}_{\parallel}^* + \mathbf{o}_{\parallel}^*)$  is the diffuse intensity at offset  $\mathbf{o}_{\parallel}^*$  from a particular Bragg reflection  $\mathbf{R}_D^* = (\mathbf{R}_{\parallel}^*, \mathbf{R}_{\perp}^*)_V$  (subscript *D* denotes *D*-basis, and *V* stands for the *V*-basis),  $k_B$  is the Boltzmann constant,  $T$  is the temperature,  $J_{aver}(\mathbf{R}_{\parallel}^*)$  is the Bragg scattering intensity of a

particular reflection and  $\mathbf{A}(\mathbf{o}_{\parallel}^*)$  is the hydrodynamic matrix.  $\mathbf{A}(\mathbf{o}_{\parallel}^*)$  includes information on the elastic properties of the quasicrystal and, therefore, is also a function of the phononic elastic constants  $C_{ijkl}$ , of the phasonic elastic constants  $K_{ijkl}$  and of the phonon-phason coupling constants  $R_{ijkl}$ . Note that Eq. 1 is valid in the case of simultaneously thermalized phonons and phasons ( $T \geq T_q$ , with  $T_q$  being the phason-quenching temperature). In the case of quenched phasons ( $T < T_q$ ), Eq. 1 can still be written in the same form but  $\mathbf{A}(\mathbf{o}_{\parallel}^*)$  has to be replaced by an effective hydrodynamic matrix  $\mathbf{A}_{eff}(\mathbf{o}_{\parallel}^*)$ .  $\mathbf{A}_{eff}(\mathbf{o}_{\parallel}^*)$  is associated with  $C_{ijkl}$ ,  $K_{ijkl}$ ,  $R_{ijkl}$  at temperature  $T$  but also with those at temperature  $T_q$ . Thus, the effectively needed input for the calculation of *PDS* & *TDS* are the elastic constants of the considered quasicrystal and the Bragg scattering intensities.

In order to keep computing time reasonable,  $\Delta J(\mathbf{R}_{\parallel}^* + \mathbf{o}_{\parallel}^*)$  is calculated up to an offset  $\mathbf{o}_{\parallel}^*$ , which is set dynamical for each Bragg reflection. The maximal offset  $\mathbf{o}_{\parallel, \max}^*$  for each reflection is chosen such that  $\Delta J(\mathbf{R}_{\parallel}^* + \mathbf{o}_{\parallel, \max}^*) \approx 0.0001 \cdot \Delta J(\mathbf{R}_{\parallel}^*)$ . This means that the calculated diffuse intensity at  $\mathbf{o}_{\parallel, \max}^*$  for each reflection drops to about 0.0001 of the diffuse intensity maximum in the pixel closest to the position of the corresponding Bragg reflection.

For the calculation of the Patterson function based on diffuse intensity data only, the diffuse scattering was *punched* around the location of each *measured* Bragg reflection by a small window-function. For details on the *punch-and-fill* method refer to part *A* of this study. In contrast to the punch-function used in Part *A* (window-function of size 9x9 pixels), the punch-function used for the *PDS* & *TDS* calculation is 3x3 pixels only. Its influence in Patterson-space is significant at Patterson vectors larger than 100 Å. In the case of the *PDS* & *TDS* calculation, the *punched* regions are not filled by the fill-function, as it was done for the calculations in part *A*. Although the Bragg reflections are not included, *punching* the diffuse diffraction pattern is necessary in the present case. Otherwise 'numerical singularities', which are due to sampling effects of the *PDS* & *TDS* pattern, would control the Patterson maps (*PM*) of the diffuse scattering. Apparently, equation 1 shows a singularity at the position of each the Bragg reflection: if  $\mathbf{o}_{\parallel}^*$  approaches 0,  $\Delta J(\mathbf{R}_{\parallel}^* + \mathbf{o}_{\parallel}^* \rightarrow 0)$  tends toward  $\infty$ . This is due to the

fact that intensities are calculated on discrete pixel positions ( $\infty$  appears if a Bragg position falls exactly on a discrete pixel position). This is in contrast to the experiment, where the scattering information is integrated over the area of one pixel, which results in a finite value.

All following results of the *PDS* & *TDS* calculations are based on the theory of thermalized phonons and phasons. Only minor differences in the diffraction patterns and *PMs* can be observed in the case of quenched phasons. Chernikov *et al.*<sup>40</sup> has determined the full set of phononic elastic constants for a decagonal Al-Co-Ni quasicrystal with resonant ultrasound spectroscopy at ambient temperature. Thus, for a decagonal quasicrystal with point group  $10/mmm$ , one ends up with only 4 parameters for the thermalized case but still with 13 for the quenched case.

## B. Dependence on the perpendicular-space component of diffraction vectors

What is the influence of a limitation of the perpendicular-space component of the diffraction vectors [see Eq. 16, part *A*] on the diffuse scattering (*PDS* & *TDS*) and the corresponding Patterson function? *PDS* & *TDS* of a *RPT* is calculated for two datasets with a maximal parallel-space component of  $d_{\parallel, \max}^* = 2.5 \text{ \AA}^{-1}$  and maximal perpendicular-space components of  $d_{\perp, \max}^* = 2 \text{ \AA}^{-1}$  and  $d_{\perp, \max}^* = 5 \text{ \AA}^{-1}$ , respectively. Zoomed sections of the calculated diffuse patterns are shown in Fig. 1(a, b), respectively, the corresponding *PMs* are depicted in Fig. 1(c, d). Note that all *PMs* depicted in this article have been smoothed to minimize truncation effects from the Fourier transformation (see part *A* for more details). All Bragg reflections stronger than 1 ppm of the intensity of the second strongest reflection are included in the calculations ( $J(\mathbf{0})$  excluded). This restriction gives a dataset comparable to what can be measured employing synchrotron radiation (dynamic range of  $\approx 10^6$ ). In the case of  $d_{\perp, \max}^* = 2 \text{ \AA}^{-1}$ , the datasets results in 17'300 Bragg reflections, in the case of  $d_{\perp, \max}^* = 5 \text{ \AA}^{-1}$ , one obtains 98'350 reflections. The phononic elastic constants  $C_{ijkl}$  were taken from Chernikov<sup>40</sup>, the phasonic elastic constants were set to  $K_1 = 0.02$ ,  $K_4 = 0.4$  and the phonon-phason coupling constant to  $R = 0.1$ . The diffraction patterns were calculated on a square grid of size 4001x4001 pixels.



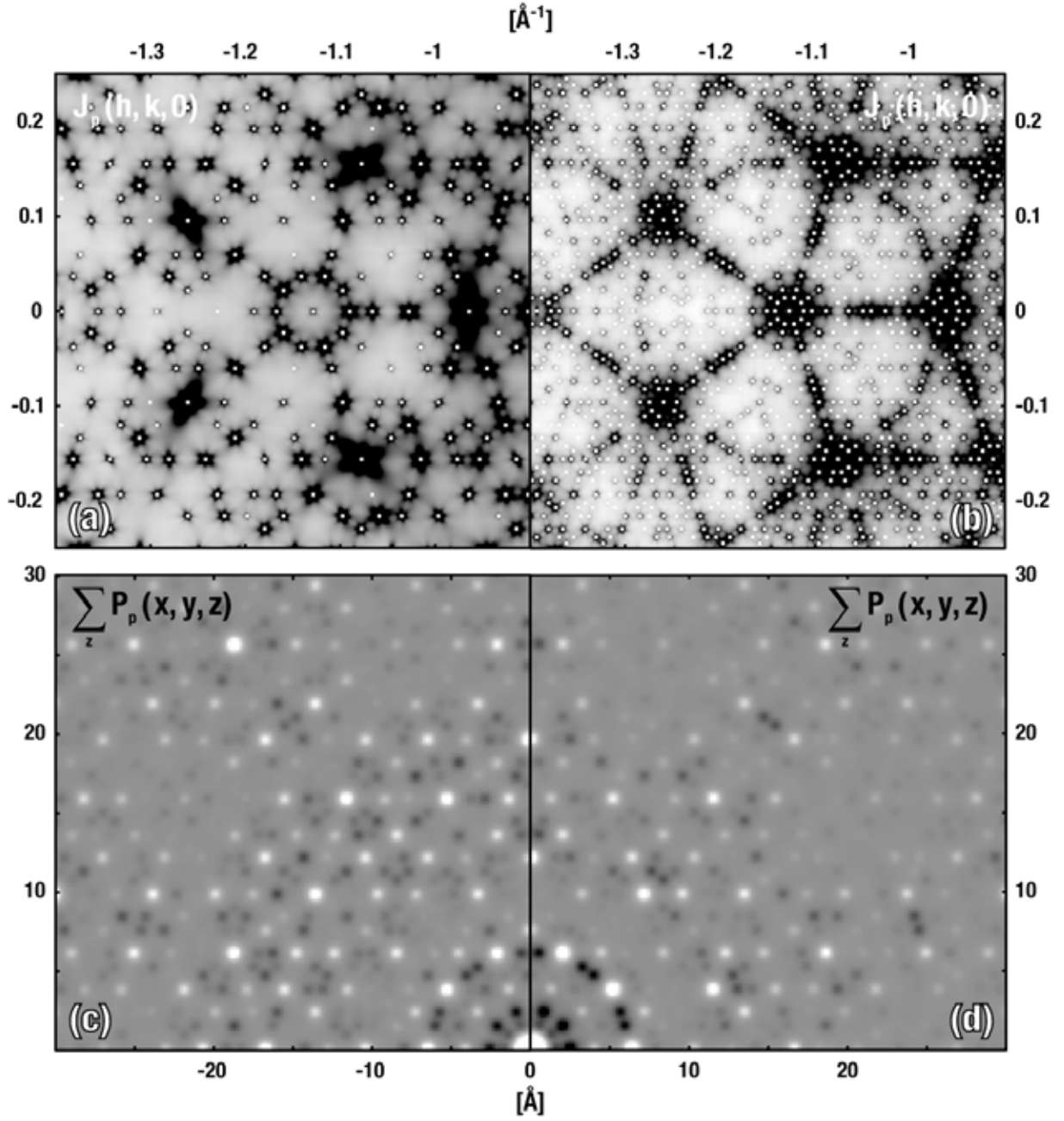


FIG. 1. Influence of a limitation of the perpendicular-space component of the diffraction vectors in reciprocal- and Patterson-space. Zoomed sections of calculated *PDS* & *TDS* of a *RPT* is shown for two datasets with a maximal perpendicular-space component of  $d_{\perp, \max}^* = 2 \text{ \AA}^{-1}$  (a) and  $d_{\perp, \max}^* = 5 \text{ \AA}^{-1}$  (b). The corresponding *PMs* are shown in (c, d), respectively. Diffuse ‘streaks’ in (b) evolve because of the superposition of *PDS* from weak Bragg reflections with high perpendicular-space components. The *PMs* of both datasets are almost equivalent for short Patterson vectors and do only differ in fine structure details. Relative scaling of the intensities in the patterns (c), (d) is 1:2.

Comparing the diffuse scattering of the two datasets [Fig. 1(a, b)], one can see a remarkable

difference. The additional Bragg reflections in Fig. 1(b) evolve a streak-like pattern of diffuse scattering and clearly change the appearance of the whole pattern. Thus, streak-like diffuse scattering of quasicrystals may result from the superposition of *PDS* from the infinite number of unobservable weak Bragg reflections with high perpendicular-space components of the diffraction vectors. Note that for Bragg reflections with high perpendicular-space components, the corresponding *PDS* intensities may be by far stronger than the sharp Bragg intensities. Taking a closer look at the *PMs* of the two datasets [Fig. 1(c, d)] one can see hardly any difference between them. In particular for short Patterson vectors, both patterns look very similar. This corroborates the assumption, that the Patterson vectors in Fig. 1(c, d) originate from *PDS* & *TDS* and are not governed by perpendicular-space truncation errors.

### C. Case studies

What is the influence of a variation of the elastic properties on the *PDS* & *TDS* calculations of a *RPT*? Five datasets with different elastic parameters are examined (see Tab. I). The number of sampling points is identical in all cases, namely 4001x4001 pixels, as well as the maximal parallel-space component of  $d_{\parallel, \max}^* = 2.5 \text{ \AA}^{-1}$  and the maximal perpendicular-space component  $d_{\perp, \max}^* = 2 \text{ \AA}^{-1}$ . The case of pure *PDS* is realized by stiffening the *RPT* in parallel-space, the case of pure *TDS* by stiffening it in perpendicular-space.

Zoomed sections of the diffraction patterns of the five cases are shown in Fig. 2(a-e). The overall distribution of diffuse scattering looks very similar in the cases (a-d) but differs from the case of pure *TDS* [Fig. 2(e)]. Usually, *TDS* is described by a function, which is zero at the origin of reciprocal-space, then increases to a maximum that is roughly proportional to the square of the diffraction vector and finally decreases slowly because of the atomic factor [for details on *TDS*, see, *e.g.*, Cowley *et al.*<sup>41</sup>]. Note, that in the present study, *TDS* is calculated from a higher-dimensional approach developed within the framework of the hydrodynamic theory<sup>4-7</sup>. Although the overall distribution of the diffuse scattering in Fig. 2(a-d) is very similar, the fine structure changes significantly.

**TABLE I. Details on elastic constants for the *PDS* & *TDS* calculations. Units are in  $10^{12}$  dyn/cm<sup>2</sup>.**

	$R > 0$	$R = 0$	$R < 0$	pure <i>PDS</i>	pure <i>TDS</i>
	Fig. 3(a, f)	Fig. 3(b, g)	Fig. 3(c, h)	Fig. 3(d, i)	Fig. 3(e, j)
$C_{11}$	2.34315	2.34315	2.34315	$1 \cdot 10^6$	2.34315
$C_{13}$	0.66625	0.66625	0.66625	$1 \cdot 10^6$	0.66625
$C_{33}$	2.32215	2.32215	2.32215	$1 \cdot 10^6$	2.32215
$C_{44}$	0.70190	0.70190	0.70190	$1 \cdot 10^6$	0.70190
$C_{66}$	0.88455	0.88455	0.88455	$1 \cdot 10^6$	0.88455
$K_1$	0.02	0.0189	0.0189	0.0189	$1 \cdot 10^6$
$K_4$	0.4	0.4	0.4	0.4	$1 \cdot 10^6$
$R$	0.1	0.0	-0.12	0.0	0.0

Taking a look at the *PMs* [Fig. 2(f-j)] one can hardly see any difference for the first four cases (f-i). This can be explained with the respective diffraction patterns. Significant differences in Fig. 2(a-d) can only be seen in the fine structure, this means in the high-frequency contributions to the diffuse scattering. Since high-frequency contributions in reciprocal-space predominantly contribute to longer vectors in Patterson-space, the striking similarity of the four *PMs* in Fig. 2(f-i) is not surprising. This has a great influence on investigations of local disorder phenomena from quasicrystals, which are due to phasonic disorder. Thus, the values for  $K_{ijkl}$  and  $R_{ijkl}$  may result quite arbitrarily from experimental studies. In contrast to the *PMs* of Fig. 2(f-i), the Patterson function of *TDS* [Fig. 2(j)] shows uniformly distributed positive Patterson peaks, each with a negative 'halo' around them. The absence of certain Patterson vectors in the *PMs* of the first four cases [see arrows in Fig. 2(f-i)] means that the structure at these vectors corresponds to the average structure and thus, these vectors are not influenced by phasonic disorder. Consequently, the *RPT* is not uniformly disordered by phasons such as it is in the case of *TDS*. Note that the integrated diffuse intensity from the pure *TDS* case is at least one order of magnitude smaller than for the other cases.

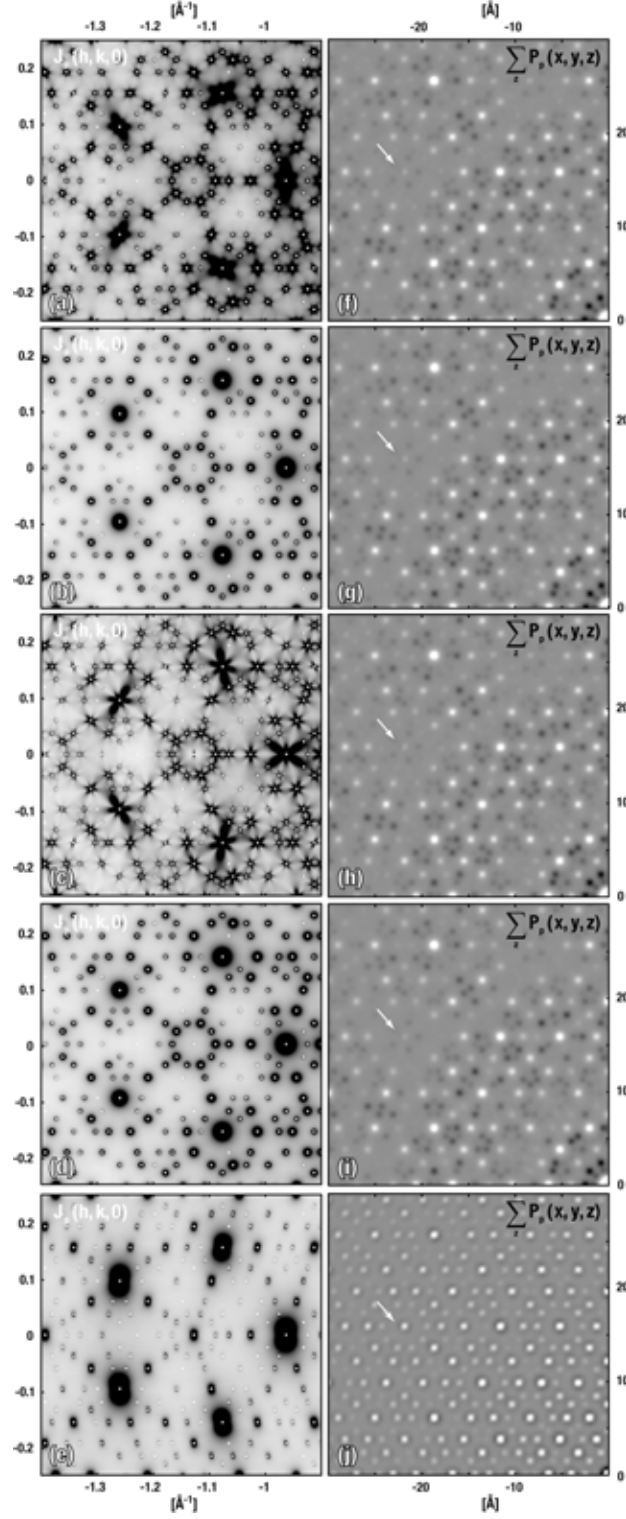


FIG. 2. Influence of a variation of the elastic parameters on the *PDS* & *TDS* calculations of a *RPT* in reciprocal- and Patterson-space (see Tab. I). Zoomed sections of the diffraction patterns of the five cases examined are shown in (a-e), the corresponding *PMs* in (f-j). The overall distribution of diffuse scattering looks very similar in the cases (a-d) but the fine structure changes significantly. Hardly any differences can be observed in the *PMs* of the first four cases (f-i). Arrows indicate absent Patterson vectors in the cases (f-i). Relative scaling of the intensities in the patterns (f-j) is 80:40:160:40:1.

## V. MODELLING *PDS* & *TDS* BASED ON EXPERIMENTAL DATA

*PDS* & *TDS* is calculated based on synchrotron diffraction data of d-Al<sub>71.5</sub>Co<sub>14.6</sub>Ni<sub>13.9</sub> (see chapter III for experimental details). The results are compared with the patterns of the *Edagawa-phase* from part A of our study. For best comparison, the data of d-Al<sub>71.5</sub>Co<sub>14.6</sub>Ni<sub>13.9</sub> has been matched in the following points to the ones from the *Edagawa-phase*. The extent in reciprocal-space is limited to  $\pm 0.8 \text{ \AA}^{-1}$ ; the *PMs* are calculated from Bragg layers  $\{hkl | -3 \leq l \leq 3\}$  and calculations are performed on a square grid of size 2137x2137 pixels. The maximal perpendicular-space component of the d-Al<sub>71.5</sub>Co<sub>14.6</sub>Ni<sub>13.9</sub> data is  $d_{\perp, \max}^* = 2.5 \text{ \AA}^{-1}$  and the elastic constants necessary for the *PDS* & *TDS* calculations are set equal to the ones in paragraph B of chapter IV. Again, all Bragg reflections stronger than 1 ppm of the intensity of the second strongest reflection are included in the calculations ( $J(\mathbf{0})$  excluded).

Fig. 3(a, d) show the *punched-and-filled* diffraction patterns at 1120 K from the *Edagawa-phase* ( $h_5 = 0$  and  $h_5 = 2$ , respectively, with index  $h_5$  referring to the  $\approx 8 \text{ \AA}$  superstructure). The original diffraction patterns are depicted in Fig. 3(b, e) and calculated *PDS* & *TDS* based on d-Al<sub>71.5</sub>Co<sub>14.6</sub>Ni<sub>13.9</sub> data in Fig. 3(c, f). Note that the *punched-and-filled* patterns [Fig. 3(a, d)] represent the extracted diffuse scattering from the original patterns [Fig. 3(b, e)] (for details on the *punch-and-fill* method, see part A of our study). The calculated *PDS* & *TDS* patterns of d-Al<sub>71.5</sub>Co<sub>14.6</sub>Ni<sub>13.9</sub> show a good agreement with the overall distribution of diffuse scattering from the *Edagawa-phase*. Differences are present in the fine structure of diffuse scattering (see zoomed sections) and in the diffuse streaks in the patterns of the *Edagawa-phase*. These deviations are partly caused by the fact that not all reflections observable on the image plate patterns (*Edagawa-phase*) have been measured by the single counter method (d-Al<sub>71.5</sub>Co<sub>14.6</sub>Ni<sub>13.9</sub>). Nevertheless, the diffuse scattering differs mostly in the fine structure, *i.e.* high-frequency part of the scattering intensity, which hardly affects short Patterson vectors.

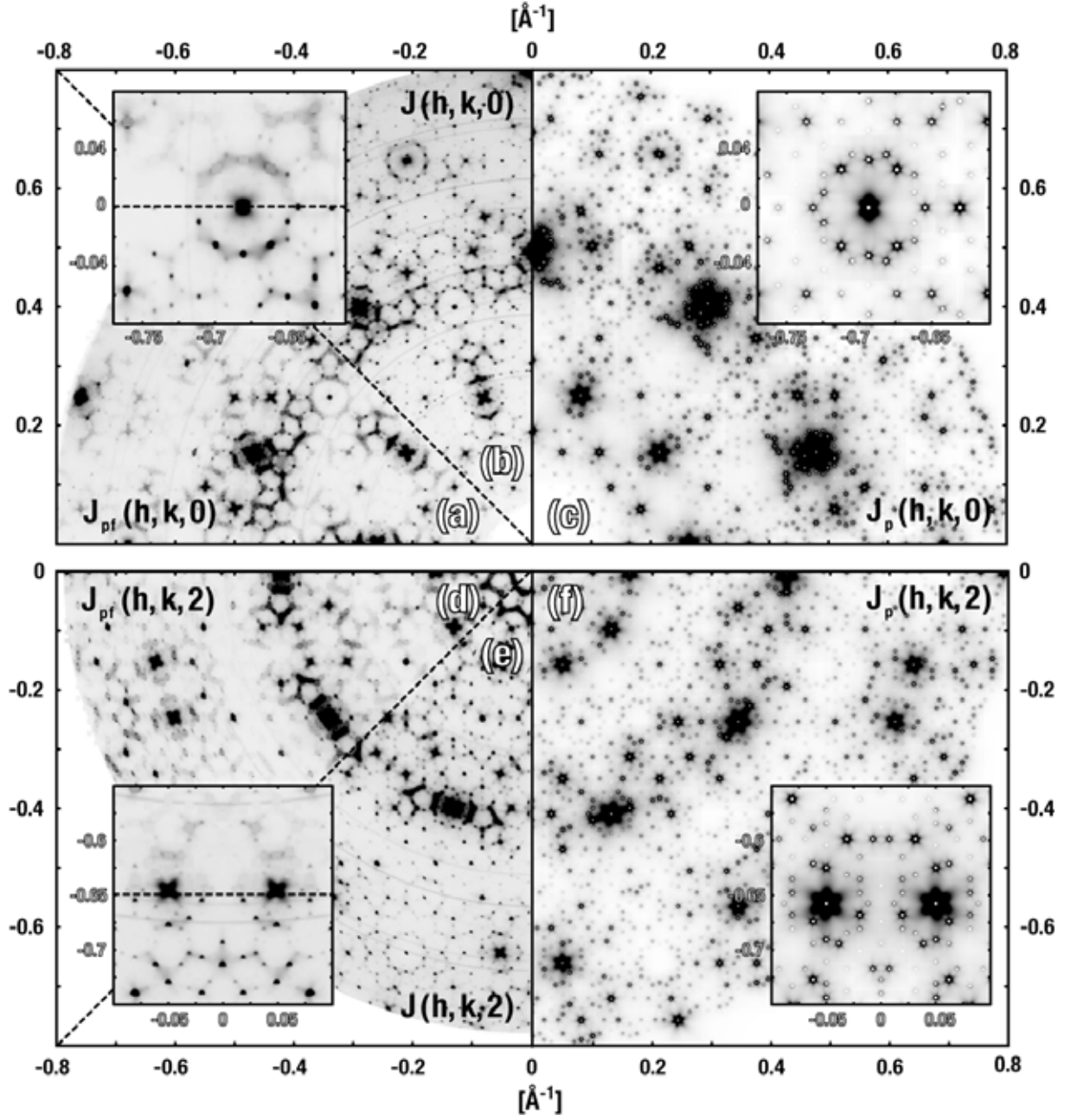


FIG. 3. Comparison of experimental and calculated diffraction patterns. (a, d) show the *punched-and-filled* diffraction patterns at 1120 K from the *Edagawa-phase*<sup>2</sup> at  $h_5 = 0$  and  $h_5 = 2$ , respectively, (b, e) the original diffraction patterns and (c, f) calculated *PDS & TDS* of the d-Al<sub>71.5</sub>Co<sub>14.6</sub>Ni<sub>13.9</sub> dataset. Zoomed sections in the insets show differences between the experimental and calculated patterns. The index  $h_5$  refers to the  $\approx 8\text{\AA}$  superstructure.

Figure 4(a, c, e) shows the projected *PM* as well as the *PMs* at  $z = 0$  and  $z = 0.25$  of the *punched-and-filled* distribution of diffuse scattering from the *Edagawa-phase* at 1120 K. The *PMs* of calculated *PDS* & *TDS* of the  $\text{d-Al}_{71.5}\text{Co}_{14.6}\text{Ni}_{13.9}$  dataset are depicted in Fig. 4(b, d, f), respectively. The correspondence between experiment and simulation is excellent. Consequently, structural disorder of the *Edagawa-phase* for correlation lengths up to 60 Å can be described by phasonic disorder. The results do equally well apply to the datasets collected at 300 K and 1070 K but with the difference that the correlation lengths in these patterns are smaller (see part *A* of our study). Note that the accessible region in the *PMs* of the *Edagawa-phase* extends to about 60 Å (see part *A* of our study). Beyond this limit, information on the difference structure is no more accessible by our dataset and the *punch-and-fill* method. Noticeable differences between experiment and simulation can only be observed in the *PMs* at  $z = 0.25$ . There, the *punched-and-filled PM* of the *Edagawa-phase* shows additional positive Patterson peaks with regard to the *PM* of *PDS* & *TDS* [see arrows in Fig. 4(e, f)]. These peaks may be due to disorder phenomena of the *Edagawa-phase*, which are not described by phasonic disorder or due to some structural differences between  $\text{d-Al}_{71.5}\text{Co}_{14.6}\text{Ni}_{13.9}$  (single counter data) and  $\text{d-Al}_{70}\text{Co}_{12}\text{Ni}_{18}$  (image plate data).

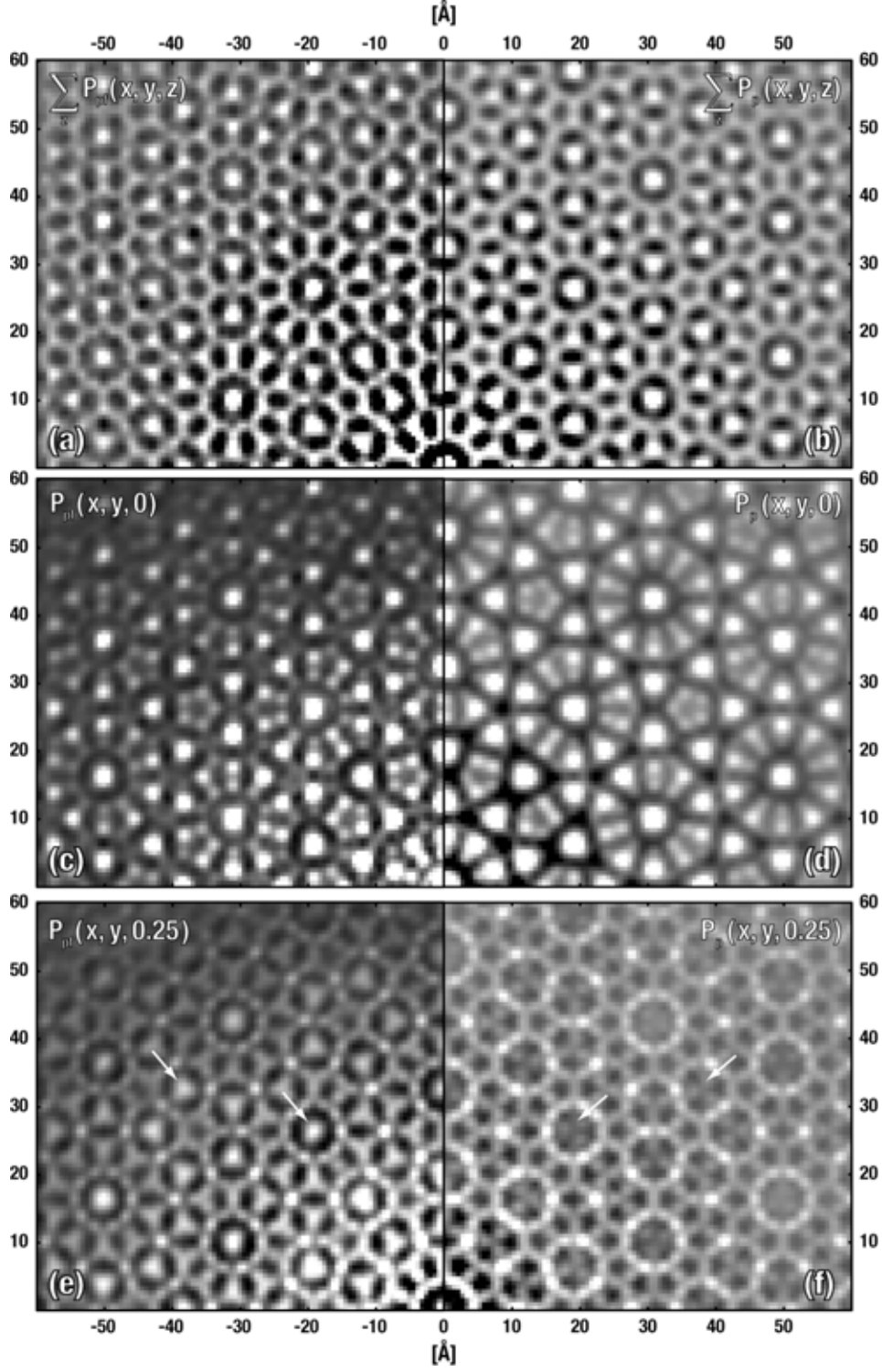


FIG. 4. Projected PM (a), the PMs at  $z = 0$  (c) and  $z = 0.25$  (e) of the *punched-and-filled* distribution of diffuse scattering from the *Edagawa-phase* at 1120 K in comparison with the Patterson function of calculated PDS & TDS of the d-Al<sub>71.5</sub>Co<sub>14.6</sub>Ni<sub>13.9</sub> dataset (b, d, f), respectively. The *punched-and-filled* PM of the *Edagawa-phase* shows additional positive Patterson peaks with regard to the PM of PDS & TDS (see arrows in (e, f)). Relative scaling of the intensities in the patterns (a), (c), (e) is 1:10:10 and in (b), (d), (f) it is 1:5:10.



## VI. MODELLING DISORDER ON THE SCALE OF CLUSTERS

In the following calculations of structural disorder phenomena, a Patterson function approach is used, in which correlations *between* structural building units (*e.g.* clusters) are ignored. As a consequence, inter-cluster Patterson vectors from the disordered structure are the same as the corresponding inter-cluster Patterson vectors from the average structure. Thus, the Patterson function from the difference structure only shows intra-cluster Patterson vectors. Consequently, the structural model can be limited to the size of a single columnar cluster. This approach is described in more detail by Cowley<sup>40</sup>.

Given a number  $m$  of different cluster configurations, the diffuse intensity may then be written in the form

$$I_{diffuse}(\mathbf{r}^*) = \frac{1}{m} \sum_{i=1}^m |F_i(\mathbf{r}^*) - F_{aver}(\mathbf{r}^*)|^2, \quad (2)$$

as long as the probabilities for each cluster configuration  $m$  is the same.  $F_i(\mathbf{r}^*)$  are the Fourier transforms of  $\rho_i(\mathbf{r})$ , which represent the electron density distributions of the different cluster configurations. In all following calculations of local disorder phenomena, the diffuse scattering resulting from a specific disorder phenomenon has been calculated according to Eq. 2. Note that since no inter-cluster correlations are included in the approach, the *PMs* calculated therefrom do not show Patterson vectors longer than the diameter of a single columnar cluster!

Various kinds of disorder phenomena of about 20-32 Å-sized clusters have been simulated with the goal to identify local disorder phenomena of clusters and their sub-units. We have investigated the following models of disorder: substitutional disorder between TM and Al, occupational disorder of Al, displacive disorder of whole clusters along the periodic axis with displacements of 2 Å and 4 Å, different local environments around Co and Ni, orientational disorder of clusters or sub-units therein, size-effect like distortions between Co and Ni and also combinations of these disorder phenomena. The simulations have been performed on the most reasonable cluster models reported in literature (see paragraph B of chapter II). Due to

the lack of cluster-models for the *Edagawa-phase* (four-layer structure), we predominantly used two-layer structure models to model disorder phenomena, which describe the diffuse intensities inside the Bragg layers of the *Edagawa-phase*. Thus, the two-layer cluster must result from the projection of the four-layer structure with sequence  $A, B, A', B'$  onto a two-layer structure with sequence  $(A+A'), (B+B')$ . This projection allows the use of two-layer cluster-models, which are chemically not reasonable, *e.g.* have too short atomic distances or atomic sites with mixed occupancy in contrast to the underlying four-layer model.

Best results are obtained with the cluster-model of Abe<sup>20</sup>. It shows mirror symmetry and a pseudo  $10_5$ -screw axis along the periodic axis (rotation of  $180^\circ$  and translation of  $\approx 2 \text{ \AA}$ ). Latter symmetry operator is fulfilled by a bigger part of the cluster, although disagreement is present in the central part of the cluster and the P sub-clusters<sup>26</sup>, which are sub-units of the Abe-cluster.

Best agreement between the experimental diffraction patterns of the *Edagawa-phase* from part A and calculated diffuse scattering is obtained for a fivefold orientationally disordered Abe-cluster<sup>20</sup>. For best comparison, the data of the present calculations have been matched to the ones from the *Edagawa-phase*, as described in chapter V. Fig. 5(a, d) shows the *punched-and-filled* diffraction patterns at 300 K of the *Edagawa-phase* ( $h_5 = 0$  and  $h_5 = 2$ , respectively). The original diffraction patterns are depicted in Fig. 5(b, e) and calculated diffuse scattering from fivefold orientational disorder of the Abe-cluster is shown in Fig. 5(c, f). The calculated diffuse scattering is in good agreement with the overall distribution of diffuse scattering from the *Edagawa-phase*, both at  $h_5 = 0$  and  $h_5 = 2$ . Note, that the size of the cluster ( $\approx 20 \text{ \AA}$  in diameter) limits the smallest width of a calculated diffuse feature to about  $0.05 \text{ \AA}^{-1}$ . The application of fivefold orientational disorder on clusters with  $5m$  symmetry, like the clusters proposed by Hiraga<sup>21-23</sup> and Ritsch<sup>24,25</sup>, does not produce any diffuse scattering at all.

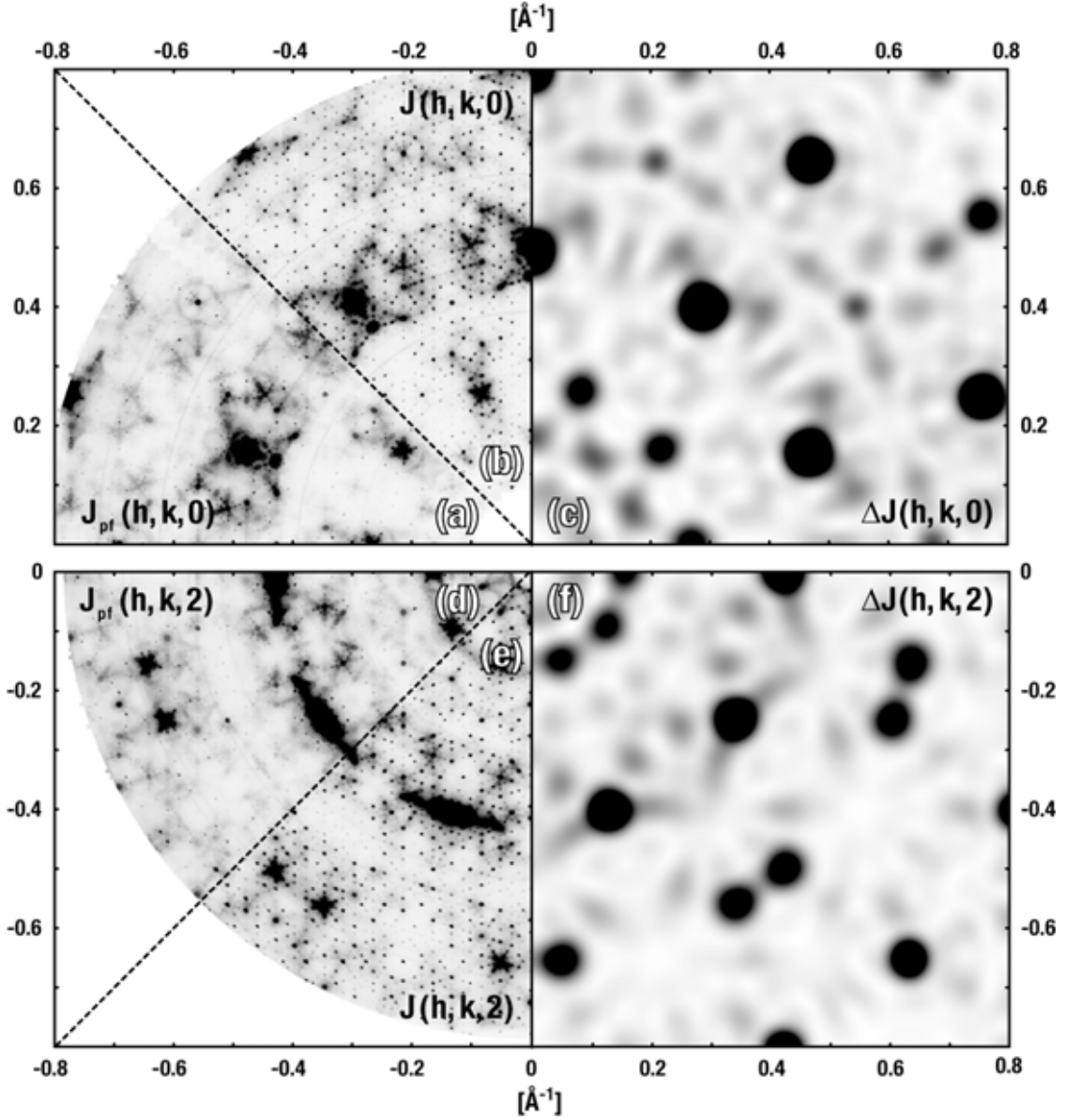


FIG. 5. Comparison of experimental and calculated diffraction patterns. (a, d) show the *punched-and-filled* diffraction patterns at 300 K from the *Edagawa-phase* at  $h_5 = 0$  and  $h_5 = 2$ , respectively, (b, e) the original diffraction patterns and (c, f) calculated diffuse scattering from fivefold orientational disorder of the Abe-cluster. Note that the size of the cluster ( $\approx 20$  Å in diameter) limits the smallest width of a calculated diffuse feature to about  $0.05$  Å $^{-1}$ .

Figure 6(a, c, e) shows the projected *PM* as well as the *PMs* at  $z = 0$  and  $z = 0.25$  of the *punched-and-filled* distribution of diffuse scattering from the *Edagawa-phase* at 300 K. The Patterson function of calculated diffuse scattering from the fivefold orientationally disordered Abe-cluster is depicted in Fig. 6(b, d, f). The correspondence between experiment and simulation is very good, although minor differences can be spotted in the *PMs*. These results

do equally well apply to the datasets collected at 1070 K and 1120 K of the *Edagawa-phase*. As described in the previous paragraph, the Patterson function of calculated diffuse scattering does only extend up to Patterson vectors close to 20 Å (diameter of a cluster). Note that the *PMs* (up to  $\approx 20$  Å) of diffuse scattering from the *Edagawa-phase* are almost equally well described by *PDS* or fivefold orientational disorder of the Abe-cluster [compare Fig. 4, 6]. This is a strong indication that fivefold orientational disorder of clusters is the short-range 3D structural representation of 5D phasonic disorder. Orientational disorder of clusters can be induced by phasons as will be shown in an upcoming section.

Fivefold orientational disorder of the Abe-cluster produces several local disorder phenomena, which are illustrated in Fig. 7. These are flips of Al-atoms on a scale of  $\approx 1$  Å (label 1), substitutional disorder between TM and Al (label 2), occupational disorder of TM or Al (label 3, 4) and split-positions between TM and Al (label 5). The pentagons in the centre of layer *A* (label 6) and *B* (label 7) differ in orientation by  $36^\circ$  and have a different chemical composition. The pentagon in layer *A* contains only TM atoms, whereas the pentagon in layer *B* is composed both of TM and Al. The former pentagon would give only little contrast variation in high-resolution transmission electron microscopy (HRTEM) images whereby the latter would show pseudo-fivefold symmetry. Fivefold orientational disorder of the Abe-cluster has also some remarkable consequences on the symmetry of the cluster. Not only does the symmetry of the average cluster increase from  $m$  to  $5m$ , but also the pseudo  $10_5$ -screw axis turns almost into a real  $10_5$ -screw axis. These observations are partly in accordance with the findings of Hiraga<sup>23</sup>, who described the average cluster of the Ni-rich basic phase by a  $\approx 32$  Å cluster having  $5m$  symmetry and a  $10_5$ -screw axis along the periodic direction.

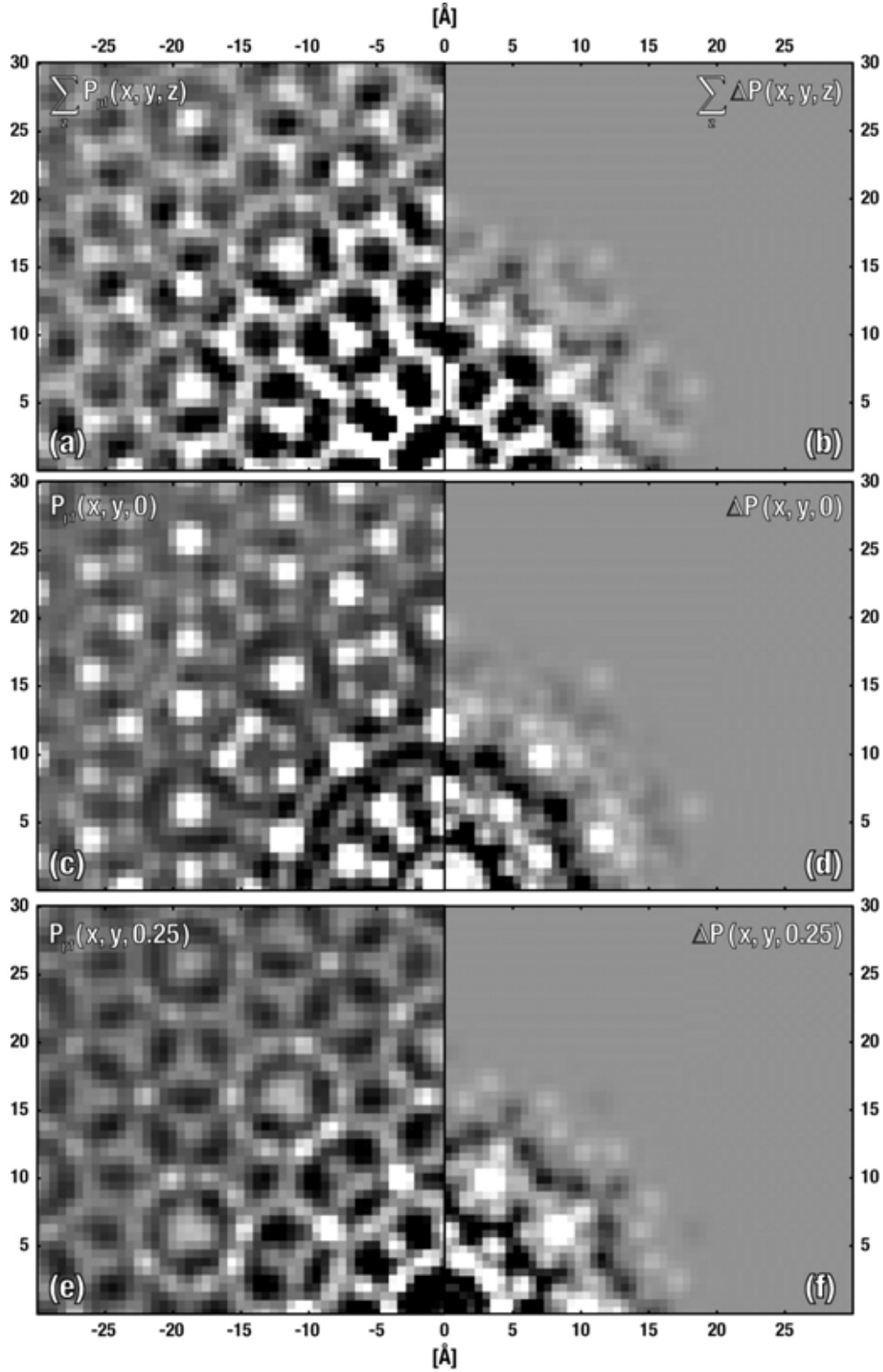


FIG. 6. Projected *PM* (a), the *PMs* at  $z = 0$  (c) and  $z = 0.25$  (e) of the *punched-and-filled* distribution of diffuse scattering from the *Edagawa-phase* at 300 K in comparison with the Patterson function of calculated diffuse scattering from the fivefold orientationally disordered Abe-cluster (b, d, f), respectively. Relative scaling of the intensities in the patterns (a), (c), (e) is 1:10:10 and in (b), (d), (f) it is 1:3:3.

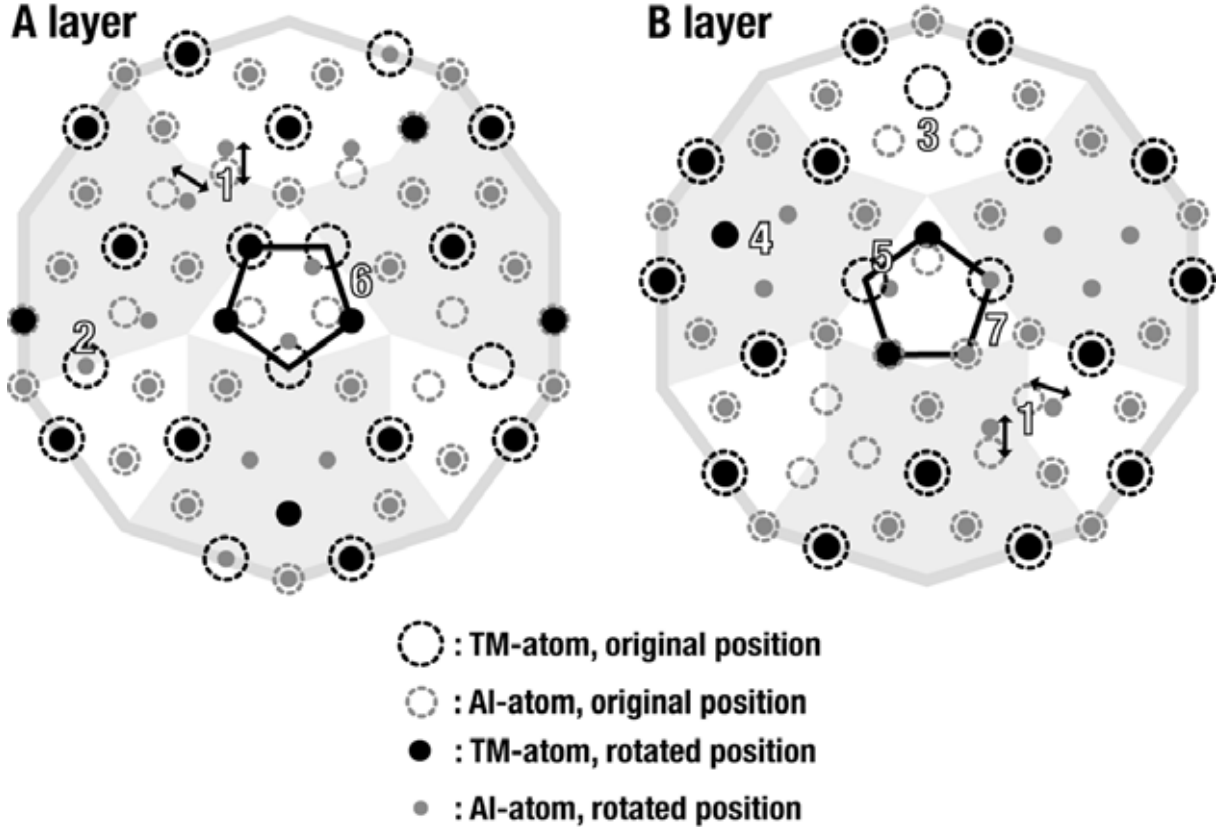


FIG. 7. Local disorder phenomena induced in the Abe-cluster by a rotation of  $72^\circ$ . The left part shows the effects on the *A* layer, the right part on the *B* layer. Observable local disorder phenomena are flips of Al-atoms (label 1), substitutional disorder between TM and Al (label 2), occupational disorder of TM or Al (label 3, 4) and split-positions between TM and Al (label 5). The pentagons in the centre of layer *A* (label 6) and *B* (label 7) differ in orientation by  $36^\circ$  and have a different chemical composition.

## VII. DISCUSSION

### A. Cluster symmetry

*EM* studies on decagonal Al-Co-Ni quasicrystals significantly differ in the symmetry of the fundamental columnar clusters derived from them. Cluster models having mirror symmetry compete against cluster models showing  $5m$  symmetry. Possibly, fivefold orientational disorder plays an important role in the appearance of symmetry on HRTEM or high-angle annular dark-field scanning transmission electron microscopy (HAADF-STEM) images. HRTEM and HAADF-STEM are techniques, in which time and space averaging takes place

over different scales. If we assume that the real cluster possesses mirror symmetry, then the average structure of the fivefold orientationally disordered cluster would have  $5m$  symmetry. How this could look like is illustrated schematically in Fig. 8, which shows a superposition of the Hiraga-cluster<sup>23</sup> and the average structure of the fivefold orientationally disordered Abe-cluster<sup>20</sup>. Both models are used to describe the structure of the Ni-rich basic phase. The agreement between the two models is remarkable. Almost all atomic sites of the Hiraga-cluster coincide with the atomic sites of the averaged Abe-cluster. Nevertheless, minor differences between both models can be found. The averaged Abe-cluster shows mixed TM/Al occupancy, while the Hiraga-cluster contains either TM [Fig. 8, label 1] or Al (label 2). Furthermore, the averaged Abe-cluster shows Al split positions (label 3) and split positions between mixed atomic sites and Al (label 4). Note that the averaged Abe-cluster shows a  $10_5$ -screw axis, while the not averaged cluster possesses a pseudo  $10_5$ -screw axis only.

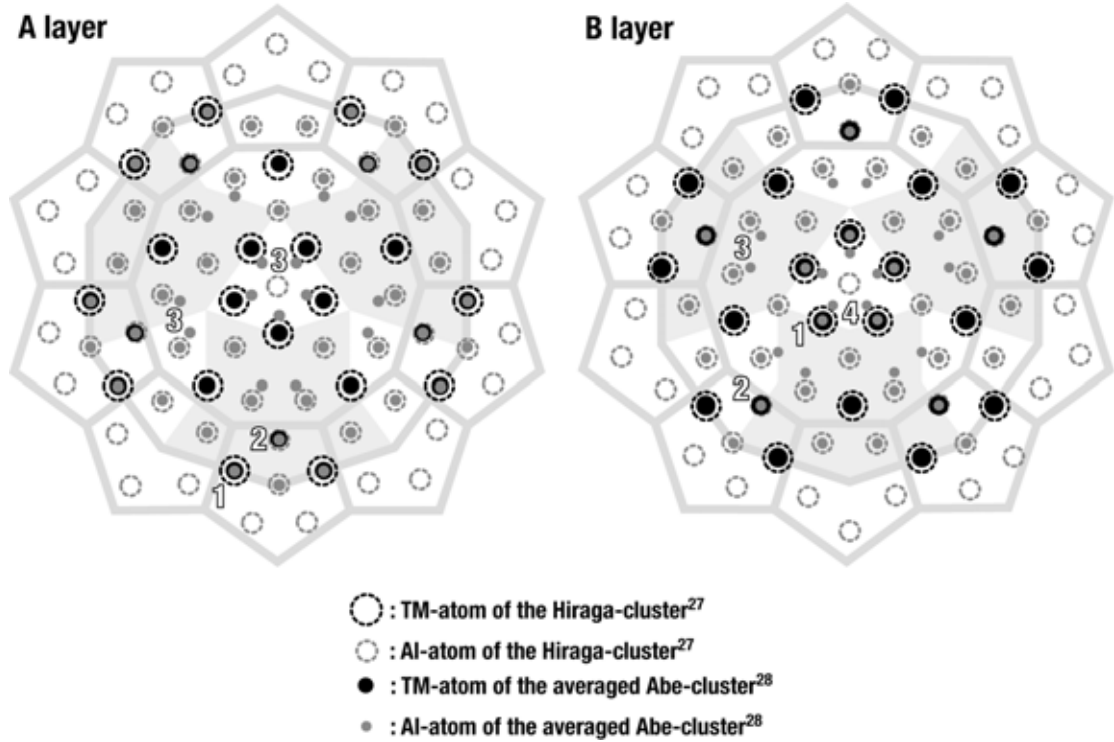


FIG. 8. A superposition of the Hiraga-cluster<sup>23</sup> and the average structure of the fivefold orientationally disordered Abe-cluster<sup>20</sup>. The Hiraga-cluster has  $5m$  symmetry, while the original Abe-cluster shows mirror symmetry only. Almost all atomic sites of the Hiraga-cluster coincide with the atomic sites of the averaged Abe-cluster. The averaged Abe-cluster shows mixed TM/Al occupancy, while the Hiraga-cluster contains either TM (label 1) or Al (label 2). Furthermore, the averaged Abe-cluster shows Al split positions (label 3) and split positions between mixed atomic sites and Al (label 4).

## B. 3D structural representation of PDS

How can *PDS*, which is well defined in five-dimensional space, be described in three dimensions? This question is a central topic in diffuse scattering studies of quasicrystals, which has not yet been satisfactorily answered. We show that *PDS* produces local disorder phenomena, which can equivalently be described by fivefold orientational disorder of clusters (up to the diameter of a columnar cluster). Model calculations using only main reflections from the complete d-Al<sub>71.5</sub>Co<sub>14.6</sub>Ni<sub>13.9</sub> dataset (extent in reciprocal-space up to  $\pm 1.5 \text{ \AA}^{-1}$ , the *PMs* are calculated from Bragg layers  $\{hkl \mid -6 \leq l \leq 6\}$ ) are compared with results from fivefold orientational disorder of the Abe-cluster<sup>20</sup> (same constraints as above). The large extent in reciprocal-space results in an atomic resolution ( $\approx 1 \text{ \AA}$ ) of the difference *PMs*. This corresponds almost to the doubled resolution ( $\approx 2 \text{ \AA}$ ) of the *PMs* depicted in Fig. 4, 6. All calculations have been performed on a square grid of size 2401x2401 pixels and the elastic constants for the *PDS* & *TDS* calculations are equal to the ones described in paragraph B of chapter IV.

Figure 9(a, c, e) shows the projected *PM* as well as the *PMs* at  $z = 0$  and  $z = 0.25$  of the average structure of d-Al<sub>71.5</sub>Co<sub>14.6</sub>Ni<sub>13.9</sub>. The Patterson function of the average structure of the fivefold orientationally disordered Abe-cluster is depicted in Fig. 9(b, d, f), respectively. The *PMs* of the average structure of d-Al<sub>71.5</sub>Co<sub>14.6</sub>Ni<sub>13.9</sub> have been calculated by Fourier transformation of the corresponding reciprocal layers, which have been generated by convoluting the Bragg reflections with two-dimensional Gaussian functions. This procedure is necessary, since the Bragg patterns, which consist of  $\delta$ -functions with Laue symmetry  $10/mmm$ , cannot otherwise be mapped on a quadratic grid. The agreement between the patterns is excellent indicating that the local average structure of d-Al<sub>71.5</sub>Co<sub>14.6</sub>Ni<sub>13.9</sub> corresponds to the average structure of the fivefold orientationally disordered Abe-cluster. Note that the Abe-cluster has been derived from *EM* investigations, from which one only obtains the projected structure. Thus, information like the patterns in Fig. 9(c-f) are not directly accessible by *EM* investigations. Good agreement with the *PMs* of the average structure of d-Al<sub>71.5</sub>Co<sub>14.6</sub>Ni<sub>13.9</sub> has also been obtained by computing the average structures of fivefold orientationally disordered clusters of Abe<sup>19</sup>, Steinhardt<sup>27-28</sup>, Yan<sup>31-34</sup> and Hiraga<sup>23</sup>. Nevertheless, a better agreement was obtained with the cluster of Abe<sup>20</sup>.



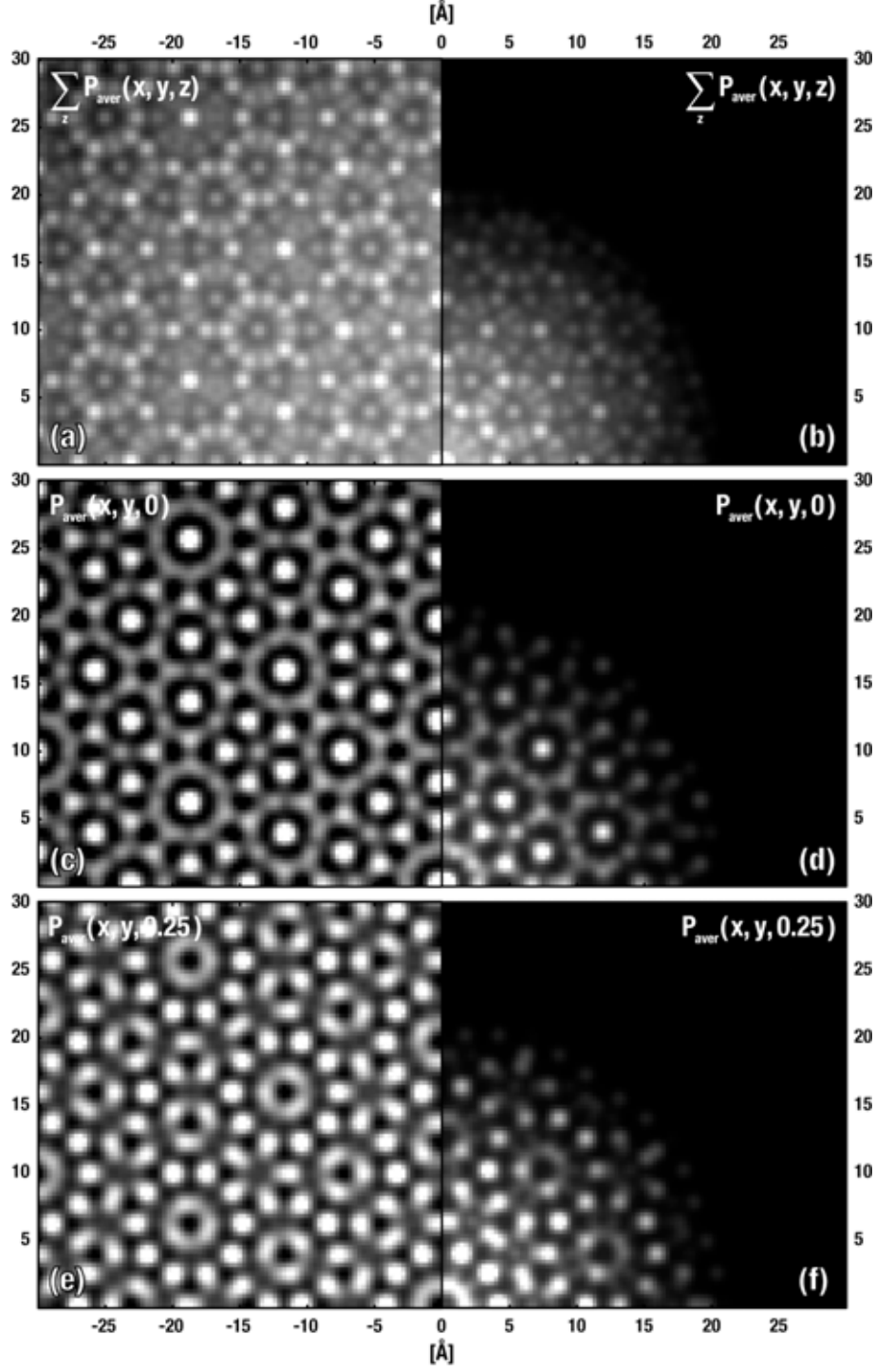


FIG. 9. Projected  $PM$  (a), the  $PM$ s at  $z = 0$  (c) and  $z = 0.25$  (e) of the average structure of the d-Al<sub>71.5</sub>Co<sub>14.6</sub>Ni<sub>13.9</sub> dataset calculated from main reflections in comparison with the Patterson function of the average structure of the fivefold orientationally disordered Abe-cluster (b, d, f), respectively. The local average structure of d-Al<sub>71.5</sub>Co<sub>14.6</sub>Ni<sub>13.9</sub> corresponds to the average structure of the fivefold orientationally disordered Abe-cluster. Relative scaling of the intensities in the patterns in (a), (c), (e) is 1:2:2 and in (b), (d), (f) it is 1:4:3.

Figure. 10(a, c, e) shows the projected *PM* as well as the *PMs* at  $z=0$  and  $z=0.25$  of calculated *PDS* & *TDS* from the d-Al<sub>71.5</sub>Co<sub>14.6</sub>Ni<sub>13.9</sub> dataset. They are compared with the *PMs* of diffuse scattering resulting from the fivefold orientationally disordered Abe-cluster (b, d, f), respectively. Excellent agreement between the two models of disorder is obtained. The difference structure of the fivefold orientationally disordered Abe-cluster clearly corresponds to the local difference structure of the 3D description of phasonic disorder of d-Al<sub>71.5</sub>Co<sub>14.6</sub>Ni<sub>13.9</sub>. Concerning the clusters of Abe<sup>19</sup>, Steinhardt<sup>27-28</sup> and Yan<sup>31-34</sup>, the agreement of the difference *PMs* is less distinct than for the cluster of Abe<sup>20</sup>, but still good. The cluster of Hiraga<sup>23</sup> does not show any diffuse scattering caused by a fivefold orientational disorder, because of its symmetry. These observations indicate that *PDS* in decagonal quasicrystals can generally be described as fivefold orientational disorder of clusters. In the present study, this has been shown for decagonal quasicrystals, the quasiperiodic patterns of which may be described by a *RPT* and the clusters of which are mirror symmetric. Nothing can be said for other types of quasicrystals.

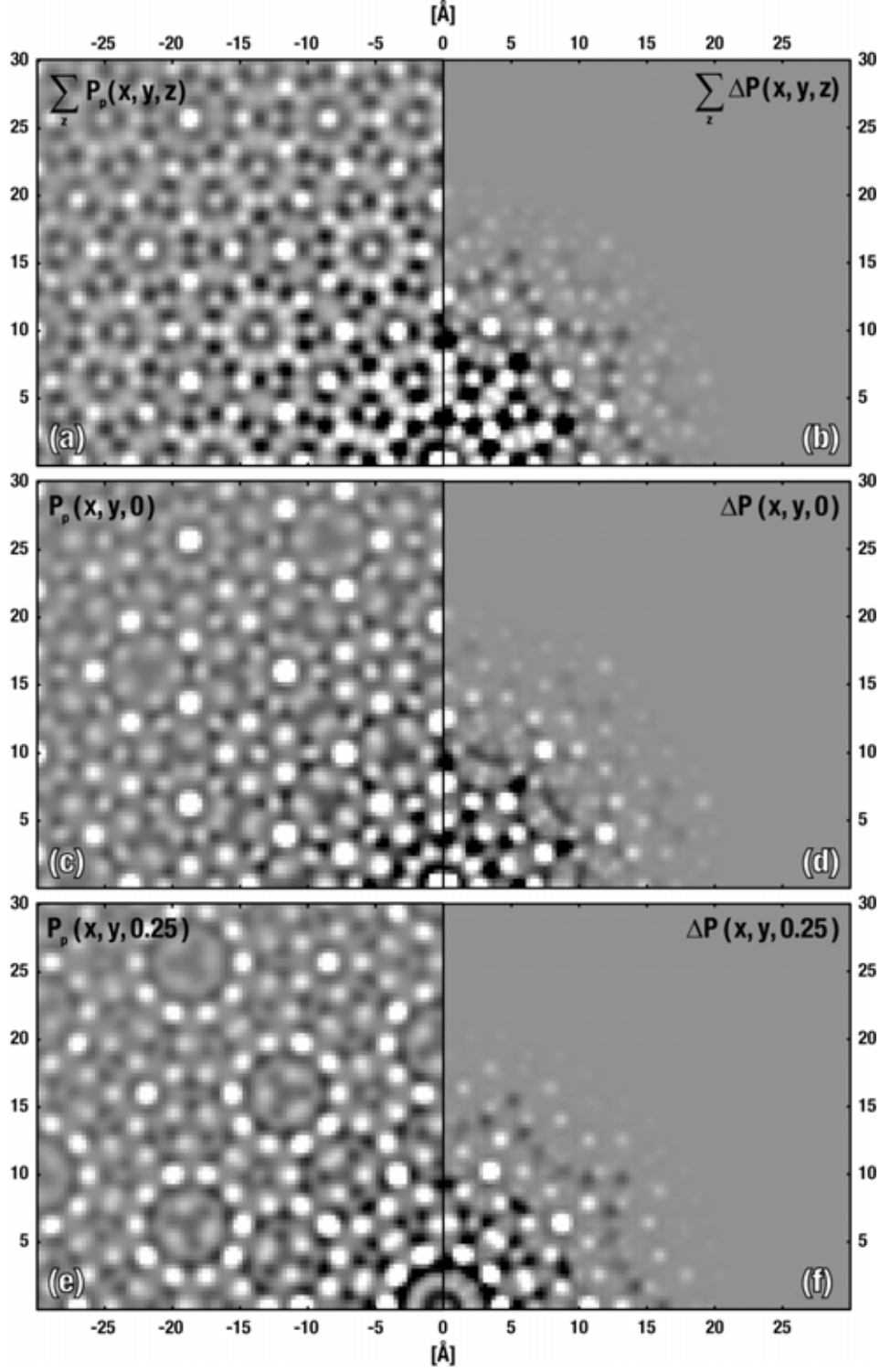


FIG. 10. Projected *PM* (a), the *PMs* at  $z = 0$  (c) and  $z = 0.25$  (e) of calculated *PDS* & *TDS* of the d-Al<sub>71.5</sub>Co<sub>14.6</sub>Ni<sub>13.9</sub> dataset calculated from main reflections in comparison with the Patterson function of calculated diffuse scattering from the fivefold orientationally disordered Abe-cluster (b, d, f), respectively. The difference structure of the fivefold orientationally disordered Abe-cluster corresponds to the local difference structure of phason disordered d-Al<sub>71.5</sub>Co<sub>14.6</sub>Ni<sub>13.9</sub>. Relative scaling of the intensities in the patterns (a), (c), (e) is 1:3:3 and in (b), (d), (f) it is 1:5:6.

### C. Average structure modifications induced by phasonic fluctuations

What kind of influence do phasons and phonons have on the higher-dimensional description of quasicrystals? Phonons in normal crystals smear out the probability density of atoms in the average structure. In quasicrystals their influence is similar, but here phonons broaden the  $ASs$  only in parallel-space, which leads to displacive disorder in the cut-space. By cut-space we mean the atomic configurations in parallel-space, which are obtained through a cut of the higher-dimensional embedding-space by the parallel-space. Phasons are responsible for the broadening of the  $ASs$  in perpendicular-space, which causes substitutional disorder and split positions in the cut-space. The phonon-phason coupling term couples phasonic and phononic fluctuations of the  $ASs$ . Consequently, in the case of a strong coupling term, phononic fluctuations induce phasonic disorder and *vice versa*. An interesting question concerns the modifications that the average structure in the cut-space undergoes if phasonic fluctuations of the  $ASs$  are introduced.

To answer this question we have constructed  $RPTs$  (as described in chapter IV) with slightly different radii of the  $ASs$ . The radii of the six considered cases are the following:

$\{(0.36 + i \cdot 0.04) \cdot \frac{a}{\tau^2} \mid i = 0, 1, 2, 3, 4, 5\}$  and  $\{(0.36 + i \cdot 0.04) \cdot \frac{a}{\tau} \mid i = 0, 1, 2, 3, 4, 5\}$  for the  $ASs$  at  $p = 1, 4$  and at  $p = 2, 3$ , respectively. An  $RPT$  in the standard embedding has  $ASs$  with radii  $0.4 \cdot \frac{a}{\tau^2}$  and  $0.4 \cdot \frac{a}{\tau}$ , respectively. The cut-spaces of the six cases are shown in Fig.

11(a-f), respectively. The average structure of the highlighted cluster changes significantly with increasing radii of the  $ASs$ , *i.e.* increasing amount of phasonic disorder. Note that the considered datasets are cutouts of  $5D$  infinite lattices. This fact leads to perpendicular-space truncation errors, which give rise to additional atomic positions in the cut-spaces of (a-f). The structure in (a) is well described by a hexagon-boat-star tiling ( $HBS$ ), while the structure in (b) follows an idealized tie-and-navette tiling. Closer inspection of the highlighted cluster in (c) reveals an ordering, which can be described by a fivefold orientational disorder of the cluster from (a). Further increase of the  $ASs$  leads to an increasing number of clusters, which are best described by fivefold orientational disorder (d-f). Thus, the formation of average clusters, which correspond to fivefold orientationally disordered clusters, naturally evolves by

introducing phasonic fluctuations of the *ASs*, *i.e.* phasons induce orientational disorder of clusters.

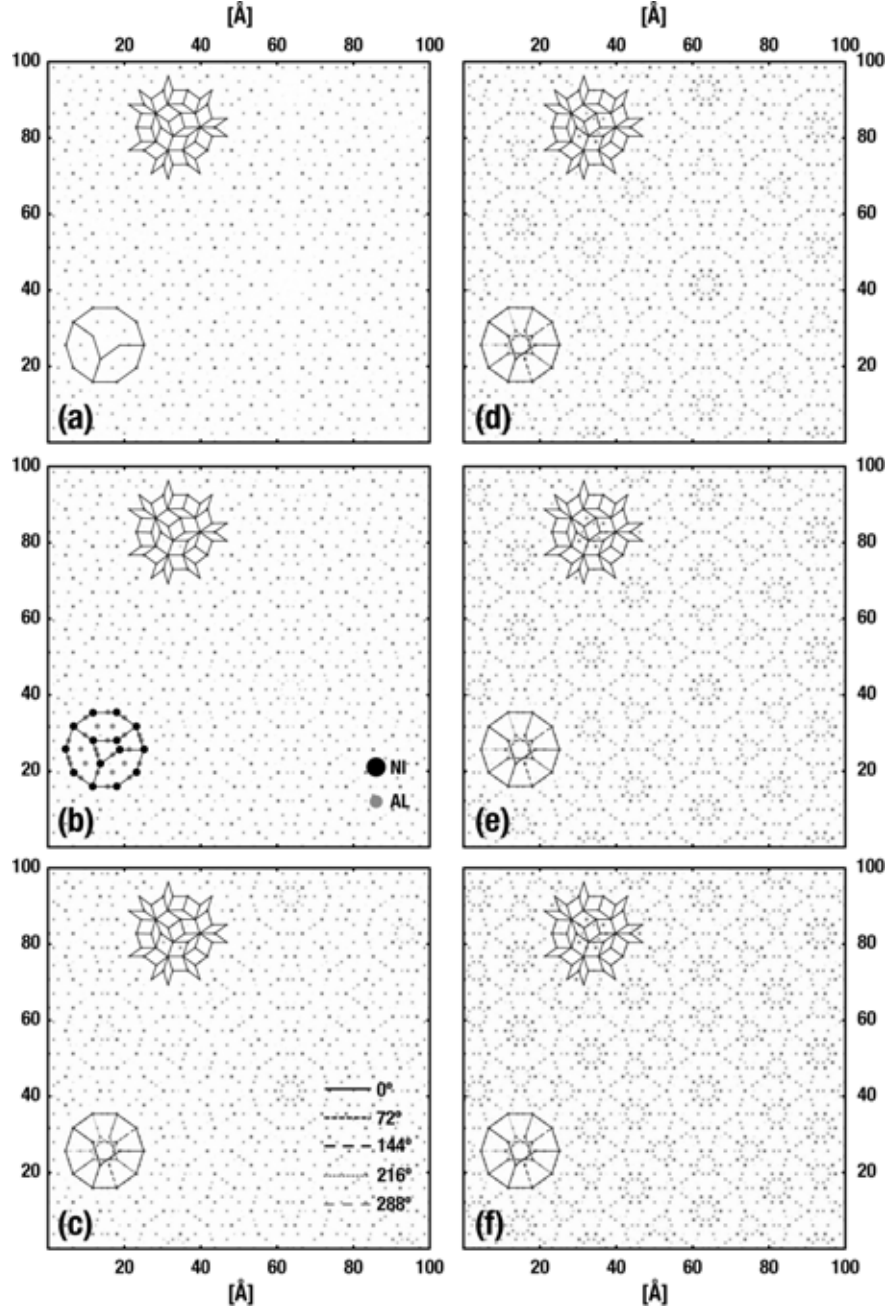


**FIG. 11.** Influence of phasonic fluctuations of the *ASs* of a *RPT* on the atomic configurations in parallel-space (modelled by radii fluctuations of the *ASs*). The average structures with increasing radii are shown in (a-f), respectively. The structure in (a) is well described by a hexagon-boat-star tiling, while the structure in (b) follows an idealized tie-and-navette tiling. The structure in (c) can be described by fivefold orientational disorder of the cluster from (a). Further increase of the *ASs* leads to an increasing number of clusters, which are best described by a fivefold orientationally disordered clusters (d-f). A small section of the underlying *RPT* is depicted in (a-f).

#### D. Structural disorder of the quasiperiodic superstructure

The structure of the quasiperiodic superstructure of the *Edagawa-phase* is still an unsolved question. Several models based on *EM* studies have been proposed. They have some kind of ordering between the fundamental columnar clusters in common.<sup>42,43</sup> None of the studies published so far deal with the structural disorder associated with the superstructure ordering. Our calculations of *PDS* & *TDS* based on the d-Al<sub>71.5</sub>Co<sub>14.6</sub>Ni<sub>13.9</sub> dataset (including main and satellite reflections) in chapter V have shown a good agreement with the *PMs* of the *Edagawa-phase*. On the basis of these calculations we studied the structural disorder associated with the superstructure ordering only.

*PDS* & *TDS* is calculated based on S1 and S2 satellite reflections of the complete d-Al<sub>71.5</sub>Co<sub>14.6</sub>Ni<sub>13.9</sub> dataset (extent in reciprocal-space up to  $\pm 1.5 \text{ \AA}^{-1}$ , the *PMs* are calculated from Bragg layers  $\{hkl \mid -6 \leq l \leq 6\}$ ). All calculations have been performed on a square grid of size 2401x2401 pixels with elastic constants for the *PDS* & *TDS* calculations equal to the ones in paragraph B of chapter IV. Figure 12(a, c, e) shows the projected *PM* as well as the *PMs* at  $z=0$  and  $z=0.25$  of *PDS* & *TDS* calculated only from S1 reflections of the d-Al<sub>71.5</sub>Co<sub>14.6</sub>Ni<sub>13.9</sub> dataset. They are compared with the difference *PMs* calculated from the S2 reflections only (b, d, f), respectively. The *PMs* show a correspondence between maxima in one pattern and minima in the other pattern (see arrows in Fig. 12(a-d)). As described in part A, these strong Patterson peaks may be related to translation vectors, which correspond to inter-cluster vectors between centers of the *Gummelt* decagons in the corresponding quasiperiodic covering. The fine structure around these Patterson peaks is due to inter-cluster correlations. The projected *PM* of the S2 reflections is strongly structured, indicating the presence of both intra- and inter-cluster correlations, whereas the pattern of the S1 reflections mainly shows inter-cluster correlations. The correlations inside quasiperiodic planes of S1 and S2 reflections show similar correlation lengths of the underlying disorder phenomena [Fig. 12(c, d)]. However, the correlations between adjacent quasiperiodic layers [Fig. 12(e, f)] show a remarkable difference in the pattern of the S1 and S2 reflections. The *PM* at  $z=0.25$  calculated from S1 reflections does hardly show any correlations in contrast to the pattern of the S2 reflections. The latter shows a strongly structured pattern both at small and long Patterson vectors. Note that the S1 and S2 reflections of the *Edagawa-phase* exhibit a different temperature dependence, as reported in part A. In a certain temperature range, the

intensities of S1 reflections decrease with increasing temperature, while those of S2 reflections increase. Streaks interconnecting main and S1 reflections appear at 1120K. The present observations support this temperature dependence of the satellite reflections. Thus, the decrease in intensity of the S1 reflections can be explained by a re-ordering of the clusters. This re-ordering may correspond to the formation of decagonal superclusters (DSC), which are composed of five interpenetrating pentagonal superclusters (PSC), as reported in part *A*. Consequently, this re-ordering takes place on cost of the superstructure ordering formed by the PSCs.

To summarize, the structural disorder associated with the S1 reflections shows basically inter-cluster correlations only inside quasiperiodic layers. On the contrary, the S2 reflections are related to both intra- and inter-cluster correlations between adjacent and inside quasiperiodic layers.

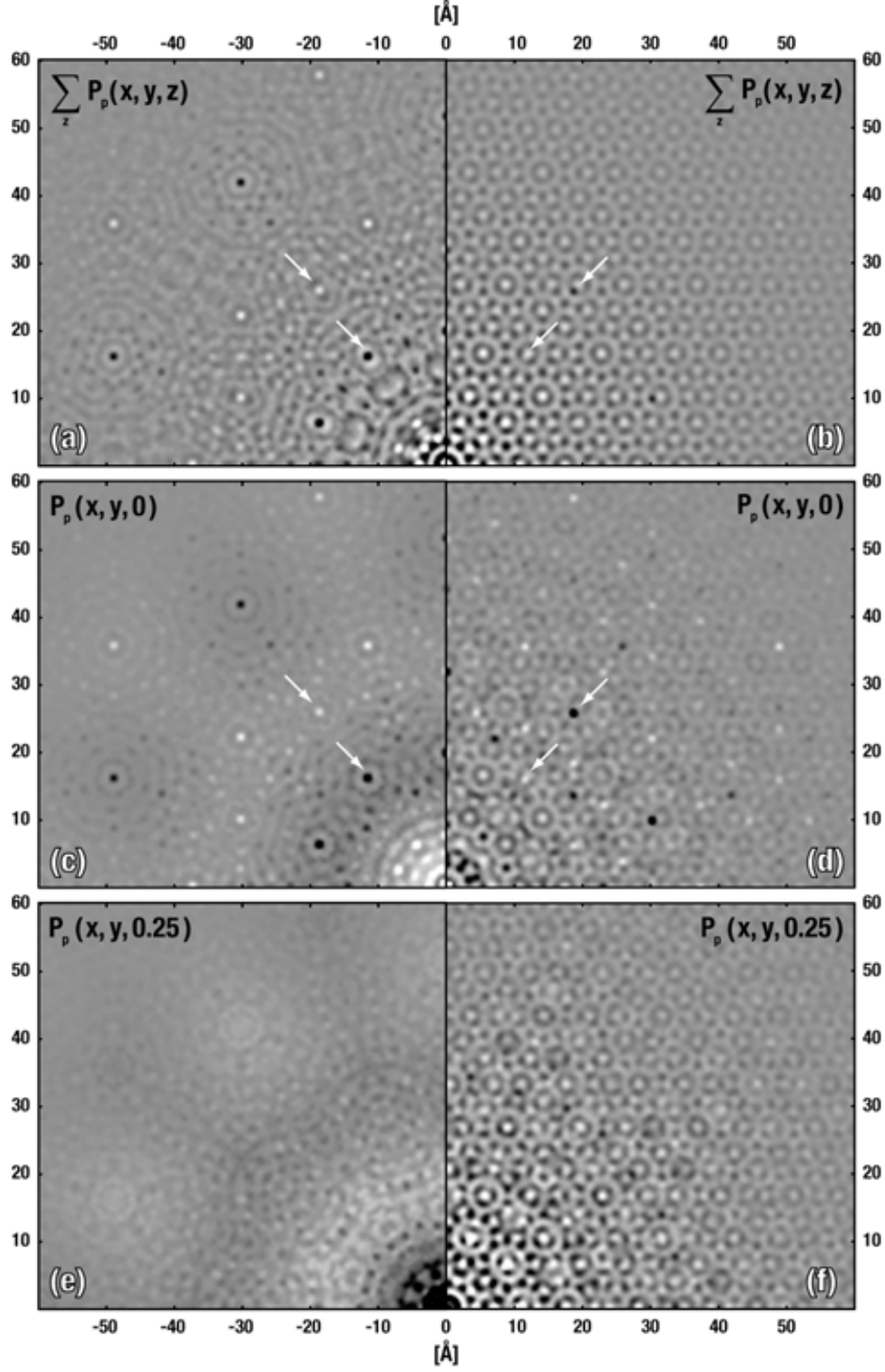


FIG. 12. Projected *PM* (a), the *PMs* at  $z = 0$  (c) and  $z = 0.25$  (e) of *PDS* & *TDS* calculated from S1 reflections [indexing after Edagawa<sup>2</sup>] of the d-Al<sub>71.5</sub>Co<sub>14.6</sub>Ni<sub>13.9</sub> dataset in comparison with *PMs* calculated from S2 reflections (b, d, f), respectively. Strong maxima in one pattern often correspond to minima in the other pattern (see arrows). (b) is strongly structured, indicating the presence of both intra- and inter-cluster correlations, whereby (a) mainly shows inter-cluster correlations. Correlations between adjacent quasiperiodic layers (e, f) differ significantly. (e) shows hardly any correlations in contrast to the (f) which is strongly structured both at small and long Patterson vectors. Relative scaling of the intensities in the patterns (a)-(f) is 5:5:70:20:50:8.



### **E. Sensitivity of diffuse scattering intensities on cluster variations**

Modelling disorder phenomena in quasicrystals can be used as a powerful tool for the selection of correct structure-models. Small changes in cluster models also produce only small changes in the average structure of these clusters. If the atoms, which are affected by these small changes are involved in disorder, such small changes can have a great influence on the diffuse scattering intensities. Thus, a selection of correct structure-models based only on the study of the average structures becomes very difficult and studying the diffuse scattering can be extremely helpful in this case. Figure 13 shows a comparison of diffraction patterns of average structures and diffuse scattering for different cluster-models. Zoomed sections of the cluster form factors of the average structures of fivefold orientationally disordered clusters are shown in Fig. 13(a-d) for the structure models of Abe<sup>20</sup>, Abe<sup>19</sup>, Steinhardt<sup>27</sup> and Steurer<sup>30</sup>, respectively. These patterns are governed by Bragg intensities only. Zoomed sections of the corresponding diffuse diffraction intensities of fivefold orientationally disordered clusters are shown in Fig. 13(e-h), respectively. The atomic configurations of the first three clusters are very similar but that the differences to the cluster of Steurer are more pronounced. Indeed, the diffraction patterns of the average structures reflect this coherency. Just by focusing on the diffraction patterns of the average structures, one cannot distinguish between the clusters of Abe<sup>19,20</sup> and Steinhardt<sup>27</sup>. But taking into account the diffuse scattering, all four models can be distinguished.

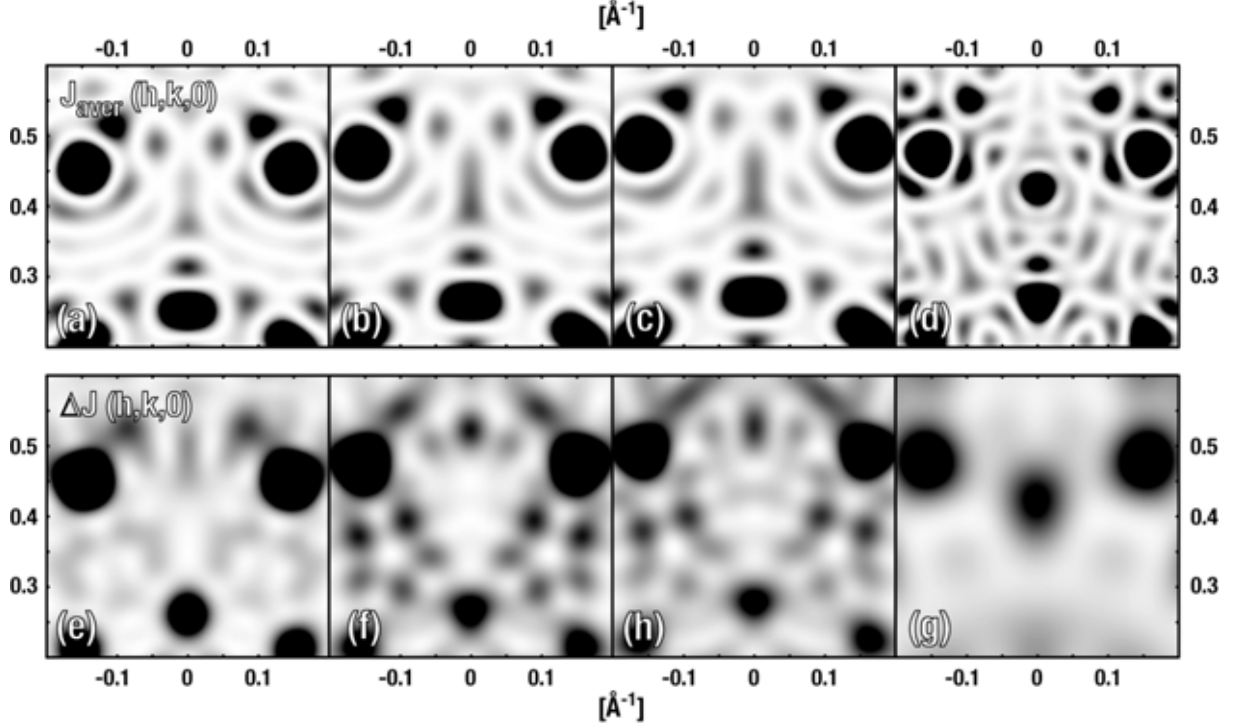


FIG. 13. Comparison of diffraction patterns of the cluster-models of Abe<sup>20</sup>, Abe<sup>19</sup>, Steinhardt<sup>27</sup> and Steurer<sup>30</sup>. The cluster form factors of the average structures of fivefold orientationally disordered clusters are shown in (a-d), respectively. The corresponding diffuse diffraction intensities of fivefold orientationally disordered clusters in (e-h), respectively. The patterns in (a-d) and in (e-h) are on the same scale, respectively.

## VIII. CONCLUSIONS

One of the aims of this study was to explore the structural implications of phasonic disorder on the example of a rhombic Penrose tiling. It results that the local difference structure is quite indifferent to variations in  $K_{ijkl}$  and  $R_{ijkl}$  but depends on the type of disorder (*e.g.* *PDS*, *TDS*). For the same model system it was also shown that phasonic fluctuations of the *ASs* give average clusters in the cut-space that correspond to fivefold orientationally disordered clusters. The hydrodynamic theory of *PDS* & *TDS* was applied successfully to describe the short-range, disordered structure of the *Edagawa-phase*. High-frequency contributions to diffuse scattering, *i.e.* the fine structure of diffuse scattering, give information on long-range correlations, while low-frequency contributions, *i.e.* the overall distribution of diffuse scattering, govern the short-range correlations. The former correlations in the disordered structure of the *Edagawa-phase* have been reproduced inadequately by *PDS*, but the latter

correlations were described excellently. Nevertheless, this does not mean that the underlying, physical disorder phenomena may be of a different kind. It has been shown that phasonic disorder and fivefold orientational disorder of the Abe-cluster can be used equivalently to describe the short-range, disordered structure of the *Edagawa-phase*. Compared thereto, disorder phenomena like domains, strains, dislocations, *etc.* may therefore play a minor role for the description of the local structure of decagonal Al-Co-Ni quasicrystals. The sensitivity of the diffuse intensity distribution to the kind of cluster model employed in the calculations allows to distinguish between different cluster types suggested in literature. Investigations on the structural disorder associated with the quasiperiodic superstructure ordering have shown that the *PMs* calculated only from *PDS* & *TDS* from S1 and S2 reflections behave differently. Former show basically inter-cluster correlations inside quasiperiodic layers, while latter exhibit intra- and inter-cluster correlations, both between adjacent and inside quasiperiodic layers. Our calculations indicated that *PDS* in decagonal quasicrystals can generally be described as fivefold orientational disorder of clusters. This has been shown for decagonal quasicrystals the quasiperiodic patterns of which may be described by a *RPT* and the clusters of which are mirror symmetric.

## ACKNOWLEDGMENT

The authors would like to thank Swiss National Science Foundation for financial support by project No. 20-67872.02. We also thank F. Frey for useful comments and the staff of the beamline D3 at the synchrotron source Hasylab for their assistance with the synchrotron measurements.

- 
- <sup>1</sup> W. Steurer and F. Frey, *Phase Transit.* **67**, 319-361 (1998).
  - <sup>2</sup> F. Frey and E. Weidner, *Z. Kristallogr.* **218**, 160-169 (2003).
  - <sup>3</sup> K. Edagawa, H. Sawa, and S. Takeuchi, *Philos. Mag. Lett.* **69**, 227-234 (1994).
  - <sup>4</sup> M.V. Jaric and D.R. Nelson, *Phys. Rev. B* **37**, 4458-4472 (1988).
  - <sup>5</sup> J. Lei, R. Wang, C. Hu, and D.H. Ding, *Phys. Rev. B* **59**, 822-828 (1999).
  - <sup>6</sup> R. Wang, C. Hu, and J. Lei, *Phys. Rev. B* **61**, 5843-5845 (2000).
  - <sup>7</sup> R. Wang, C. Hu, and J. Lei, *Phys. Status Solidi B* **225**, 21-34 (2001).
  - <sup>8</sup> Y. Ishii, *Mater. Sci. Eng. A* **294-296**, 377-380 (2000).
  - <sup>9</sup> W. Yang, C. Hu, D.H. Ding, and R. Wang, *Phys. Rev. B* **51**, 3906-3909 (1995).
  - <sup>10</sup> C. Hu, R. Wang, W. Yang, and D. Ding, *Acta Crystallogr. Sect. A* **52**, 251-256 (1996).
  - <sup>11</sup> K.J. Strandburg, L.H. Tang, and M.V. Jaric, *Phys. Rev. Lett.* **63**, 314-317 (1989).
  - <sup>12</sup> L.H. Tang, *Phys. Rev. Lett.* **64**, 2390-2393 (1990).
  - <sup>13</sup> L.J. Shaw, V. Elser, and C.L. Henley, *Phys. Rev. B* **43**, 3423-3433 (1991).
  - <sup>14</sup> W.-J. Zhu and C.L. Henley, *Europhys. Lett.* **46**, 748-754 (1999).
  - <sup>15</sup> U. Koschella, F. Gähler, J. Roth, and H.-R. Trebin, *J. Alloys. Comp.* **342**, 287-290 (2002).
  - <sup>16</sup> T.C. Lubensky, S. Ramaswamy, and J. Toner, *Phys. Rev. B* **32**, 7444-7452 (1985).
  - <sup>17</sup> Y. Ishii, *Phys. Rev. B* **45**, 5228-5239 (1992).
  - <sup>18</sup> W. Steurer, *Z. Kristallogr.* **219**, 391-446 (2004).
  - <sup>19</sup> E. Abe, K. Saitoh, H. Takakura, A.P. Tsai, P.J. Steinhardt, and H.C. Jeong, *Phys. Rev. Lett.* **84**, 4609-4612 (2000).
  - <sup>20</sup> E. Abe, S.J. Pennycook, and A.P. Tsai, *Nature* **421**, 347-350 (2003).
  - <sup>21</sup> K. Hiraga, F.J. Lincoln, and S. Wei, *Mater. Trans. JIM* **32**, 308-314 (1991).
  - <sup>22</sup> K. Hiraga, W. Sun, and A. Yamamoto, *Mater. Trans. JIM* **35**, 657-662 (1994).
  - <sup>23</sup> K. Hiraga, T. Ohsuna, W. Sun, and K. Sugiyama, *Mater. Trans.* **42**, 2354-2367 (2001).
  - <sup>24</sup> S. Ritsch, C. Beeli, and H.U. Nissen, *Philos. Mag. Lett.* **74**, 203-209 (1996).
  - <sup>25</sup> S. Ritsch, C. Beeli, and H.U. Nissen, *Philos. Mag. Lett.* **75**, 49-49 (1997).
  - <sup>26</sup> K. Saitoh, K. Tsuda, M. Tanaka, K. Kaneko, and A.P. Tsai, *Jpn. J. Appl. Phys* **36**, L1400-L1402 (1997).
  - <sup>27</sup> P.J. Steinhardt, H.C. Jeong, K. Saitoh, M. Tanaka, E. Abe, and A.P. Tsai, *Nature* **396**, 55-57 (1998).

- 
- <sup>28</sup> P.J. Steinhardt, H.C. Jeong, K. Saitoh, M. Tanaka, E. Abe, and A.P. Tsai, *Nature* **403**, 267-267 (2000).
- <sup>29</sup> P. Gummelt, *Geom. Dedicata* **62**, 1-17 (1996).
- <sup>30</sup> W. Steurer, T. Haibach, B. Zhang, S. Kek, and R. Lück, *Acta Crystallogr. Sect. B* **49**, 661-675 (1993).
- <sup>31</sup> Y.F. Yan, S.J. Pennycook, and A.P. Tsai, *Phys. Rev. Lett.* **81**, 5145-5148 (1998).
- <sup>32</sup> Y.F. Yan and S.J. Pennycook, *Nature* **403**, 266-267 (2000).
- <sup>33</sup> Y.F. Yan and S.J. Pennycook, *Phys. Rev. B* **61**, 14291-14294 (2000).
- <sup>34</sup> Y.F. Yan and S.J. Pennycook, *Phys. Rev. Lett.* **86**, 1542-1545 (2001).
- <sup>35</sup> K. Lemster, Ph.D. thesis ETH No. 14141, ETH Zurich, 2001.
- <sup>36</sup> T. Haibach, A. Cervellino, W. Kek, and W. Steurer, *HASYLAB Jahresber.* **I**, 519-520 (1997).
- <sup>37</sup> A. Cervellino, T. Haibach, and W. Steurer, *Acta Crystallogr. B* **58**, 8-33 (2002).
- <sup>38</sup> W. Steurer and T. Haibach, in *International Tables for Crystallography*, 2nd edition, edited by U. Shmueli (Kluwer Academic Publishers, Dordrecht/Boston/London, 2001), Vol. **B**, Chap. 4, p.486-532.
- <sup>39</sup> E.N. Maslen, A.G. Fox, and M.A. O'Keefe, in *International Tables for Crystallography*, edited by A.J.C. Wilson (Kluwer Academic Publishers, Dordrecht/Boston/London, 1992), Vol. **C**, Chap. 6.1, p.500-502.
- <sup>40</sup> M.A. Chernikov, H.R. Ott, A. Bianchi, A. Migliori, and T.W. Darling, *Phys. Rev. Lett.* **80**, 321-324 (1998).
- <sup>41</sup> J.M. Cowley, *Diffraction Physics*, **3rd rev. ed.** (Elsevier Science B.V., Amsterdam, 1995).
- <sup>42</sup> K. Niizeki, *J. Phys. Soc. Jpn.* **63**, 4035-4043 (1994).
- <sup>43</sup> K. Hiraga, T. Ohsuna, and S. Nishimura, *Philos. Mag. Lett.* **80**, 653-659 (2000).

### 4.3 Appendix

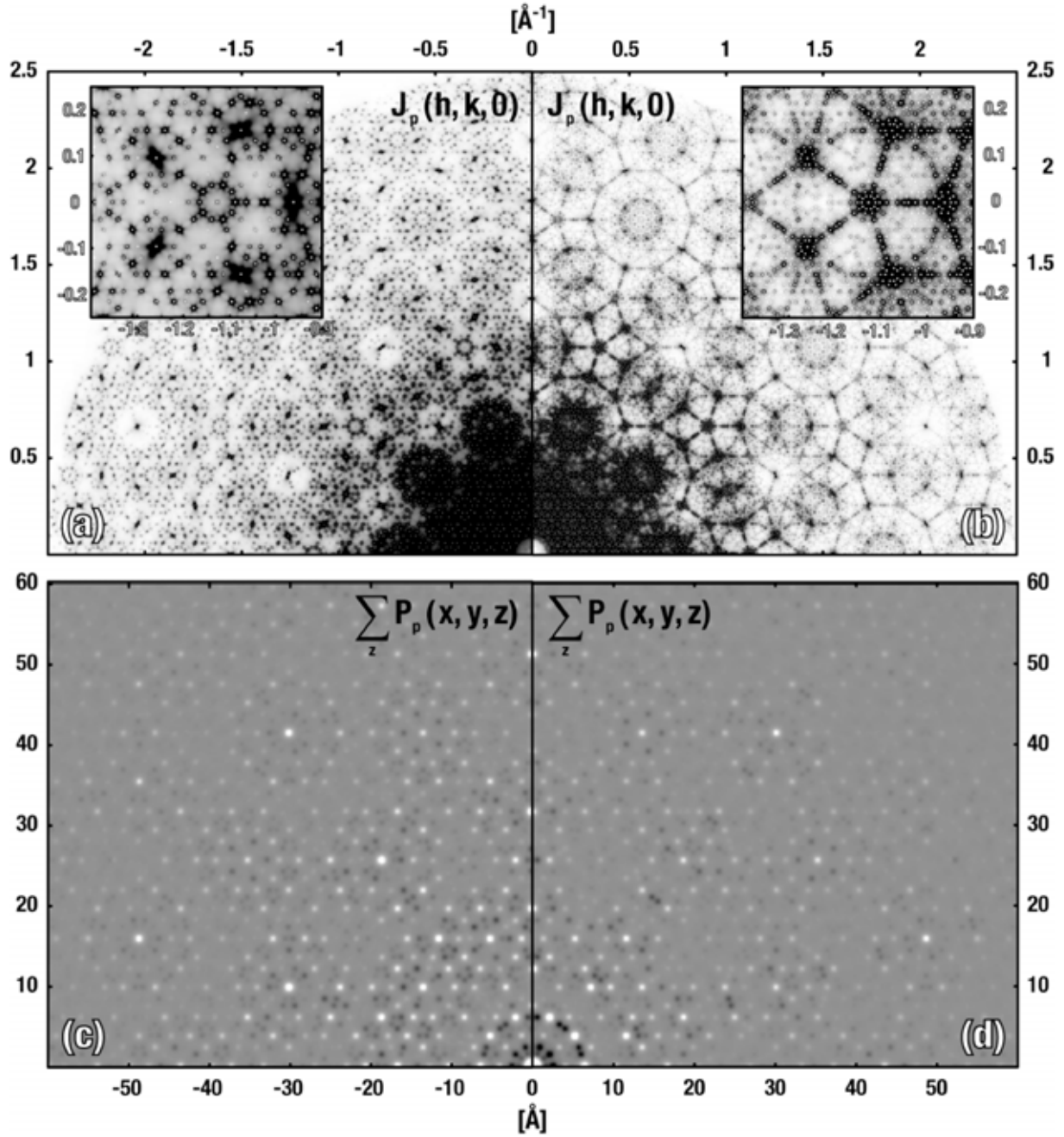


**Fig. 3:** This figure corresponds to Fig. 1 of article III, with the following difference: (a, b) show in addition to the zoomed sections the complete diffraction patterns. The *PMs* depicted in (c, d) cover larger extents (up to 60  $\text{\AA}$ ). Although the overall distribution of diffuse scattering in (a, b) are similar, the fine structure changes significantly. Especially the evolution of diffuse 'streaks' is striking, which arise from the superposition of *PDS* from weak Bragg reflections with high perpendicular-space components. Despite the prominent differences in the diffraction patterns (a, b), the *PMs* look very similar, *i.e.* the short-range, disordered structures of the two *RPTs* show only minor differences.

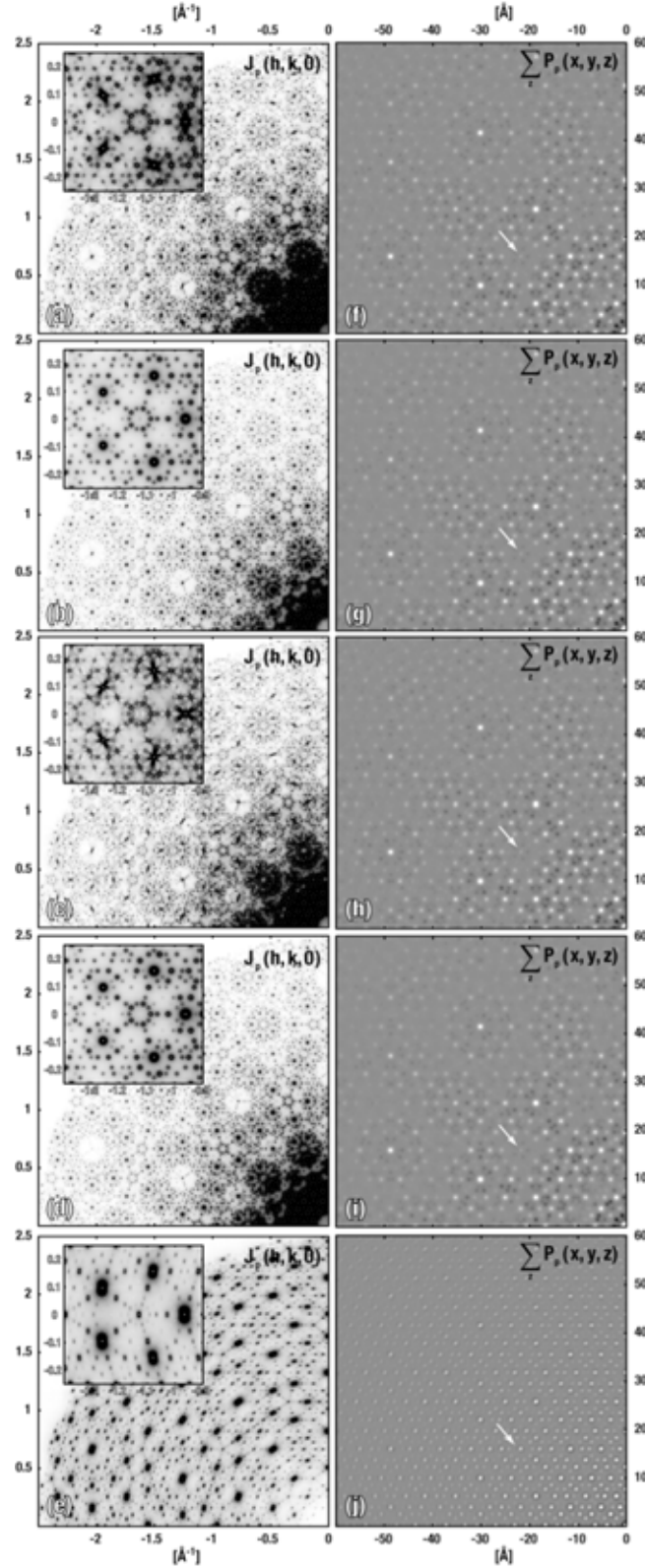


**Fig. 4:** This figure corresponds to Fig. 2 of article III, with the following difference: (a-e) show in addition to the zoomed sections the complete diffraction patterns. The *PMs* depicted in (f-j) cover larger extents (up to 60 Å). The complete diffraction patterns in (a-d) show a similar overall distribution of diffuse scattering unlike their fine structures (see zoomed sections). Hardly any differences can be spotted in the *PMs* of the first four cases (f-i) up to 60 Å.

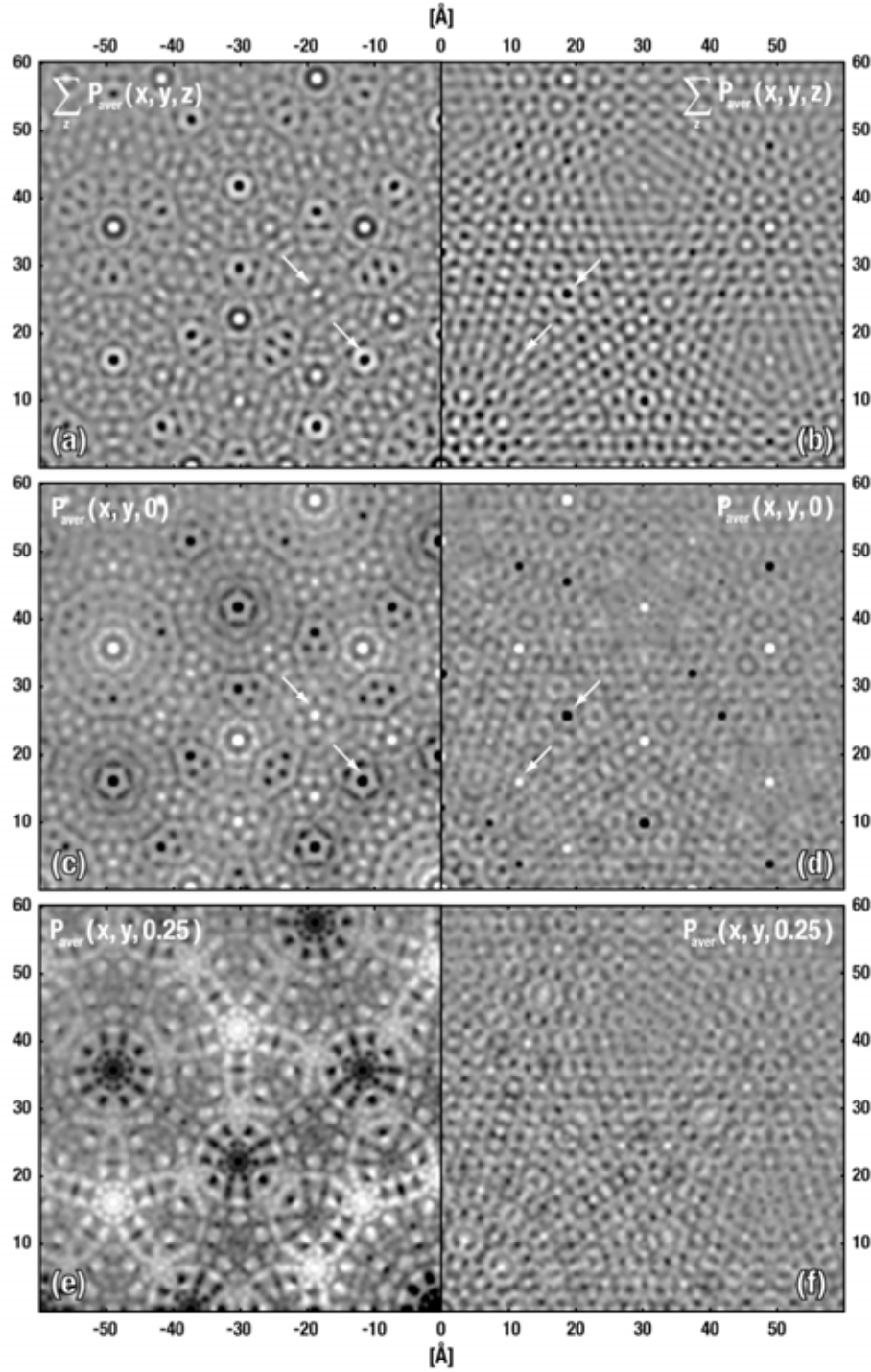


**Fig. 5:** Projected *PM* (a), the *PMs* at  $z=0$  (c) and  $z=0.25$  (e) of the average structure calculated from S1 reflections of the d-Al<sub>71.5</sub>Co<sub>14.6</sub>Ni<sub>13.9</sub> dataset in comparison with *PMs* calculated from S2 reflections (b, d, f), respectively [cf. to Fig. 12 in article III]. Strong maxima in one pattern often correspond to minima in the other pattern (see arrows). (b) is strongly structured, indicating the presence of both intra- and inter-cluster correlations, whereas (a) mainly shows inter-cluster correlations. Note the remarkable difference in the *PMs* for correlations between adjacent quasiperiodic layers (e, f). (e) shows only long-range correlations, whereas (f) which is strongly structured both at small and long Patterson vectors. Relative scaling of the intensities in the patterns (a)-(f) is 2:1:20:4:10:3.



## 5 Modelling structural disorder of the diffuse interlayers

### 5.1 Article IV

This section contains a reprint of the article:

Th. Weber, M. Kobas and W. Steurer: The Disordered 8 Å Superstructure of a Decagonal  $\text{Al}_{70}\text{Co}_{12}\text{Ni}_{18}$  Quasicrystal. *Ferroelectrics*, **305**, 213-218 (2004).

# The Disordered 8 Å Superstructure of a Decagonal $\text{Al}_{70}\text{Co}_{12}\text{Ni}_{18}$ Quasicrystal

Th. WEBER, M. KOBAS, and W. STEURER

*Laboratory of Crystallography, ETH-Zurich, Zurich, Switzerland*

*(Received 5 September 2003; accepted 28 September 2003)*

*Diffuse inter-layers from a decagonal quasicrystal with nominal composition  $\text{Al}_{70}\text{Co}_{12}\text{Ni}_{18}$  were investigated at 1120 K, 1070 K and 300 K. Patterson maps calculated from the inter-layers are interpreted such that the main units for correlated displacements along  $a_5$  are structure motifs ('clusters') having a diameter of about 15 Å. At 1120 K, displacements of the clusters are uncorrelated along quasiperiodic directions, while they form about 42 Å-sized super-clusters at lower temperatures. The arrangement but not the inner structure of the super-clusters differs significantly at 1070 K and 300 K. Further, a first approach to the atomic structure of the 15 Å cluster is presented.*

**Keywords** Decagonal quasicrystal; Patterson method; diffuse scattering

## 1. Introduction

Diffraction patterns from decagonal quasicrystals frequently show a system of diffuse layers lying halfway between Bragg layers along the periodic axis (for an overview see Frey et al. [1]). The Bragg layers reflect the 4 Å periodic average structure, while the inter-layers represent an 8 Å super-structure [2]. The super-structure is (usually) long-range ordered along the periodic direction and short-range ordered perpendicular thereto. The origin of the underlying disorder is assumed to come from displacive disorder of columnar clusters along the periodic direction. Appearance and temperature evolution of diffuse intensities in Bragg-layers and inter-layers differ significantly [3] and may therefore be discussed independently. We will show and discuss results from *in-situ* measurements of an  $\text{Al}_{70}\text{Co}_{12}\text{Ni}_{18}$  quasicrystal at 1120 K, 1070 K and 300 K. For experimental details see Steurer et al. [3] and Kobas et al. [4]. Diffuse scattering in the Bragg-layers is discussed in this issue by Kobas et al. [4].

## 2. Observations

### 2.1. Experimental

The scattering pattern of the diffuse inter-layers exhibits a strong variation as a function of temperature (Fig. 1). The diffuse scattering is relatively simple at 1120 K showing broad diffuse maxima only. After cooling down to 1070 K the diffuse intensities condense into almost Bragg-peak like maxima. The maxima can be indexed by the same quasiperiodic lattice as the reflections in the Bragg layers, including main reflections as well as first and second order satellite reflections. At 300 K the diffraction pattern is similar to 1070 K but it is more blurred. Despite the fact that the fine structure of the diffuse features is changing

Address correspondence to Th. Weber, Laboratory of Crystallography, ETH-Zurich, Zurich, Switzerland.  
 E-mail: thomas.weber@mat.ethz.ch

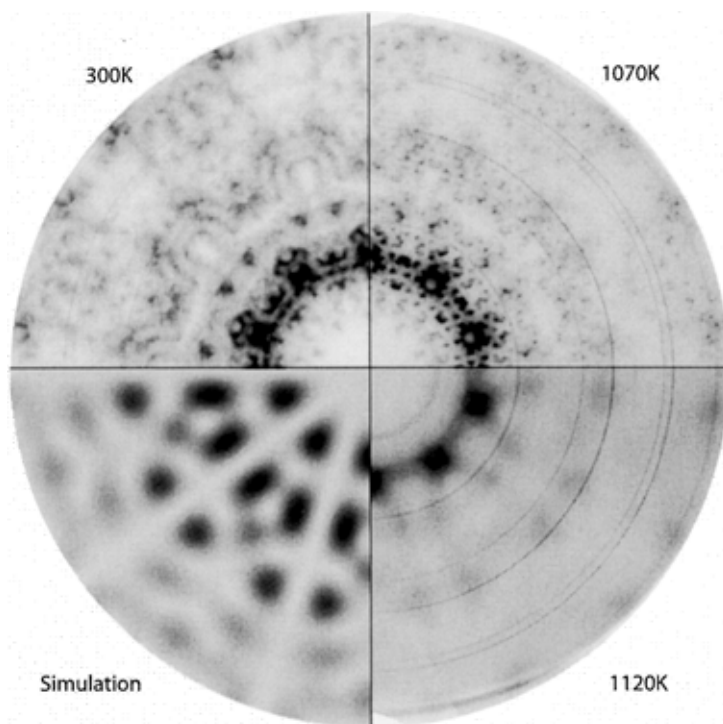


**FIGURE 1** Diffraction patterns from  $h_5 = 1.5$  at various temperatures. Calculated intensities from the atomistic model discussed in section 3 are shown in the lower left corner. The powder rings in the experimental data are coming from the sample holder.

drastically during temperature evolution, the overall distribution of diffuse intensities is mostly unaffected by temperature.

## 2.2. Patterson Maps

Figure 2 shows the temperature dependence of the zero layer Patterson maps (PMs), each calculated from the first three orders of the corresponding diffuse inter-layers. The PMs reflect correlated displacements of atoms along the periodic direction. Positive peaks mean that the corresponding inter-atomic vector of the real structure occurs more often than in 4 Å average structure, negative peaks indicate that the number of inter-atomic vectors is less frequent than in the average structure. The PM at 1120 K shows significant maxima for Patterson vectors  $|\mathbf{p}| \leq 15$  Å only. Some minor peaks in the range  $|\mathbf{p}| > 15$  Å are also present, but it is not clear if they are real Patterson maxima or if they are truncation effects. The PM at 1070 K can be divided into three zones: zone I ( $|\mathbf{p}| \leq 15$  Å) is almost unchanged compared to 1120 K, zone II ( $15 \text{ Å} < |\mathbf{p}| \leq 42 \text{ Å}$ ) is densely filled with positive and negative maxima of moderate amplitude including some strong negative peaks at  $|\mathbf{p}| \approx 23$  Å and zone III ( $|\mathbf{p}| > 42 \text{ Å}$ ) is characterized by a few, but very intense positive maxima at  $|\mathbf{p}| \approx 61$  Å and 99 Å. Additionally, a number of positive and negative peaks can be seen in zone III, which are significantly weaker than those observed in zone II. At 300 K, zones I and II are very similar compared to 1070 K. The situation in zone III, however, changes significantly. The strong maxima observed at 1070 K become weaker, but they are still present. At the same time, new peaks emerge in zone III.

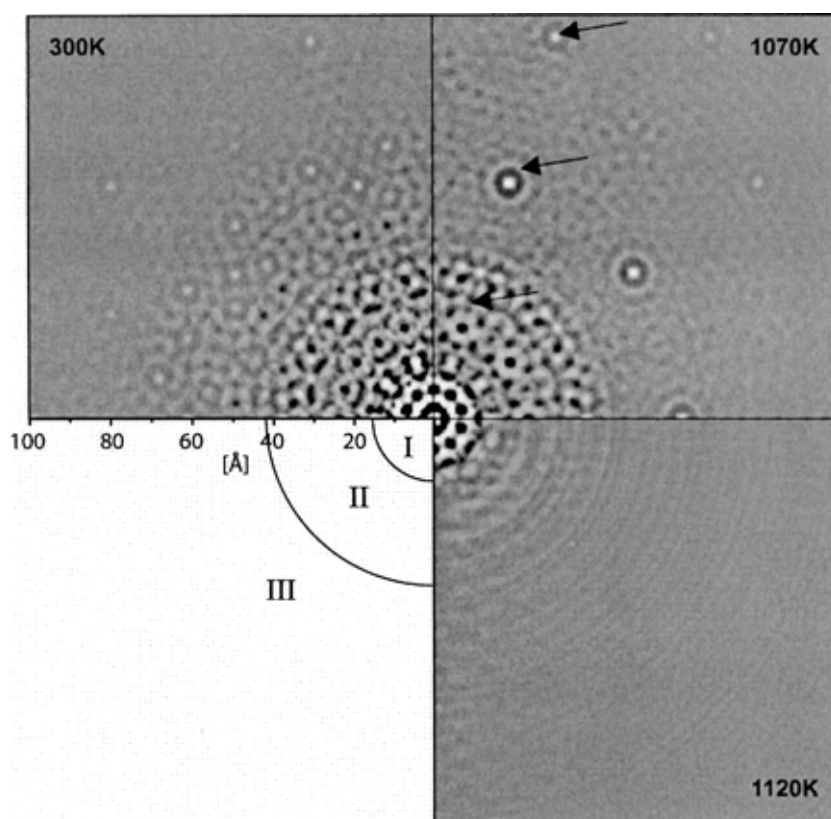


**FIGURE 2** Zero layer Patterson maps calculated from diffuse inter-layers only. Negative peaks are darker, positive peaks are brighter than the zero level background. The arcs indicate boundaries between zones I, II and III and the arrows show the prominent peaks at  $|\mathbf{p}| \approx 23$  Å, 61 Å and 99 Å. The Patterson maps are smoothed to minimize truncation effects.

### 3. Discussion

The observations from the PMs may be interpreted as follows: Throughout the temperature range examined in this work a basic cluster-like arrangement with a diameter of about 15 Å is the main motif for correlated displacements along the periodic direction. From the temperature dependent behaviour in zone I it is obvious that the fine structure of this cluster does hardly change as a function of temperature. At 1120 K no spatial correlations between z-positions of neighbouring clusters are present. Going down to lower temperatures, the emerging peaks from zone II may be understood to come from a rearrangement of the 15 Å clusters forming super-clusters with a diameter of about 42 Å. The rather sharp transition from zone II to zone III indicates that the super-clusters are of a well-defined shape. A possible explanation for this behaviour would be that frustration effects prohibit a growth of the super-clusters to a size larger than 42 Å. The strong maxima in zone III may be interpreted as translation vectors between the super-clusters. At 1070 K the most dominant distance between two super-clusters is about 61 Å. On the transition to 300 K, the *internal* structure of the super-clusters is almost unchanged, but their *spatial distribution* is reordered on the cost of the 1070 K arrangement. Obviously, this transition is not complete, since the strong maxima observed at 1070 K are still present.

A first approximation to the atomic fine structure of the 15 Å cluster, and therefore to the diffraction pattern at 1120 K could be found on the basis of the following model. The disordered motif is assumed to consist of a pentagon with a radius of about 5.4 Å. The pentagon is present in two orientations, which are separated by a rotation of  $18^\circ$  around an axis passing through the centre of the pentagons. Locally, only one of the two orientations may be realized. Figure 1 shows the diffuse diffraction pattern that is expected if a 8 Å periodic sequence is present, consisting of 4 Å separated  $+9^\circ$  and  $-9^\circ$  rotated pentagons. No correlations are assumed to be present along quasiperiodic directions. A reasonable agreement between observed and calculated data can be observed. Although incomplete, this model may serve as a first step towards a more sophisticated model of the real atomic arrangement in the disordered structure. Note that orientational disorder as described by this model is equivalent to 4 Å displacive disorder along  $a_5$ .

### Acknowledgment

The authors would like to thank Swiss National Science Foundation for financial support (project No. 20-67872.02).

### References

1. F. Frey, E. Weidner, M. de Boissieu, R. Currat, K. Shibata, A. P. Tsai, and T. J. Sato, *Phil. Mag. A* **80**, 2375–2391 (2000).
2. F. Frey and W. Steurer, *J. Non-Cryst. Solids* **153/154**, 600–605 (1993).
3. W. Steurer, A. Cervellino, K. Lemster, S. Ortelli, and M. A. Estermann, *Chimia*, **55**, 528–533 (2001).
4. M. Kobas, Th. Weber, W. Steurer, this issue.

## 6 Outlook

### 6.1 Optimisation of the *punch-and-fill* method

The *punch-and-fill* method introduced in article I can be used to extract diffuse scattering data from full 3D diffraction datasets. The total scattering intensity is *punched* at the positions of the Bragg reflections with a window-function of constant size [see article I]. *Punching* sets the scattering intensities at and around the positions of Bragg reflections to 0. Because of the constant size of the window-function, tails of strong reflections are not completely removed, while diffuse scattering around weak reflections is partially removed. Former leads to spiky relicts in the scattering intensity around positions of strong Bragg reflections. It is unclear whether these intensities can be attributed to Bragg scattering or to diffuse scattering. This fact mainly depends on the considered disorder phenomenon. Létoublon *et al.* (2001) have measured diffuse scattering from icosahedral Al-Pd-Mn quasicrystals on an absolute scale and have shown that phasonic diffuse scattering (*PDS*) peaks under certain Bragg reflections with intensities that reach up to ten percent of the corresponding Bragg intensity. Because of the uncertainty of the attribution of the spiky relicts in our case, one should try to remove them. Despite the constant size of the window-function, it was shown that the *punch-and-fill* method extracts diffuse scattering reasonably well.

The *punch-and-fill* method may be optimized by removing the spiky relicts in the diffraction patterns. Filter functions that are widely used in multi-dimensional digital image processing can be applied to perform this task. One possibility is to identify the spiky artifacts that correspond to high-frequency contributions in the diffraction patterns with appropriate filters (e.g. Laplace filter) and subsequently remove them from the diffraction patterns. Another possibility is to smooth the artifacts with appropriate filters (e.g. median filter). However, the consequences of the application of such filters onto the Patterson function must be carefully analysed.

Another step in optimizing the *punch-and-fill* method can be achieved by dynamically adjusting the size of the window-function to the width of the Bragg reflections. This modification minimizes the artifacts, which are caused by incomplete *punching* of the strong Bragg reflections and the removal of diffuse scattering around weak reflections. An implementation of these modifications in the developed code is straightforward, but the

consequences onto the mathematical formalism of the *punch-and-fill* method [see article I] are complex. A careful analysis of the influence of these changes onto the Patterson function would be necessary.

Most possibly the best approach to separate diffuse and Bragg scattering intensities may be achieved by fitting the Bragg peaks with two-dimensional profile functions. A highly resolved diffraction pattern is a necessary prerequisite in this case. For a subsequent Patterson analysis of the data with a fine resolution in Patterson space, one also needs a large extent in reciprocal space. This would result in very large datasets, which are both difficult to measure and difficult to handle (memory demand). The advantage of such an approach is obvious: one would obtain a dataset of diffuse scattering, which correctly describes its distribution even at the positions of Bragg reflections.

## 6.2 Growth model for decagonal Al-Co-Ni

Our model calculations in article III have shown that the disordered structure at small Patterson vectors of the *Edagawa-phase* [Edagawa, 1994] can be described equally well both by *PDS* and fivefold orientational cluster disorder. The *PDS* approach is based on an abstract concept describing disorder in *5D* space and does not give an atomic model of a corresponding *3D* disordered structure. In contrast to that, the calculations of structural disorder (cluster orientational disorder) give a picture of the disordered *3D* structure but they are limited in size to the diameter of a columnar cluster ( $\approx 20$  Å). In a next step, a *3D* structure model must be developed including fivefold orientational disorder of the clusters. Basically, two approaches are conceivable. In the first approach, a perfect quasiperiodic covering is constructed and subsequently the clusters are disordered by fivefold orientational disorder. Aggravating circumstances are that the clusters do overlap and thus, the assignment of a cluster becomes intricate. In the second approach, it would be possible to use a growth model. Starting from a single cluster, the quasiperiodic structure is constructed by adding clusters according to some overlap rules. This approach facilitates significantly the application of a fivefold orientational disorder to the clusters. A major advantage of this approach is that one can study the development of a quasiperiodic superstructure step by step with increasing size of the structure model. The model calculations on structural disorder associated with the quasiperiodic superstructure ordering [see article III] should allow the identification of a forming superstructure. In the following subsections we have applied overlap rules to the Abe-cluster [Abe, 2003] and identified the rules that lead to a perfect covering, a relaxed one and a relaxed covering with fivefold orientationally disordered

clusters. These investigations build up the basis for the simulation of a growth model for decagonal Al-Co-Ni that describes the 3D disordered structure of the *Edagawa-phase*.

Quasiperiodic order, both perfect and random, can either be described in the framework of tilings or cluster-coverings. A major advantage of the cluster-covering model is that it is based on one single structural building unit (cluster). Gummelt has worked out overlap rules for the cluster-covering model that enforce either perfect or random decagon coverings [Gummelt 1996, 2000, 2004]. However, atomic decoration of the decagon coverings has a major influence on the applicability of the overlap rules. We have applied both, perfect and relaxed overlap rules on decagons decorated with the Abe-cluster and explored the consequences of introducing fivefold orientational disorder of clusters on the applicability of the overlap rules.

Figure 6 shows the application of the perfect overlap rules (a-d) and the relaxed overlap rules (e-h) onto the layer  $A$  ( $z = 0$ ) of the Abe-cluster. The index  $z$  refers to the  $\approx 8$  Å superstructure. Note that type-A overlaps [named after Gummelt, 2000] appear for the overlap rules (a-c, e-g) and type-B overlaps for the overlap rules (d, h). First, we will exclude disorder and just focus on perfect decagon coverings. We can see, that the Abe-cluster is compatible with rule a), c) and d) but not with rule b). The atomic configuration inside the overlap region of b) is chemically unreasonable because of too short atomic distances. Rule b) could be fulfilled if layer  $A$  ( $z = 0$ ) of the cluster is overlapped with layer  $B$  ( $z = 0.25$ ) but this would imply that the average cluster shows a sequence of layers  $\dots(A+B)(A+B)\dots$  and thus, the periodicity would be reduced to  $\approx 2$  Å. Such a structure would not show any Bragg reflections at  $h_5 = 2$ , which is not the case for any decagonal Al-Co-Ni quasicrystal found so far. Thus, rule b) is forbidden and one can exclude cluster shifts of  $\approx 2$  Å along the periodic axis as a possible disorder phenomenon for decagonal Al-Co-Ni quasicrystals. Consequently, the Abe-cluster could only form a perfect quasiperiodic pattern with overlap rules a), c) and d). But since rule d) always enforces rule b) in the case of perfect matching [Gummelt, 1996], one ends up only with overlap rules a) and c) for a perfect quasiperiodic pattern constructed with the Abe-cluster. In this case, one obtains a tie-and-navette tiling [private communications with Gummelt]. Only overlaps of type-A appear in such a structure.

Taking into account the relaxed overlap rules, one can exclude f), g) and h) for the same reason as for rule b). Gummelt has shown that rules e) and g) always lead to a contradiction concerning the generation of larger patches [Gummelt, 2000, 2004], *i.e.* structural frustrations are the consequence. For random decagon coverings of the Abe-cluster, one ends up with



rules a), c), d) and e). Note that rule d) is now allowed, because perfect matching is not imperative any more in the case of the relaxed overlap rules. Both overlaps of type-A and type-B do appear in the case of a random decagon covering of the Abe-cluster.

Now, how does orientational disorder of clusters influence the applicability of the overlap rules? Comparing the atomic configurations in a) and b) [Fig. 6(a, b)], one can see that the configuration in b) is obtained by rotating the upper right cluster in a) around  $108^\circ$  (clockwise rotation). From a) to e), one must rotate  $144^\circ$ , from a) to f)  $252^\circ$ , from b) to e)  $36^\circ$ , from b) to f)  $144^\circ$ ; from c) to g)  $36^\circ$  (rotation of the lower right cluster) and from d) to h)  $108^\circ$ . Investigations on the atomic configurations obtained by rotations of  $36^\circ$  and multiples therefrom have shown the following: rotations of  $\{36^\circ + n \cdot 72^\circ | n = 0, 1, 2, 3, 4\}$  end up with chemically unreasonable configurations, whereby rotations of  $\{n \cdot 72^\circ | n = 0, 1, 2, 3, 4\}$  give reasonable atomic configurations. The latter rotations have been simulated in the calculations of fivefold orientational disorder of the Abe-cluster (see article III). The observation that rotations of  $\{36^\circ + n \cdot 72^\circ | n = 0, 1, 2, 3, 4\}$  give chemically unreasonable atomic configurations can be explained by the pseudo  $10_5$ -screw axis of the Abe-cluster. The atomic configurations obtained by a shift of the cluster by  $\approx 2 \text{ \AA}$  along the periodic direction is very similar to the one obtained by rotating the cluster around  $36^\circ$ . Thus, rotations of  $\{36^\circ + n \cdot 72^\circ | n = 0, 1, 2, 3, 4\}$  end up in forbidden configurations as in the case for rule b) and one can exclude tenfold orientational disorder of the Abe-cluster as a possible disorder phenomenon for the *Edagawa-phase*. All above observations do equally well apply to layer A and layer B of the Abe-cluster.

To summarize, when starting from the Abe-cluster, chemically reasonable atomic configurations for perfect coverings are obtained with rules a) and c) (only type-A overlaps occur). One ends up with a tie-and-navette tiling for the perfect quasiperiodic structure. Random coverings can evolve from overlap rules a), c), d) and e) and both type-A and type-B overlaps occur. In the case of a random covering including fivefold orientationally disordered clusters one ends up with overlap rules a), c), d), e) and cluster rotations of  $\{n \cdot 72^\circ | n = 0, 1, 2, 3, 4\}$  (both type-A and type-B overlaps occur). Note that structural frustrations are the consequence of overlaps of kind e) [Gummelt, 2000, 2004]. In the article III we have shown that phasonic fluctuations of the atomic surfaces (ASs) in decagonal quasicrystals modify structures that are best described by a tie-and-navette tiling to structures that are best described by fivefold orientationally disordered clusters.

What do the Patterson maps (*PMs*) look like for a random covering including fivefold orientationally disordered clusters constructed with the above described overlap rules? The approach used for the calculations of structural disorder (cluster orientational disorder) does not include inter-cluster correlations (see article III). Thus, the *PMs* calculated therefrom do not show Patterson vectors longer than the diameter of a single cluster. A structure showing the same *PMs* is obtained by omitting all overlap rules in the cluster-covering model. However, the difference *PMs* of the *Edagawa-phase* do show correlation lengths longer than the diameter of a single cluster [see article I]. These *PMs* may be explained by a disordered structure motif (*DSM*) that is arranged at certain translation vectors [see article I]. Such a structure can be constructed with the above described overlap rules for the random covering model including fivefold orientationally disordered clusters. The discrete set of overlap rules used to construct such a structure increases the correlation lengths for both, the average and the disordered structure, because of information transfer from cluster to cluster. Such a model would show *PMs* with a *DSM* arranged at certain translation vectors. The *DSM* corresponds in this case to the *PM* of the fivefold orientationally disordered cluster.

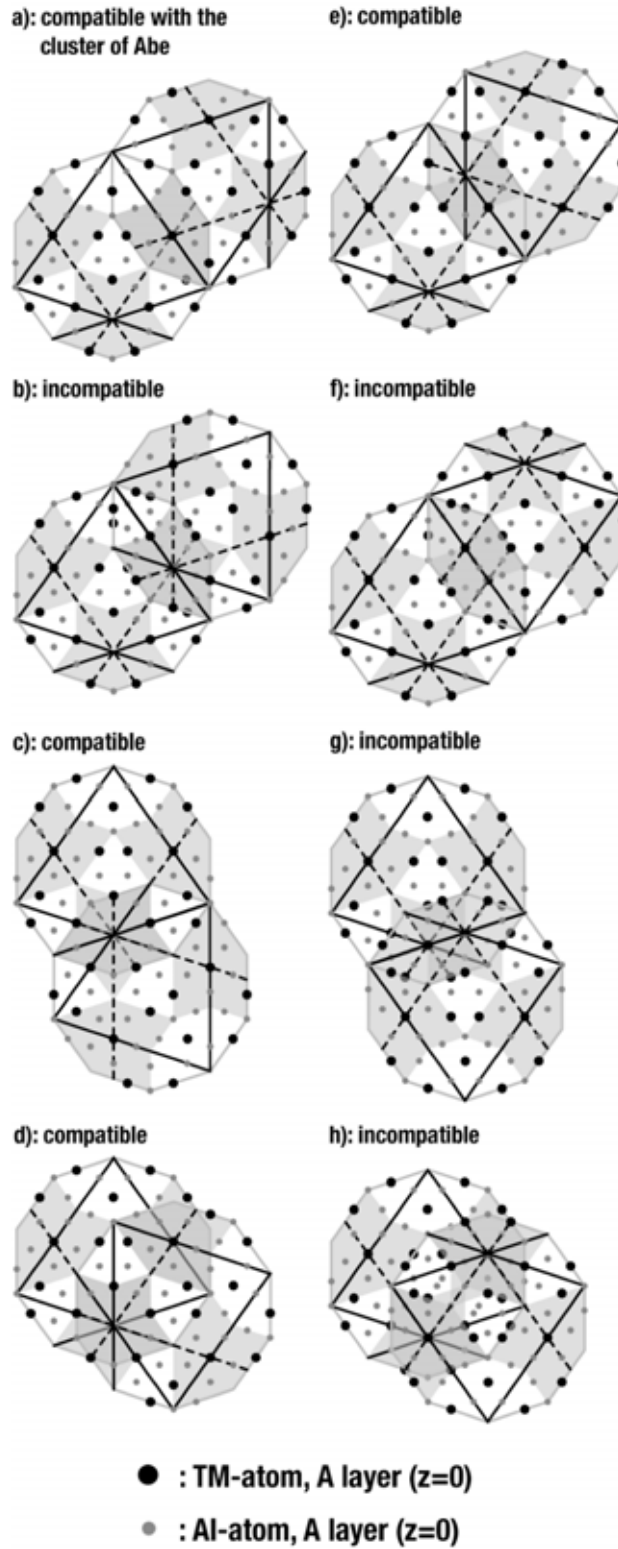


**Fig. 6:** Perfect (a-d) and relaxed (e-f) overlap rules of cluster-coverings applied on decagons decorated with the Abe-cluster [Abe, 2003]. Chemically reasonable atomic configurations for perfect coverings are obtained with rules a) and c) (only type-A overlaps occur). One ends up in a tie-and-navette tiling for the perfect quasiperiodic structure. Random coverings are possible with overlap rules a), c), d) and e) and cluster rotations of  $\{n \cdot 72^\circ | n = 0, 1, 2, 3, 4\}$  (both type-A and type-B overlaps occur). For details see text.

## Bibliography

- Abe, E., Pennycook, S.J. and Tsai, A.P., *Nature* **421**, 347-350 (2003).
- Cowley, J.M., *Diffraction Physics*, 3rd edition (Elsevier Science B.V., Amsterdam, 1995).
- Edagawa, K., Sawa, H. and Takeuchi, S., *Philos. Mag. Lett.* **69**, 227-234, (1994).
- Gummelt, P., *Geom. Dedicata* **62**, 1-17 (1996).
- Gummelt, P., Ph. D. thesis, Ernst-Moritz-Arndt-Universität (1998).
- Gummelt, P. and Bandt, C., *Mater. Sci. Eng. A* **294**, 250-253 (2000).
- Gummelt, P., *J. Non-Cryst. Solids* **334&335**, 62-67 (2004).
- Janot, C., *Quasicrystals. A Primer*, 2nd edition (Oxford University Press, UK, 1994).
- Keen, D.A. and McGreevy, R.L., *Nature* **344**, 423-425 (1990).
- Létoublon, A., De Boissieu, M., Boudard, M., Mancini, L., Gastaldi, J., Hennion, B., Caudron, R. and Bellissent, R., *Philos. Mag. Lett.* **81**, 279-283 (2001).
- Nield, V.M. and Keen D.A., *Diffuse Neutron Scattering from Crystalline Materials* (Oxford University Press, UK, 2001).
- Ossi, P.M., *Disordered Materials. An Introduction* (Springer, Berlin, 2002).
- Penrose, R., *Bull. Inst. Maths. and its Appl.* **10**, 266-271 (1974).
- Proffen, Th. and Welberry, T.R., *Acta Crystallogr. A* **53**, 202-216 (1997a).
- Proffen, Th. and Welberry, T.R., *Z. Kristallogr.* **212**, 764-767 (1997b).
- Proffen, Th. and Welberry, T.R., *Phase Transit.* **67**, 373-397 (1998).
- Shechtman, D., Blech, I.A., Gratias, D. and Cahn, J., *Phys. Rev. Lett.* **52**, 1951-1953 (1984).
- Stadnik, Z.M., *Physical Properties of Quasicrystals* (Springer, Berlin, 1998).
- Suck, J.-B., Schreiber, M. and Häussler, P., *Quasicrystals. An Introduction to Structure, Physical Properties, and Applications* (Springer, Berlin, 2002).
- Trebin, H.R., *Quasicrystals. Structure and Physical Properties* (Wiley-VCH, Weinheim, 2003).
- Welberry, T.R., *J. Appl. Crystallogr.* **19**, 382-389 (1986).
- Welberry, T.R., *Diffuse X-Ray Scattering and Models of Disorder* (Oxford University Press, UK, 2004).

## Curriculum vitae

Family name: Kobas  
 First name: Miroslav  
 Date of birth: 23 September 1975  
 Place of birth: Slavonski Brod, Croatia  
 Citizen: Swiss, Croatian  
 Address: Neunbrunnenstr. 120  
 CH-8050 Zürich  
 Marital status: Single

1982-1990	Elementary school, Bazenheid, St. Gallen
1990-1995	High school, Wattwil, St. Gallen
1995-1996	Mathematics studies, University of Zurich
1996-2001	Materials science studies, ETH Zurich
1999-2000	Materials science studies, EPFL Lausanne
2001-2004	Ph. D. studies, Laboratory of Crystallography, ETHZ
2001-2004	Scientific assistant, Laboratory of Crystallography, ETHZ

1999	Semester thesis " <i>Ab-Initio Modellierung von eindimensionalen leitenden Polymeren</i> " at the Institute of Polymers under supervision of Prof. Dr. U Suter, ETH Zurich
2000	Semester thesis " <i>Hochtemperatur-Druckversuche an Titan-Aluminiden</i> " at the Institute of Applied Physics under supervision of Prof. Dr. G. Kostorz, ETH Zurich
2001	Diploma thesis " <i>Modellierung diffuser Streuphänomene</i> " at the Laboratory of Crystallography under supervision of Prof. Dr. W. Steurer, ETH Zurich
2001-2004	Ph. D. thesis " <i>Modelling Structural Disorder in Quasicrystals. Decagonal Al-Co-Ni</i> " at the Laboratory of Crystallography under supervision of Prof. Dr. W. Steurer, ETH Zurich

## Acknowledgements

I wish to express my sincere gratitude to

- [illegible]